

HARVARD UNIVERSITY
Graduate School of Arts and Sciences




DISSERTATION ACCEPTANCE CERTIFICATE


The undersigned, appointed by the

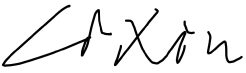
Harvard John A. Paulson School of Engineering and Applied Sciences
have examined a dissertation entitled:

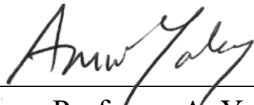
“Electrical Properties of Novel and Engineered Two-Dimensional Materials”

presented by: Mehdi Rezaee

Signature 
Typed name: Professor P. Kim

Signature 
Typed name: Professor E. Hu

Signature 
Typed name: Professor X. Li

Signature 
Typed name: Professor A. Yacoby

December 16, 2022

Electrical Properties of Novel and Engineered Two-Dimensional Materials

A DISSERTATION PRESENTED
BY
MEHDI REZAAE
TO
THE DEPARTMENT OF APPLIED PHYSICS

IN PARTIAL FULFILLMENT OF THE REQUIREMENTS
FOR THE DEGREE OF
DOCTOR OF PHILOSOPHY
IN THE SUBJECT OF
APPLIED PHYSICS

HARVARD UNIVERSITY
CAMBRIDGE, MASSACHUSETTS
DECEMBER 2022

©2022 – MEHDI REZAAE
ALL RIGHTS RESERVED.

Electrical Properties of Novel and Engineered Two-Dimensional Materials

ABSTRACT

Layered materials are a class of matter in which atomic layers are bonded to one another via van der Waals (vdW) forces. Due to these weak, out-of-plane interactions, we can exfoliate layered materials even down to monolayer thicknesses. Confinement of electron interactions to two dimensions (2D) has led to the rise of new exciting physical properties which are largely inaccessible in three dimensions. Additionally, we can create new artificial interfaces which do not occur naturally, by creating heterostructures of the exfoliated materials. Therefore, assembling vdW materials with highly-tunable properties have been at the epicenter of innovative material and physics research over the past two decades. This dissertation reports on the methods for electrical and optical characterization of some of these novel two dimensional materials. Increasing the amount of electronic and ionic charge that can be rapidly accumulated in and recovered from a material is the preeminent chemical challenge for electrochemical energy storage devices like supercapacitors and batteries. In the first two parts of this thesis, I will reveal the role of the interface during intercalation processes by creating heterostructures with finite, discrete hetero-layers. Here, we demonstrate the electro-intercalation of lithium at the level of singular “vdW number of constituent layers,” comprised of deterministically stacked hexagonal boron nitride (hBN), graphene, and molybdenum dichalcogenide layers. Such engineered functional vdW heterostructures enable the direct resolution of intermediate stages in the intercalation of discrete heterointerfaces and the extent of charge transfer to individual layers. Also, we develop *operando* optical microscopy to investigate the dynamics of ion diffusion into thin graphite to estimate upper diffusion limits. Furthermore, developing new quantum materials has a crucial role in advancing quantum technology. Advances in crystal growth methods provide scientists opportunities to invent new layered materials with phenomenal electrical and optical properties. In the second part of this thesis, I will present electrical characterization of novel layered materials, such as metal organic frameworks (MOFs), a new allotrope of carbon—so called graphullene, and CeSiI as new 2D heavy fermions candidates. I will present novel device fabrication techniques and electron transport characterizations based on these low-dimensional quantum materials. The results in this thesis provide new methodologies and offer novel approaches to manipulating the charge density in the 2D limit and to explore the electrical properties of quantum materials.

Contents

TITLE PAGE	i
COPYRIGHT	ii
ABSTRACT	iii
TABLE OF CONTENTS	iv
FRONT MATTER	vi
Author List	vi
List of Figures	viii
Dedication	x
Acknowledgements	xi
1 INTRODUCTION	1
1.1 Two Dimensional Materials	2
1.2 Electro-intercalation in Mesoscopic Scale	4
1.3 Novel Organic & Semi-organic Layered Materials	7
1.4 Strongly Correlated System : Kondo effect in low dimensions	8
1.5 Overview of This Thesis	13
2 ELECTROCHEMICAL INTERCALATION INTO VAN DER WAALS HETEROSTRUCTURES	17
2.1 Introduction	17
2.2 Electrochemical doping & intercalation	18
2.3 Low-temperature charge transport and magnetoresistance analysis	20
2.4 Raman & Photoluminescence spectroscopy studies	30
2.5 Transmission electron microscopy of intercalation process	32
2.6 Density Functional Theory (DFT) computations	35
2.7 conclusion	38

3	DIFFUSION STUDY OF CATIONS $[\text{AlCl}_4^-]$ INTO FEW LAYER GRAPHENE	40
3.1	Introduction	40
3.2	Electro-intercalation in 2D limits of the $\text{AlCl}_4^-/\text{graphite}$ system	43
3.3	Dynamic of ion diffusion in continuum limit (Random Walk)	46
3.4	Chloroaluminate AlCl_4^- ion diffusion via optical microscopy	48
3.5	AlCl_4^- Diffusion Study into Disk Shape Electrode	51
3.6	Conclusion	53
4	ELECTRON TRANSPORT IN ORGANIC AND SEMI ORGANIC LAYERED MATERIALS	55
4.1	Introduction	55
4.2	Air & Solvent Free Device fabrication	56
4.3	Electrical Transport Single crystals of 2D MOFs $\text{Ni}_3(\text{HITP})_2$	58
4.4	Hall Effect Measurement in Single Crystals of 2D MOFs $\text{Ni}_3(\text{HHTP})_2$	63
4.5	Graphullerene : superatomic cousin of graphene	68
5	HEAVY FERMIONS IN THE 2D LIMITS	73
5.1	Introduction	73
5.2	CeSiI new candidate for 2D Heavy Fermions	75
5.3	Air & Solvent Free Device fabrication for few layer CeSiI	79
5.4	Electrical Transport : Kondo lattice on few layer CeSiI	81
5.5	Magneto-resistance and Fermi surface reconstruction for few CeSiI	82
5.6	Magneto-resistances for 4 layers CeSiI	88
5.7	Conclusion	89
6	OUTLOOK	91
	APPENDIX A FABRICATION AND CHARACTERIZATION OF ELECTROCHEMICAL CELL	94
	APPENDIX B DIFFUSION STUDY MICRO-ELECTROCHEMICAL CELL FABRICATION	97
	APPENDIX C CESII DEVICE FABRICATION COMPLEXITY	99
	REFERENCES	108

Author list

The content in Chapter 2 is included in the publication and authors who contributed:

- **Bediako, D. Kwabena***, **Mehdi Rezaee***, Hyobin Yoo, Daniel T. Larson, S. Y. Zhao, Takashi Taniguchi, Kenji Watanabe, Tina L. Brower-Thomas, Efthimios Kaxiras, and Philip Kim. "Heterointerface effects in the electrointercalation of van der Waals heterostructures." *Nature* 558, no. 7710 (2018): 425-429.

The content in Chapter 3 is included in the publication and authors who contributed:

- **Yoon, Hana***, **Mehdi Rezaee***, Yeong A. Lee, Kanghoon Yim, Rizcky Tamarany, Chan-Woo Lee, Valerie S. McGraw et al. "Chloroaluminate Anion Intercalation in Graphene and Graphite: From Two-Dimensional Devices to Aluminum-Ion Batteries." *Nano Letters* 22, no. 4 (2022): 1726-1733.

The content in Chapter 4 is included in the publication and authors who contributed:

- Day, Robert W., D. Kwabena Bediako, **Mehdi Rezaee**, Lucas R. Parent, Grigori Skorupskii, Maxx Q. Arguilla, Christopher H. Hendon et al. "Single crystals of electrically conductive two-dimensional metal-organic frameworks: Structural and electrical transport properties." *ACS central science* 5, no. 12 (2019): 1959-1964.
- Ha, Dong-Gwang, **Mehdi Rezaee**, Yimo Han, Saima A. Siddiqui, Robert W. Day, Lilia S. Xie, Brian J. Modtland et al. "Large single crystals of two-dimensional π -conjugated metal-organic frameworks via biphasic solution-solid growth." *ACS central science* 7, no. 1 (2020): 104-109.
- Elena Meirzadeh, Austin M. Evans, **Mehdi Rezaee**, Milena Milich, Connor J. Dionne, Thomas P. Darlington, Si Tong Bao, Amy Marie K. Bartholomew, Taketo Handa, Daniel J. Rizzo, Ren A. Wiscons, Mahniz Reza, Amirali Zangiabadi, Natalie Fardian-Melamed, Andrew C. Crowther, P. James Schuck, D. N. Basov, Xiaoyang Zhu, Ashutosh Giri, Patrick E. Hopkins, Philip Kim, Michael L. Steigerwald, Jingjing Yang, Colin Nuckolls, Xavier Roy. "A few-layer covalent network of fullerenes" in *Nature* 613, no. 7942 (2023): 71-76.

The content in Chapter 5 is included in the publication and authors who contributed:

- Victoria A. Posey, Simon Turkel, **Mehdi Rezaee**, Aravind Devarakonda, Asish Kundu, Chin Shen Ong, Michael E. Ziebel, Daniel G. Chica, Rocco Vitalone, Ran Jing, Suheng Xu, David Needell, Elena Meirzadeh, Margalit Feuer, Apoorv Jindal, Tonica Valla, T. Yilmaz, E. Vescovo, Xiaoyang Zhu, Allen Scheie, Andrew May, D. N. Basov, Angel Rubio, Cory Dean, Philip Kim, Andrew Millis, Abhay Pasupathy, Xavier Roy. "A two-dimensional heavy fermion metal " in progress to submit in Nature.

List of Figures

1.1	2D materials	2
1.2	van der Waals 2D materials	3
1.3	Li Intercalation into graphite.	4
1.4	Intercalation into van der Waals hetero structure.	5
1.5	Porous, conductive 2D MOFs.	6
1.6	Carbon allotropes.	7
1.7	Kondo effect : Interaction between free electrons and magnetic impurities.	9
1.8	Heavy fermion components and Kondo lattice formation	10
1.9	Fermionic Resonance band in presence of Kondo effect.	11
1.10	Doniach phase diagram.	12
1.11	Quantum criticality in Kondo Lattice system.	13
2.1	Van der Waals heterostructures for lithium intercalation.	20
2.2	Intercalation of Structure II graphene–metal dichalcogenide heterostructures.	21
2.3	Additional electrochemical and Hall data of structure II graphene–MoSe ₂ stack.	22
2.4	Quantum transport at low temperature	24
2.5	Quantum Transport data on multi-structure-device.	26
2.6	Additional data on multi-structure-device	27
2.7	Charge transport parameters	28
2.8	Tuning intercalation properties with vdW heterolayers.	30
2.9	Raman & photoluminescence spectroscopy Map.	33
2.10	Extend Data for Raman & photoluminescence spectroscopy.	34
2.11	Structural evolution of vdW heterostructures with electrochemical intercalation.	36
2.12	Density Functional Theory (DFT) computations.	37
3.1	Fabrication of micro-electrochemical cell for AlCl ₄ ⁻ process	43
3.2	On-chip electrochemical cell and intercalation of few-layer graphene.	45
3.3	Electrical Transport of intercalated of few-layer graphene.	45
3.4	2D random walk path for an ion moving inside graphite.	47
3.5	Schematic showing on-chip spectroelectrochemical cell.	49
3.6	on-chip spectroelectrochemical cell data analysis.	50

3.7	On-chip Disk shape electrochemical cell for Diffusion Study	52
3.8	Diffusion study of Disk shape electrochemical cell vs T.	53
3.9	Calculation of diffusion coefficient for variable temperature	54
4.1	high-resolution stencil mask technique.	57
4.2	EM images of morphology observed following growth of $\text{Ni}_3(\text{HITP})_2$ using previously reported conditions.	59
4.3	Conductive 2D MOF devices of $\text{Ni}_3(\text{HITP})_2$	60
4.4	$\text{Ni}_3(\text{HITP})_2$ rod devices and variable temperature (VT) conductivity measurements.	61
4.5	$\text{Ni}_3(\text{HHTP})_2$ growth process.	64
4.6	SEM and optical image Single-crystal plates of $\text{Ni}_3(\text{HHTP})_2$	64
4.7	stencil mask technique to fabricate $\text{Ni}_3(\text{HHTP})_2$	65
4.8	$\text{Ni}_3(\text{HHTP})_2$ comparison of several different device.	66
4.9	Electrical properties of Ni-CAT-1 ($\text{Ni}_3(\text{HHTP})_2$).	67
4.10	Synthesis and crystal structures of polyfullerides.	68
4.11	Mg deintercalation and mechanical exfoliation to produce graphullerene.	70
4.12	Exfoliation and characterization of polyfullerides crystals.	71
5.1	Crystal structure, crystal image, exfoliation, atomic force microscopy of CeSiI.	76
5.2	Heat capacity, magnetic properties, and electrical transport of CeSiI.	77
5.3	Device Fabrication for few layer CeSiI.	80
5.4	Atomic Force Microscopy of Fabricated few layer CeSiI device.	81
5.5	Electrical Transport : Kondo lattice on few layer <i>CeSiI</i>	82
5.6	Electrical Transport :fermi liquid Kondo lattice on few layer <i>CeSiI</i>	83
5.7	Electrical Transport : Longitudinal magneto-resistance for few layer CeSiI.	84
5.8	Electrical Transport : Hall Data for few layer <i>CeSiI</i>	86
5.9	Electrical Transport : Hall Data line cut.	87
5.10	Electrical Transport : Differential Hall coefficient	87
5.11	Electrical Transport : Shubnikov–de Haas oscillation (sdH) in R_{xx}	88
5.12	Electrical Transport for 4-layers CeSiI.	89
A.1	Device fabrication Steps for electrochemcial cell.	95
C.1	<i>CeSiI</i> degradation	100
C.2	<i>CeSiI</i> fabricated device degradation without hBN	101
C.3	<i>CeSiI</i> fabricated device degradation with hBN	102

THIS THESIS IS DEDICATED TO MY FAMILY WHO SUPPORT ME THROUGH THIS JOURNEY.

Acknowledgments

A PhD journey is not just a research adventure. It is truly a lifetime experience which shapes our mind to the surrounding world. First and foremost, I would like to express my deepest gratitude to my thesis advisor, Professor **Philip Kim**, for his unwavering support and guidance throughout this journey. His expert knowledge and invaluable feedback helped me to navigate the complex research landscape and develop my ideas. I never felt alone along this long path. I had the privilege to learn research techniques from him and be his mentee. Undoubtedly, he gave me great encouragement to explore newly-discovered materials. His support gave me the confidence to be more mindful not only about my research path, but also about my personal life path. For all of this, I am eternally grateful.

I am also incredibly grateful to the members of my thesis committee, Professor **Evelyn Hu**, Professor **Amir Yacoby**, and Professor **Xin Li**, for their valuable insights and constructive critiques. Their expertise and dedication helped me to refine my research and improve the overall quality of my thesis. I would also like to thank the SEAS and Physics faculty and CNS staff at Harvard for creating an intellectually stimulating and supportive environment.

Accomplishments cannot be achieved relying on ourselves alone. Friends and colleagues are cornerstones along the path. I am truly blessed to have met and maintained a great group of friends and colleagues who helped me during this journey. I am particularly grateful to **Kwabena** for his help with various aspects of my research. He was my first mentor at Harvard. He taught me all the essential steps in both physics and chemistry that I needed to succeed in a great part of my PhD research. Also, I would like to thank **Frank, Andy, Andres, Isabelle, Zhongying, Zeyu, James, Tom, Andrew, Rebecca, Laurel, Kierstin, Grace, Alex, Artem, Jonathan, Thao, Nadine, Sejoon, Abhishek, Qi, Sasha, Joon Young, Dapeng** and all former group members of the Kim lab for your support and guidance throughout my PhD journey. Their suggestions and constructive criticisms have helped me improve the quality of my research. Your unwavering encouragement, invaluable advice, and willingness to lend a helping hand have meant the world to me. Also, I would like to say thank you to all the volleyball players on the **Volleytronics** team.

During my PhD, I had the chance to collaborate on several projects with different groups. I have met the most amazing people from several universities. I would like to express my sincere gratitude to all of my collaborators who have contributed to the success of our projects. Their invaluable input and support have been instrumental in the completion of this work. I would like to thank **Bobby and Dong-Gwang** from MIT. Their expertise and experience were essential in helping me navigate my research on MOFs. Also, I would like to thank **Elena** and **Victoria** from Columbia. Elena is a kind

and smart researcher who leads the graphullerene project.

Friends are the greatest source of strength and inspiration. I am particularly grateful to **Amirhassan, Ehsan, and Mary** for their help with various aspects of my research and personal life. I met **Amirhassan** eight years ago and we became friend from the first moment. He is a very smart, hard-working, and passionate researcher. We went through the same path during the PhD. His presence along the way was a great source of confidence and comfort for me. I am truly blessed to have you as my friend. **Ehsan** is one of my best friends. His calmness and kindness always gave me confidence that we can overcome any hard situations. We took many trips and hikes which became the best memories I have of my PhD life. My very first day at Harvard, when I walked into room 207 in McKay, I met **Mary**, who was sitting in the desk next to mine. She is one of the kindest people that I have ever met in my life. She is a super smart and hardworking scientist. I am really honored to be her friend, and thank her for all of her support. In the last couple years of my PhD, I met a few new friends whose presence gave me enormous hope and encouragement for my life. I am particularly thankful to **Evie, Sajede, Payam, Sepideh, Daneil, Cigdem, Mohammad, Shakiba, Amin, Sahba, Navid, Ali, Ameneh, Dustin, Ashley** and **Ellie** for their support and inspiration. I am truly blessed to have you as my friends. Thank you from the bottom of my heart for being amazing friends.

I would like to take a moment to express my deepest appreciation and gratitude to my family. My mother **Noosh Afarin**, and my father **Nasser**, gave me their love, guidance, and support throughout my whole life. They have been my rock and support system throughout my life, providing me with love and encouragement. My parents have been my role models and have taught me valuable lessons about hard work, determination, and the importance of family. They have always been there for me, through the good times and the bad, and I am so grateful for their love and support. My siblings, **Saeede** and **Mohsen**, have also been a source of strength and inspiration for me. They have taught me the importance of the value of having a strong support system. They have always been there to celebrate my achievements. Also, I would like to thank my brother and sister in law **Omid** and **Fariba** for their love and support in all these years. My niece, **Shahzad**, gave me the happiest moments in hardest times with her smiles over the last four years. In short, my family has been my guiding light, and I am so grateful for their love and support. I am truly blessed to have such an amazing family, and I will always cherish the memories we have shared together. I would like to express my love and appreciation to them, and I hope that they know how much they mean to me.

1

Introdcution

Exfoliation of monolayer graphene¹ opened a new era of exploration into the physical properties of materials in the thinnest limits. Since 2004, scientists have been trying to discover new combinations of layered materials that can host new quasi particles for advanced applications. Here, in this thesis, I will discuss electrical characterization of engineered and novel 2–dimensional (2D) materials. In this chapter, as an introduction, I start with general description of 2D materials research, intercalation processes on a mesoscopic scale, electrical transport in novel oraganic/semi-organic materials, and heavy

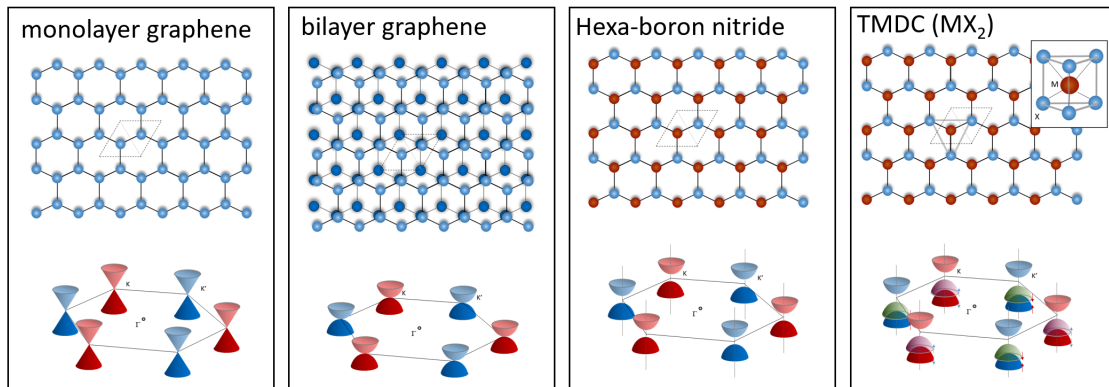


Figure 1.1: 2D materials: semimetal to insulator.

fermion formation in low dimensions, the topics that will be discussed in the following chapters.

1.1 TWO DIMENSIONAL MATERIALS

The mere existence of materials in 2D was under questions for almost 70 years. A theory in the 1930s^{2,3} predicted that, because of thermodynamic limitations, materials could not form or maintain structure in 2D. The energy fluctuations were predicted to cause the sheets of material to fold and become a giant squashy ball, effectively. Unprecedentedly in 2004, Andre Geim and Konstantin Novoselov¹ showed that one can exfoliate graphite down to monolayer thickness, known as graphene, by using scotch tape to break the weak van der Waals (vdW) forces bonding the sheets of graphene together to form graphite. The local thermodynamic fluctuations actually stabilize the 2D materials. Then a single sheet of graphene could be deposited onto a substrate. Graphene, as an allotrope of carbon, is a monolayer of graphite in which atoms are sitting in a honeycomb lattice structure. Based on a tight-binding model, graphene has Dirac cone electronic band structure with massless electrons close to charge neutrality. Graphene, the pioneer of 2D materials, has extraordinary properties such as high mobility, massless Dirac fermions, high thermal conductivity, weak electron-phonon coupling,

etc. Despite its extraordinary properties, graphene has some drawbacks which make it ill-suited for some applications. For instance, the lack of bandgap in graphene limits its application in semiconductor industries. On the other hand, other 2D materials such as transition metal dichalcogenides (TMDs) and hexagonal boron nitride (hBN) show semiconductor to insulator behavior (Fig 1.1). The extensive library of 2D materials makes them a unique platform to explore exotic and phenomenal physical properties such as quantum Hall, fractional quantum Hall, superconductivity, and strongly correlated systems. This discovery has motivated scientists for the past two decades to explore, discover, and grow new 2D materials in order to study condensed matter problems in two dimensions and develop new tools for various applications across fields ranging from bio-technology devices to astronomical sensors and detectors.

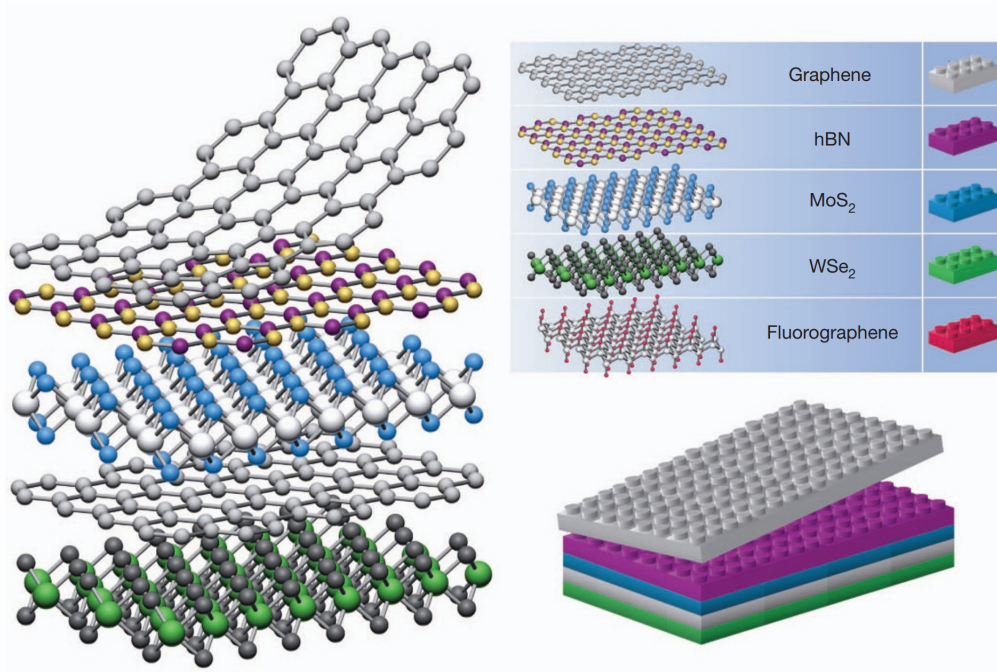


Figure 1.2: Assembling of van der Waals heterostructure by stacking 2D materials⁴.

The diversity in physical properties and exfoliability of 2D materials give us an enormous oppor-

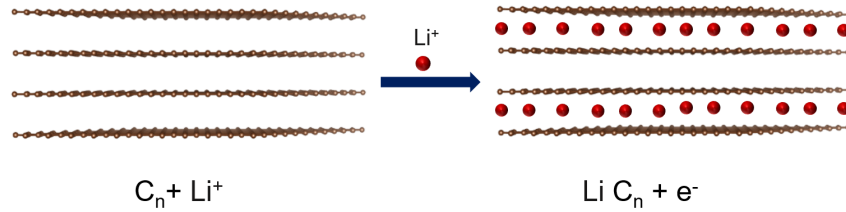


Figure 1.3: the schematic half cell reaction in lithium ion batteries.

tunities to create new heterostructures without worrying about the lattice mismatch at interfaces (Fig 1.2). Creating vdW heterostructures of distinct 2D layers enables us to control and manipulate the generation, confinement and transport of different type of particles /quasi particles such as charge, excitons, photons and phonons within these atomic interfaces. In this thesis, I will discuss the physics and engineering of heterointerfaces by stacking 2D materials and create unique vdW heterostructure. In addition, I try to extend the 2D materials library by studying electrical properties of novel organic /semi organic layered materials.

1.2 ELECTRO-INTERCALATION IN MESOSCOPIC SCALE

Electrochemical intercalation is the insertion of ions between layers of some anode or cathode by use of an electric field as the driving force of the ion-forming chemical reaction⁵. This process give us the possibilities to manipulate layered materials to tune and induce new physical properties by inserting various ions. For instance, Emery *et al*⁶ demonstrate the superconductivity in graphite upon intercalation with calcium(Ca). Furthermore, Dresselhaus *et al*⁵ show the transition metal dichloride could induce strong magnetism in graphite. Also, the intercalation process has great importance in developing rechargeable energy storage system. The reaction at anode/cathode of battery cell is an example of the electro-intercalation process (Fig 1.3). Assembling vdW layers into heterostructures introduces the possibility of preparing heterostructures with uniquely tailored vdW interfaces that, in princi-

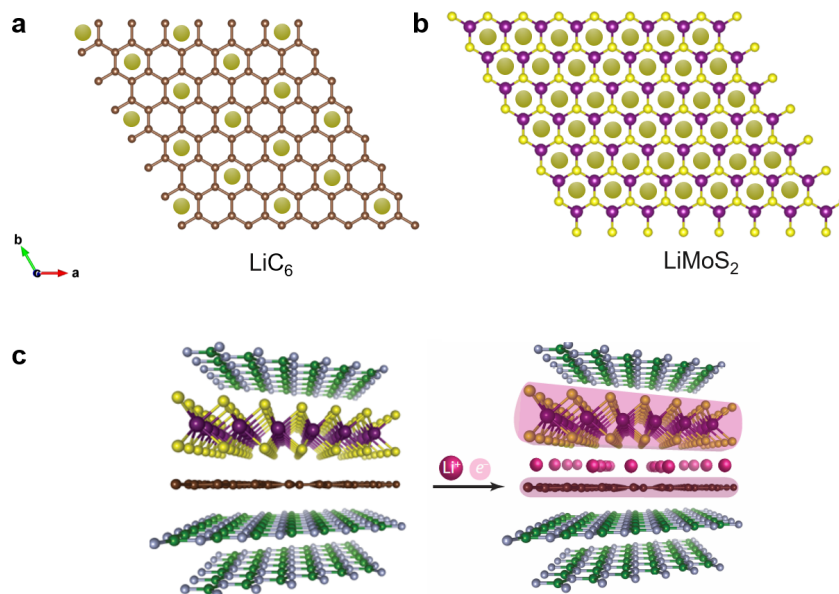


Figure 1.4: a,b, Graphene and MoS₂ are fully intercalated with ions at possible atomic site. c the left side is vdW (hBN/Gr/MoS₂/hBN) host before Li⁺ intercalation process. After, Li ions insert between the host layers, they will donate charge to each individual layers.

ple, may be capable of accommodating more intercalants (increasing capacity), altering intercalation potentials (modifying thermodynamic landscapes) and/or influencing ion conduction through the interlayer gap (regulating ion diffusion kinetics).

Intercalation reactions are ultimately limited by the maximal stoichiometry (number of intercalation sites per unit area) of the intercalation compound (Fig 1.4 a,b). A traditional method to study the intercalation process is based on building an electrochemical cell with the following ingredients: a metal to serve as anode/cathode (for example, platinum or lithium in the case of lithium intercalation), a layered material host (for example graphite or complex oxide such as cobalt oxide, etc.), and an electrolyte. This method has its merits, particularly when performing bulk characterization. However, this bulk measurement cannot provide insightful information about the microscopic process occurring within the individual material layers. Furthermore, while enhancing the ion accumula-

tion is a dominant goal in energy storage research communities, fast charging/discharging, aging, and operation under harsh conditions limit the use of new materials as cathode/anode in storage energy units. To address these problems, we need to understand the dynamics of ion diffusion inside the anode/cathode of the electrochemical cell. Layered materials at the 2D limit are a great platform to study dynamic ion diffusion. Optical microscopy method⁷ can be strongly useful to study ion diffusion into vdW materials as well. The need to investigate the microscopic reactions of intercalation motivated us to develop our new method in which we monitor the intercalation process at the mesoscopic scale for finite discrete individual layers. Thus, we can create an on-chip microscopic electrochemical cell by combining 2D materials with traditional intercalation tools. Particularly, we will present interfaces based on graphene, hexagonal boron nitride, and molybdenum dichalcogenides (Fig 1.4 c) as a prototype vdW heterostructures.

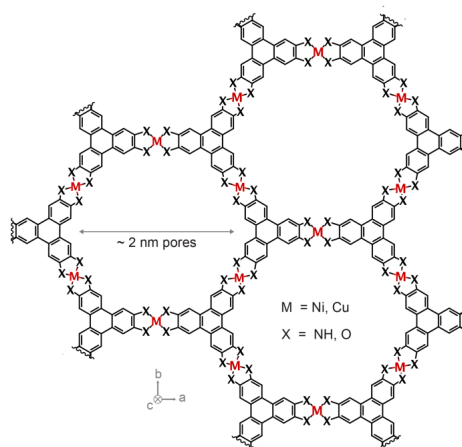


Figure 1.5: Schematic illustrating the general structure of conductive 2D MOFs where layers stack in the c direction to form intrinsically porous crystals with pores of approximately 2 nm in diameter. Metal atoms and organic ligands comprise the honeycomb lattice of the 2D layers. $\text{Ni}_3(\text{HITP})_2$ and $\text{Cu}_3(\text{HHTP})_2$ have $M/X = \text{Ni}/\text{NH}$ and Cu/O respectively.

1.3 NOVEL ORGANIC & SEMI-ORGANIC LAYERED MATERIALS

Recent developments in 2D materials applications have lured chemists and material scientists into growing and constructing more sophisticated and complex layered crystalline systems. In this thesis, two different classes of organic molecular structures are studied. The first one is metal organic frameworks (MOFs). These molecular crystals are organic-inorganic hybrid materials that form a highly ordered network of organic ligands which connect to each other with transition metal ions (fig 1.5)⁸. MOFs have been studied and used for gas storage, catalysis, magnetism, and drug delivery^{9,10,11,12}. This category of material has been developed and studied over the last decade. However, lack of sufficient electrical conductivity has restricted the application of these materials from electronic applications. Only recently have a few groups shown the possibility of synthesizing conductive MOFs^{8,13,14}. Preliminary results on Cu and Ni based MOFs have shown promising conductivity in bulk¹³, but have only been performed as 2-terminal transport measurements on bulk aggregates.

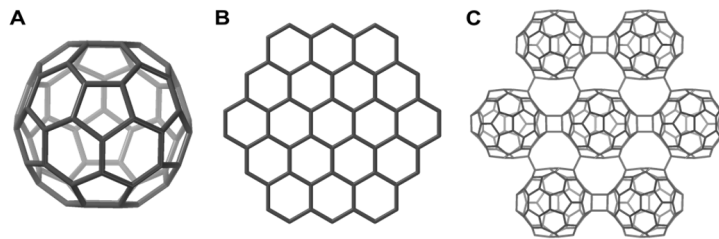


Figure 1.6: a, C_{60} fullerene, a zero-dimensional molecular cage composed of 60 carbon atoms, and b, graphene, consisting of a single layer of atoms, both composed of three-coordinate carbon. c, Graphullerene, a molecular sheet of carbon assembled from covalently-linked C_{60} fullerene superatomic building blocks.

I have also studied materials that are covalently linked molecular sheets. These materials offer the potential to revolutionize technologies related to electronics and energy storage to chemical separations and structural materials¹⁵. Largely, this is because 2D confinement leads to an extraordinary

range of properties distinct from 3-dimensional (3D) analogues. For instance, 2D carbon-allotropes (Fig 1.6) are known to combine desirable electronic properties with flexibility, which has already begun driving their commercial development. However, to continue the technological expansion of 2D materials, new structures must be prepared as high-quality, exfoliatable crystals, and a comprehensive understanding of their material properties must be forged. In addition, the systematic design of 2D materials will benefit enormously from the systematic incorporation of molecular motifs directly into covalent 2D networks. In this regard, I studied a new, two-dimensional crystalline polymer of C_{60} that is a hybrid of molecular and extended carbon materials. This 2D polymer is charge neutral and purely carbon-based with macroscopic crystals large enough to mechanically exfoliate into molecularly-thin flakes with clean interfaces - a critical requirement for the creation of useful heterostructures and optoelectronic devices.

1.4 STRONGLY CORRELATED SYSTEM : KONDO EFFECT IN LOW DIMENSIONS

From the perspective of condensed matter physics, confinement of electrons in low dimensions enhances interactions (for example, Coulomb interactions) and leads to new phenomenal properties. In low dimensions, magnetic atoms with d and f orbitals can affect electronics band structure of materials significantly. Around 100 years ago, after the discovery of superconductivity in mercury, scientists tried to cool down all sorts of metals in search of new superconductors. Surprisingly, they realized some simple metals such as Au, Cu, and Ag exhibit very peculiar low temperature behavior. The resistivity of these metals did not decrease monotonically, with a minimum at non-zero temperatures¹⁶. This finding was baffling for around 30 years before scientists eventually figured out the connection of magnetic impurities to the appearance of minimum resistivity in those metals. In the 1960s, researchers discovered that reducing the number of impurities in such materials also reduced the minimum resistivity reached at low temperatures, to the point of vanishing resistivity once all magnetic

impurities were completely removed¹⁷. Thus we learned that the presence of magnetic impurities in a sea of electrons can affect the behavior of electrons at low temperatures.

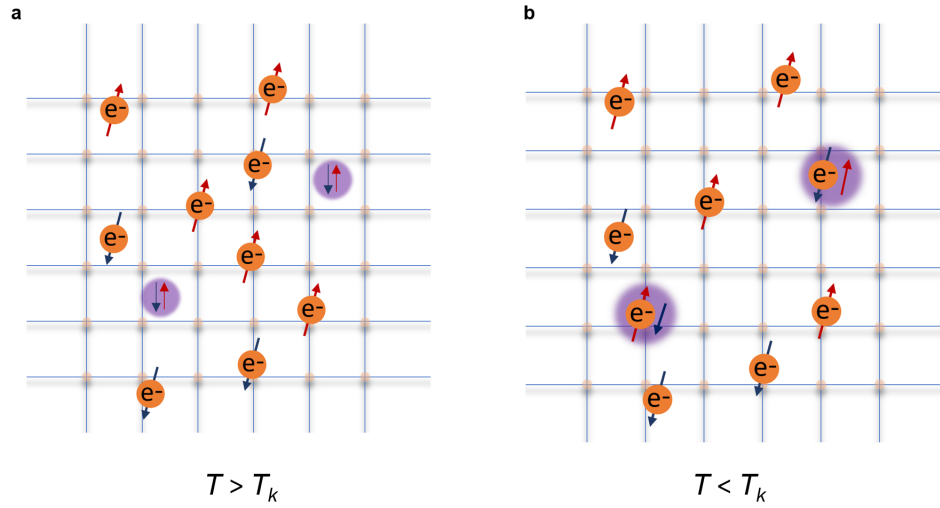


Figure 1.7: **a.** Schematic illustration of rectangular lattice with free electrons in orange coloring. Above T_k , the interaction between localized ions and the sea of electrons is weak. **b.** When temperature is below T_k , we have continuous formation of the singlet Kondo state. The localized ion starts to screen the spin of conduction electrons at the Fermi surface.

In 1962, Kondo proposed a mechanism describing how the presence of magnetic ions alters the minimum resistivity in metals¹⁸. This process, the so called Kondo effect, proposes a scenario in which magnetic ion impurities with a high-temperature magnetic Curie susceptibility are screened by the spin of conduction electrons to form spinless scattering sites. The Kondo effect is a continuous process which occurs at the Kondo temperature (T_K) or a magnetic field that is lower than the interaction energy scale. Local moments at the scattering sites suppress the conduction electron mobility, resulting in an increase in resistivity. The spin of free electrons and magnetic moments of localized magnetic orbitals create the singlet state that remains down to ground state. Figure 1.7 depicts the process of Kondo singlet state formation in the single-impurity Kondo effect. The Kondo effect predicts that magnetic impurities yield a logarithmic temperature dependence to electrical transport¹⁶.

We can express the electrical transport in a 3D metal with magnetic impurities as follows:

$$\rho(T) = \rho_0 + AT^2 - B \ln\left(\frac{\mu}{T}\right) + CT^5 \quad (1.1)$$

where T is temperature, ρ_0 is residual resistivity and A, B, C, μ are constants which are independent of T . The logarithmic term grows at lower temperatures and becomes dominant in transport. The second term comes from the Fermi liquid behavior of electrons in metals. The last terms is connected to electron-phonon scattering.

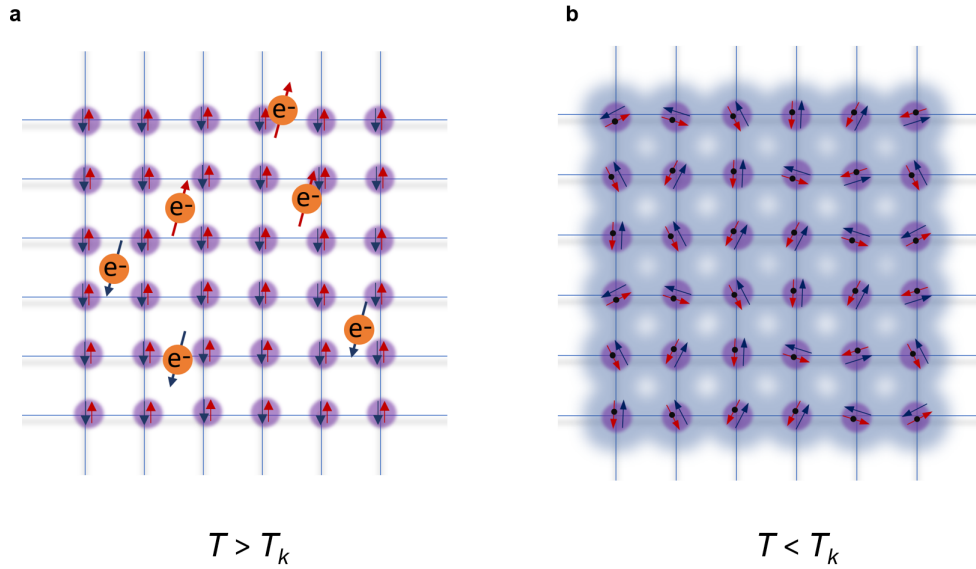


Figure 1.8: **a.** Schematic illustration of rectangular lattice containing localized heavy atoms with d or f orbitals at each sites with free electrons presented in orange color. The interaction between free electrons and localized f or d orbitals are weak when T is above T_k . **b.** When temperature is below T_k , the localized ions starts to form a singlet state with the spin of the conduction electrons. The system does not have any magnetic ordering, but it develops a coherent state which causes the sharp change in decreasing resistivity.

Now, consider a scenario in which the localized magnetic moments happen at each lattice site (Fig 1.8a). In this situation, the Kondo singlet state forms at each atomic point at temperature below T_K , and the spinless scattering sites become periodic (Fig 1.8b). This network formation is known as a

Kondo Lattice^{19,16}. The coupling strength between sites creates coherent states which causes a drop in the resistivity. The Kondo lattice forms in heavy fermionic systems consisting of rare earth materials with d and f orbitals with localized magnetic moments, such as Ce^{20,17,16}. Also, the Kondo effect can create resonant states at the Fermi surface. Single impurities lead to the formation of a single fermionic level which can be modelled as Anderson localization inside the system (Fig 1.9a). On the contrary, the Kondo lattice induces a new, heavy fermionic band in the density of states, with bandwidth T_K ¹⁶.

$$T_K \sim D e^{-1/2J\rho} \quad (1.2)$$

where D is the width of the electronic state, J is the interaction strength (effective coupling), and ρ is the density of states of the electrons. Based on the heavy Fermionic bands, we could have either Kondo metallic or Kondo insulating behaviour (Fig 1.9b).

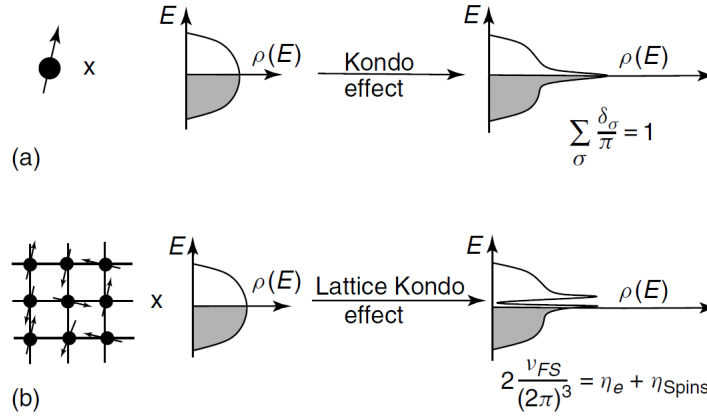


Figure 1.9: **a.** Single-impurity Kondo effect builds a single fermionic level into the electron conduction sea, which gives rise to a resonance in the conduction electron density of states. **b.** Lattice Kondo effect builds a fermionic resonance into the conduction sea in each unit cell. The elastic scattering of this lattice of resonances leads to the formation of a heavy electron band. [Reprint from P. Coleman 2006¹⁶]

In a Kondo lattice, the localized magnetic moments interact with each other through conduction electrons. These indirect interactions mediate in metallic environments and can give rise to magnetic

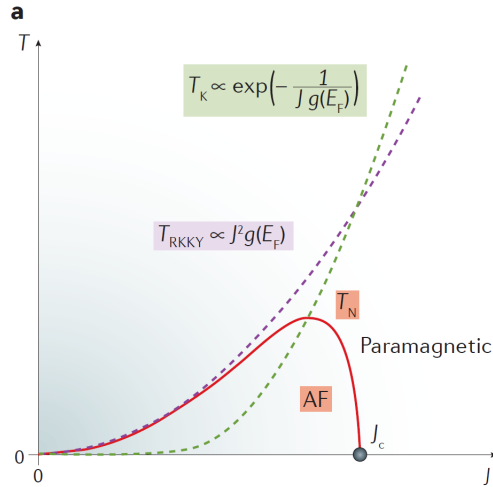


Figure 1.10: The dashed lines represent the dependence of the Kondo (green) and the Ruderman–Kittel–Kasuya–Yosida (RKKY; purple) interaction – represented by the dependence of the respective characteristic temperatures, T_K and T_{RKKY} , on the effective spin-exchange coupling parameter, J , between conduction electrons and local d or f electrons¹⁹. At the point where the two interactions have equal strength, the magnetic ordering temperature, T_N (represented by the solid red line), approaches zero and a quantum critical point (QCP) ensues if the transition from one ground state to the other is continuous. [Reprint from Steffen Wirth and Frank Steglich Nature 2016¹⁹]

ordering at low temperatures. Indirect exchange interactions at interatomic spacings between local moments occur due to Friedel oscillations of the conduction electron spin density. This polarization process happens in metals and is known as the Ruderman–Kittel–Kasuya–Yosida (RKKY) interaction¹⁶. The RKKY interaction depends on J^2 , coupling strength, and g , electron density of states, (Fig 1.10). The Kondo effect and RKKY interaction have competing contributions at low temperatures. RKKY terms can overcome the Kondo effect and form an antiferromagnetic (AFM) or spin density wave (SDW) ground state in heavy fermionic systems. In the bulk of heavy fermion materials, the interplay between the (RKKY) interaction, which induces magnetic ordering, and the Kondo effect, which determines the ground state, can be tuned using external parameters (e.g., pressure, magnetic or electric field) to the brink of a quantum phase transition where various exotic quantum phenomena can emerge (Fig 1.10). The Doniach phase¹⁹ space diagram depicts different states of spin for a general heavy fermionic system. We can use non-thermal tuning parameters (δ), such magnetic field

or pressure, to tune the ground state of the system, and consequently study the exotic phenomena occurring near the quantum criticality point.

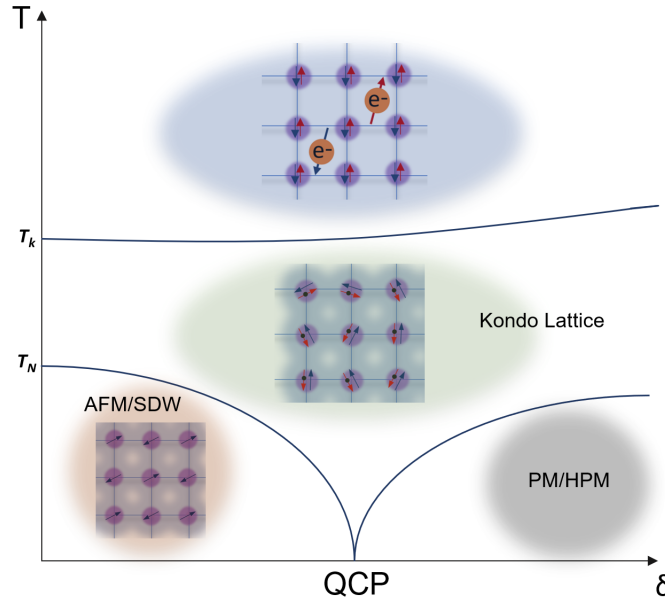


Figure 1.11: δ is an external, non-thermal control parameter used to tune the material through the quantum critical point (QCP). The blue area which is above T_K indicates the phase space in which electrons interact weakly with local magnetic moments. The green shaded indicates Kondo lattice formation. Competition between Kondo and RKKY leads to an ordered state when T is lower than T_N . AFM, antiferromagnetic; SDW, spin density wave; PM/HPM paramagnetic state or Heavy paramagnetic state; T_K , Kondo temperature; T_N , Néel temperature.

1.5 OVERVIEW OF THIS THESIS

In the following chapters, we will first discuss the intercalation dynamics at the microscopic scale by developing a new electrochemical cell method. Exceeding the performance limits of metal-ion battery technologies mandates the discovery of new approaches to tune the fundamental properties of electrode materials. While composites of layered materials have drawn relatively recent attention as high capacity battery anodes, the precise role of heterolayers in modifying intercalation reactions remains unclear. Previous studies represented ensemble measurements of macroscopic films or pow-

ders, which lacked the specificity to isolate and probe the 2D interfaces individually^{21,22}. Paradigm shifts in batteries, ion separation, electronics, and a myriad of other technologies will require isolation and identification of the fundamental electrochemical characteristics of 2D heterointerfaces to enable rational materials design. In chapter 2, we prepare individual vdW intercalation heterostructures of graphene and transition metal dichalcogenide (TMDC) layers that are encapsulated between layers of inert hexagonal boron nitride (hBN). We establish several operando experimental tools such as Hall voltammetry and intercalation frontier imaging to monitor the course of the electro-intercalation Li^+ reaction at the mesoscopic 2D heterointerfaces. The high quality of our 2D intercalated heterostructures permits us to use low-temperature quantum transport methods in conjunction with spectroscopy to identify the fundamental layer capacities and equilibrium potentials of individual 2D layers.

In chapter 3, we demonstrate the intercalation of AlCl_4^- ions into van der Waals heterostructure layers consisting of deterministically stacked hexagonal boron nitride (hBN) and few layer graphene. We use magnetoresistance charge transport and operando optical microscopy to evaluate the dynamics of intercalation processes in atomically thin samples. We develop a colorimetric method to estimate the diffusion coefficient in variable temperature.

In chapter 4, we cover electrical transport studies of two novel layered materials. Here, studies of single crystals of two 2D MOFs, $\text{Ni}_3(\text{HITP})_2$ and $\text{Ni}_3(\text{HHTP})_2$, uncover critical insights into their structure and transport. Conductivity measurements down to 0.3 K suggest metallicity for mesoscopic single crystals of $\text{Ni}_3(\text{HITP})_2$, which contrasts with apparent activated conductivity for polycrystalline films. Notably, single rods exhibit conductivities up to 150 S/cm, which persist even after prolonged exposure to the ambient environment. Also, we perform Hall effect measurements in single crystal $\text{Ni}_3(\text{HHTP})_2$. These single crystal studies confirm that 2D MOFs hold promise as molecularly tunable platforms for fundamental science and applications where porosity and conductivity are critical. In the second part of chapter 4, we introduce the newest member of the graphene

family. The two natural allotropes of carbon, diamond and graphite, are extended networks of sp^3 and sp^2 hybridized atoms, respectively. By mixing different hybridizations and geometries of carbon, one could conceptually construct countless synthetic allotropes. Here we introduce graphullerene, a new two-dimensional (2D) crystalline polymer of C_{60} that bridges the gulf between molecular and extended carbon materials. Its constituent fullerene subunits arrange hexagonally in a covalently interconnected molecular sheet. We report charge-neutral, purely carbon-based macroscopic crystals that are large enough to produce, via mechanical exfoliation, molecularly-thin flakes with clean interfaces, a critical requirement for the creation of heterostructures and optoelectronic devices. We explore the electrical conductivity of this material. More broadly, the synthesis of extended carbon structures by polymerization of molecular precursors charts a clear path to the systematic design of new materials for construction of 2D heterostructures with tunable optoelectronic properties.

In chapter 5, we introduce the newest candidate for heavy fermions with layered structure. We report electrical transport of atomically thin CeSiI. Heavy fermion metals can host exotic quantum phenomena such as Kondo lattices, unconventional superconductivity, and quantum criticality. Our study of an atomically thin 2D heavy fermion system provides a new route to explore low dimensional strongly correlated systems. Heavy fermion metals are prototype systems for the observation of emergent quantum phases driven by electronic interactions. A longstanding aspiration has been to control these quantum phases by reducing the dimensionality of the host compounds. This remains a significant challenge because traditional intermetallic heavy fermion materials have three-dimensional atomic structures. Here we report comprehensive thermodynamic and spectroscopic evidence of a heavy fermion ground state in CeSiI, a layered antiferromagnetic metal composed of 2D sheets held together by weak vdW interactions. The vdW structure of CeSiI allows us to control its physical dimension using mechanical exfoliation. The electrical transport properties of few-layer flakes reveal heavy fermion behavior and magnetic order down to the ultra-thin regime. Our work offers unique opportunities to apply well-established mechanical exfoliation and transfer methods to understand

and manipulate Kondo screening, magnetism, and proximity effects in heavy fermion systems. In this chapter, we also discuss how the verification of the 2D electronic system and the inherent layered structure of CeSiI makes 2D transport an exciting avenue to explore the effect of dimensionality on its heavy fermion behavior. With the air sensitivity exhibited by bulk crystals, exfoliated flakes are more reactive, and because of this increased reactivity, device fabrication is extremely complex.

Finally, I will end this thesis by projecting a potential outlook from the projects presented in this thesis.

2

Electrochemical intercalation into van der Waals heterostructures

2.1 INTRODUCTION

Increasing the amount of electronic and ionic charge is the preeminent chemical challenge for electrochemical energy storage devices like supercapacitors and batteries^{21,22,23,24}. Conventional routes to

modifying the fundamental redox properties of electrode materials include alloying and partial substitution/doping. These approaches inherently mandate chemical and structural compatibility between substitute and parent compound for synthesis. The assembly of layered vdW materials into novel heterostructures relaxes the requirements on crystallographic commensurability across interfaces and enables the creation of atomically precise superlattices⁴ that may be synthetically intractable by chemical growth. Intrinsically, this stacking of vdW layers creates unique 2D interlayer galleries that are absent from bulk materials, and which may be electrochemically driven to accommodate ions for energy storage^{24,25,26}. Since intercalation necessarily involves some form of chemical bond formation between host and guest, this atomistic control over the coordination environment of an intercalant species introduces the possibility of preparing a myriad of new complex materials with uniquely tailored heterointerfaces that, in principle, may be capable of accommodating more/less intercalants (controlling capacity), altering intercalation potentials (modifying thermodynamic landscapes) and/or influencing ion conduction through the interlayer gap (regulating ion diffusion kinetics). The recently developed “Hall potentiometry” (HP) method²⁷, together with low-temperature quantum transport measurements, directly probes the intercalation process at atomic interfaces to reveal novel synergistic effects of intimate face-to-face vdW contact between multiple redox-active 2D layers in a prototypical carbon/metal dichalcogenide system. A complementary potentiostatic technique has elucidated rapid diffusion of Li in graphene bilayers²⁸. In this chapter I will study the Li intercalation into Van der Waals heterostructures.

2.2 ELECTROCHEMICAL DOPING & INTERCALATION

To examine the role of the vdW heterointerface in intercalation, we have assembled layers of graphene, molybdenum dichalcogenides (MoX_2 , $\text{X} = \text{S}, \text{Se}$), and hBN into the series of five heterostructures shown in Figure 2.1a using vdW assembly²⁹. Structure I was the subject of our previous studies and is

included in this study as a point of comparison²⁷. These device architectures are interrogated singularly as the working electrodes (WEs) of on-chip micro-electrochemical cells as shown in Figures 2.1b and c. Using the Hall voltammetry method (see Appendix A for details), we can monitor both the longitudinal resistance, R_{xx} , of the heterostructure WE as well as the Hall carrier density, n_H and by extension, the progress of the electrochemical reaction at this mesoscopic system while the reaction driving force (potential) is altered.

Fig. 2.2 presents results for electro-intercalation of a heterostructure stack of Structure II. This heterostructure is stack of (hBN/MoS₂/G/hBN). From the behaviors of R_{xx} and n_H as a function of applied potential E , four distinct phases (Phase 1–4) in the electrochemical data can be distinguished corresponding to intermediate stages in the electrochemical reaction of the MoS₂/G heterostructure. This in-situ monitoring of R_{xx} and n_H provides more direct information of intercalation staging than that of the traditional electrochemical approach using linear sweep or cyclic voltammetry, in which the overall electrochemical response is also influenced by any charge transfer reactions at the solid–solution interface of the metal contacts. The transport features in Phase 1 (for $E > -2.3$ V) replicate the purely electrostatic doping behavior observed in electric double layer gating of graphene^{30,31}. As we apply an increasingly negative voltage E , several intercalation processes occur, revealed by pronounced jumps in R_{xx} and n_H . The latter features in phases 3 and 4, specifically the peak in R_{xx} that occurs in concert with the surge in n_H , are key signatures of ion intercalation involving a high mobility graphene layer. The intercalation process engenders a decline in electron mobility as Li⁺ ions become closely associated with the graphene lattice and act as scattering sites for mobile electrons. Ultimately the resistance is driven back down as mounting carrier densities supersede this sudden decrease in mobility²⁷. We find that the deintercalation process (by sweeping E toward 0 V potential) reverses doping and recovers R_{xx} and n_H values similar to those of the pristine heterostructure (Fig. 2.3).

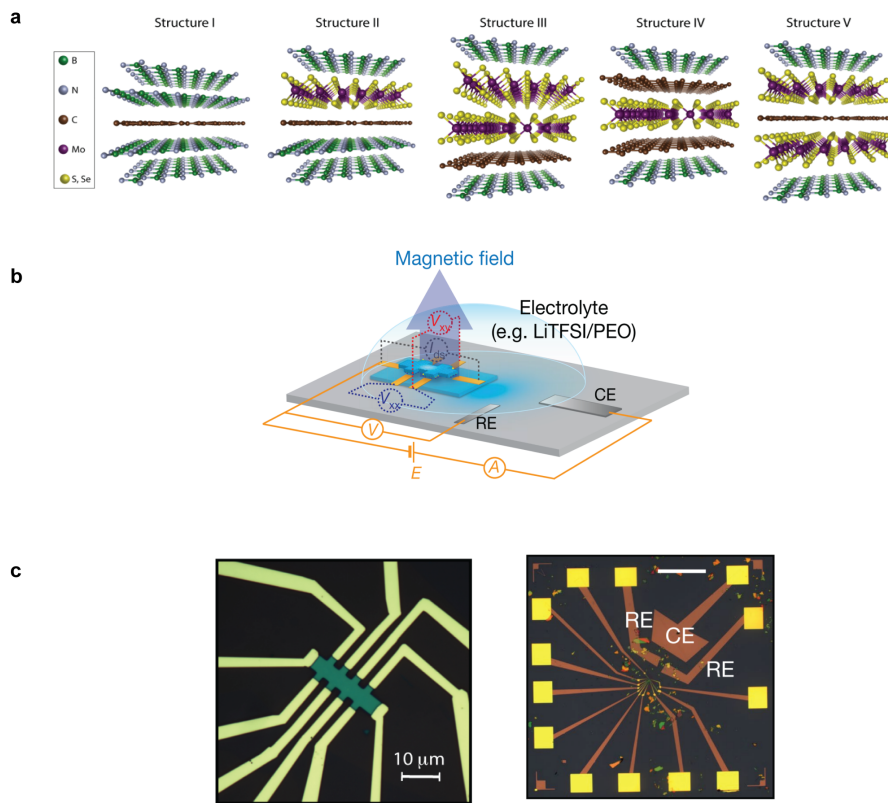


Figure 2.1: **a**, Schematic diagram of the heterostructure series employed for investigation of heterolayers on intercalation capacities and thermodynamics. **b** Schematic model of mesoscopic electrochemical cell where the electrochemical potential, E , is applied between the working electrode consisting of a vdW heterostructure and the counter electrode for controlled intercalation. Magnetic fields are applied perpendicular to the heterostructure plane and a small AC current I_{ds} is applied along the heterostructure. Magnetoresistance and Hall resistance R_{xx} and R_{xy} are obtained from the longitudinal and transverse voltages, V_{xx} and V_{xy} by taking their respective ratios to I_{ds} . R_{xx} and R_{xy} are measured during the intercalation process by sweeping E in the presence of the electrolyte and the results are compared to the cyclic voltammetry obtained by monitoring the “leakage” current (A). **c**, Optical micrographs of an on-chip electrochemical cell for charge transport and optical measurements during electro-intercalation. Scale bars: left, $500 \mu m$; right, $10 \mu m$.

2.3 LOW-TEMPERATURE CHARGE TRANSPORT AND MAGNETORESISTANCE ANALYSIS

Our unique capabilities for in-situ characterization of electrical properties of electrochemically-modified vdW structures offer an elegant route to probe the distribution of charge on each 2D layer after intercalation. To uncover these details, we performed low temperature magnetotransport studies in the in-

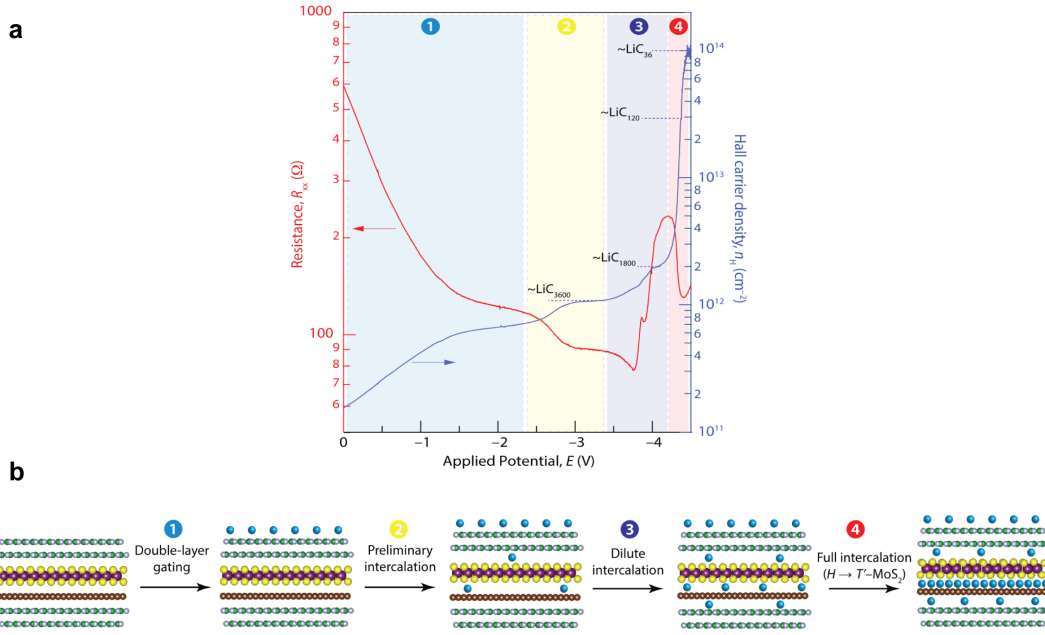


Figure 2.2: . a, Two-electrode “Hall potentiogram” recorded at 325 K for a graphene–MoSe2 device, showing the change in four-terminal longitudinal resistance, R_{xx} and Hall carrier density, n_H (in the presence of a perpendicular magnetic field of 0.5 T) as a function of applied potential between heterostructure and the counter electrode. Four distinct phases of the intercalation are emphasized along with the approximate stoichiometries of lithium–carbon centers as the sweep progresses. b, Mechanism of vdW heterostructure intercalation based on experimental data.

tercalated vdW heterostructures. Fig. 2.4a presents the magnetoresistance R_{xx} and Hall resistance R_{xy} for a fully intercalated Structure II device at 1.8 K. R_{xy} is linear in magnetic field B from which we estimate n_H equal to $1.0 \times 10^{14} \text{ cm}^{-2}$. R_{xx} exhibits a pronounced peak near $B = 0$, presumably related to the weak localization behavior due to intervalley scattering of intercalated Li^+ ions²⁸. As B increases, we observe well-defined Shubnikov-de Haas (SdH) oscillations^{32,33}, for $B > 3$ T, signifying a high quality 2D electron gas (2DEG) and homogeneity of the lithium-intercalated heterostructure. SdH oscillations in $R_{xx}(B)$ arise due to the formation of Landau levels at high magnetic fields. Plotting $R_{xx}(B)$ as a function of B^{-1} confirms that these oscillations are periodic in B^{-1} with a frequency B_F . The associated carrier density of the 2DEG, n_{SdH} , can then be determined from the relation:

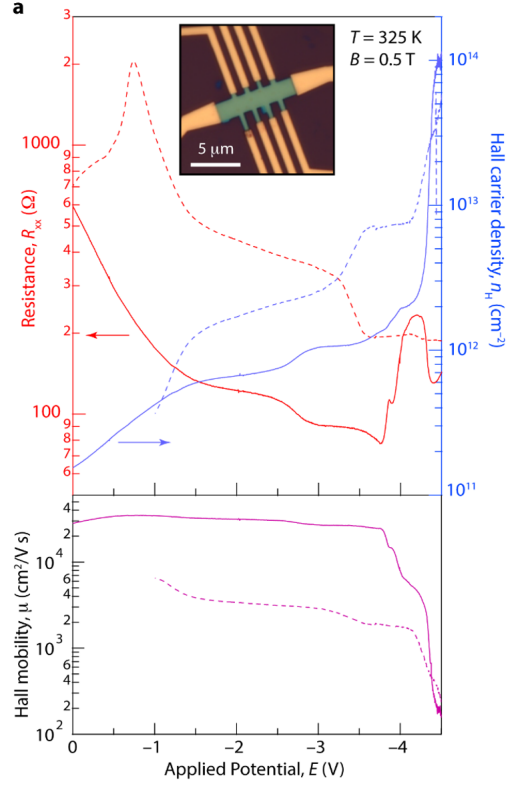


Figure 2.3: Forward (solid lines) and reverse (dashed lines) sweeps of four-probe resistance (red), Hall carrier density (blue), and Hall mobility (purple) as a function of potential at the heterostructure (vs. the counter electrode/electrolyte gate—i.e. in a two-electrode electrochemical configuration) in a LiTFSI/PEO electrolyte at 325 K in the presence of a magnetic field, $B = 0.5$ T. Inset: optical micrograph of heterostructure stack working electrode.

$$n_{SdH} = \frac{g \times e \times B_F}{h} \quad (2.1)$$

where g is the Landau level degeneracy, e is the elementary charge and h is Planck's constant. For these electron-doped graphene or MoX_2 layers, it is reasonable to take g as close to 4. Spin-valley locking in the valence band of H- MoX_2 layers gives rise to degeneracies close to 2, whereas the conduction band-edges are almost spin degenerate leading to degeneracies closer to 4 for electron-doped H- MoS_2 . The periodicity of SdH quantum oscillations with B^{-1} (Fig. 2.4b) unveils a carrier den-

sity n_{SdH} on the order of $2 \times 10^{13} \text{cm}^{-2}$, which is five-fold smaller than the total density, n_H estimated from Hall measurement. This discrepancy between n_{SdH} and n_H lies in stark contrast with those observed for Structure I, and is consistent with a two-channel electronic system, where a higher mobility 2DEG produces SdH oscillations corresponding to a lower density $n_{SdH} < n_H$, while another channel contains the vast majority of electron density ($n_H - n_{SdH}$).

For further quantitative analysis of the electronic band, we measure the SdH behavior at different temperatures, T (Fig. 2.4b). The decreasing oscillation amplitude with increasing T is linked to the effective mass (m^*) of electrons. The effective mass, m^* , of the band giving rise to SdH oscillations is determined from the temperature dependence of the SdH amplitude, ΔR_{xx} (Fig. 2.4b), by fitting these data to the Lifshitz–Kosevich theory^{32,33},

$$\Delta R_{xx}(B, T) \propto \frac{\frac{\alpha T}{\Delta E_N(B)}}{\sinh\left(\frac{T}{\Delta E_N(B)}\right)} e^{\left(\frac{-\alpha T_D}{\Delta E_N(B)}\right)} \quad (2.2)$$

$$\Delta E_N(B) = \frac{heB}{2\pi m^*} \quad (2.3)$$

$$T_D = \frac{h}{4\pi^2 \tau k_B} \quad (2.4)$$

$$\alpha = 2\pi^2 k_B \quad (2.5)$$

where B is the magnetic field position of the N th minimum in R_{xx} , $\Delta E_N(B)$ is the energy gap between the N th and $(N+1)$ th Landau levels (m^* is the effective mass, e is the elementary charge, and h is the Planck constant), T_D is the Dingle temperature, k_B is Boltzmann's constant, τ_q is the quantum lifetime of carriers, and α is the momentum space area including spin degeneracy. In our experiment, ΔE_N and T_D are the only two fitting parameters. The pre-exponential in this expression is the only temperature dependent portion and permits the straightforward determination of m^* and τ .

Fitting SdH data using the standard Lifshitz-Kosevich formalism (2.2), we obtained $m^* = 0.11m_0$

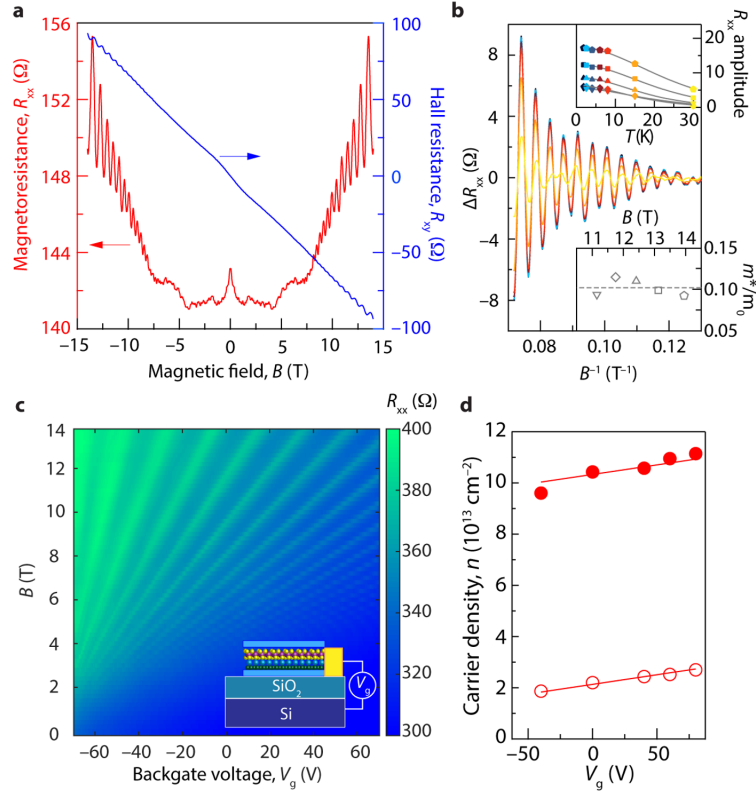


Figure 2.4: **a**, Four-terminal magnetoresistance, R_{xx} and Hall resistance, R_{xy} as a function of perpendicular magnetic field strength, B , for a Structure II graphene-MoS₂ device after intercalation at $E = -5$ V. Hall carrier density, n_H , is determined to be $1.0 \times 10^{14} \text{ cm}^{-2}$. **b**, ΔR_{xx} , determined from R_{xx} by subtraction of a polynomial fit to the magnetoresistance background as a function of the reciprocal magnetic field strength, B^{-1} , at various temperatures. Shubnikov-de Haas oscillations (SdH) possessing a periodicity of $4.47 \times 10^{-3} \text{ T}^{-1}$ are observed, consistent with a carrier density, n_{SdH} , of $2 \times 10^{13} \text{ cm}^{-2}$. Top inset shows the temperature dependence of SdH amplitude at five values of B . Solid lines depict the fit to the data according to the Lifshitz-Kosevich formalism. Bottom inset shows effective masses, m^* , extracted from fits at different values of B , all around $0.1m_0$ (where m_0 is the free electron mass $\sim 9.11 \times 10^{-31} \text{ Kg}$). **c**, **d**, Dependence of charge transport on backgate voltage, V_g . **c**, Landau fan diagram $R_{xx}(V_g, B)$ after intercalation, evincing a robust dependence of n_{SdH} on V_g , consistent with the underlying graphene layer as the origin of quantum oscillations in these heterostructures. Inset shows schematic of the intercalated heterostructure used with the graphene layer beneath MoS₂. **d**, V_g dependence of n_{SdH} (open circles) and n_{Hall} (filled circles). The lines represent fits assuming a Si backgate capacitance of $1.2 \times 10^8 \text{ F cm}^{-2}$.

(m_0 is the electron rest mass), close to the value of $0.099m_0$ that we obtain for intercalated Structure I (hBN/graphene/hBN) doped to a density of $2 \times 10^{13} \text{ cm}^{-2}$ (additional transport quantities are summarized in Table 1, fig 2.7). We also characterize the low temperature magnetotransport as a function of back gate voltage V_g applied to the underlying Si substrate (Figs. 2.4c and d). For Structure II, studied above, the graphene monolayer channel is positioned in closer proximity to the back gate, underneath the MoS₂ channel (Fig. 2.4c inset). From the Landau fan diagram (Fig. 2.4c), where R_{xx} is plotted as a function of both V_g and B , we observe that the SdH quantum oscillations are strongly dependent on V_g , pointing to the graphene as the origin of the magneto-oscillations. Were it the case that the MoS₂ layer served as the origin of the SdH oscillations, the SdH channel would be electrostatically screened by graphene and the associated density would therefore be independent of V_g . Correspondingly, we find that n_{SdH} and n_H exhibit the same dependence on V_g (Fig. 2.4d), consistent with the bottom-graphene layer (ca. 10^{13} cm^{-2}) serving to shield the overlying MoS₂ sheet (ca. 10^{14} cm^{-2}) from the electrostatic influence of V_g . In this picture, the dependence of the total density, given by n_H , simply follows the dependence of one of its components n_{SdH} . We estimate the backgate capacitance, $C = 1.2 \times 10^8 \text{ F cm}^{-2}$ using $\Delta n_H = CV_g/e$, whose value is in a good agreement with the thickness of SiO₂ and hBN layers serving as the gate dielectric.

Having established that the carrier density distribution of these heterostructures lies strongly on the metal dichalcogenide layer, we expected that an increase in the number of dichalcogenide layers to two (Structure III) would simply furnish carrier densities well in excess of those observed for Structure II. Interestingly, we observe that intercalation of Structure III stacks ($n_H = 1.4 - 1.9 \times 10^{14} \text{ cm}^{-2}$, Data Fig. 2.5) does not lead to carrier densities in excess of typical Structure II samples, suggesting that it is the G/MoS₂ heterointerface that harbors the vast majority of intercalated ions as opposed to hBN/MoX₂ or MoX₂/MoX₂ interfaces. A significant benefit to our device-based approach to electrochemistry and our method of deterministically assembling 2D layers with designed interfaces is the possibility to directly compare electrochemical reactions at different 2D heterointerfaces. By

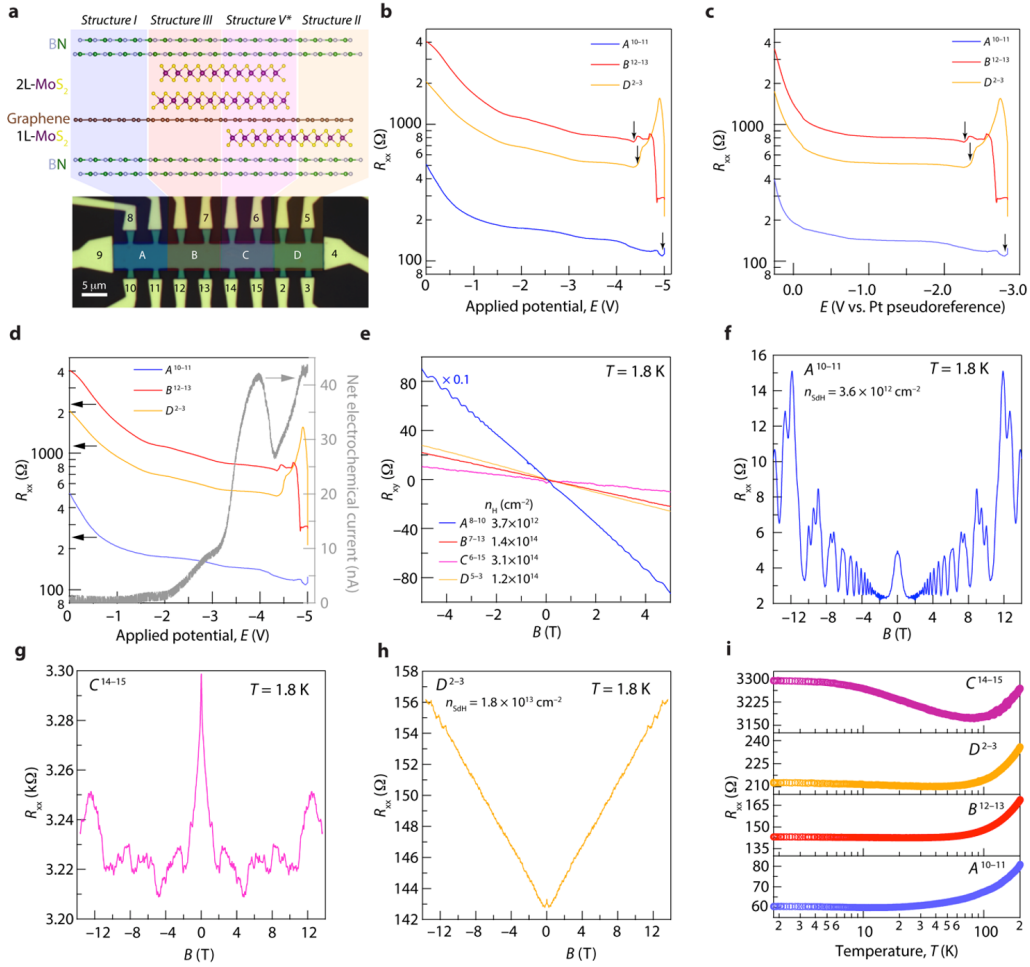


Figure 2.5: a, Optical micrograph (false color) of a device consisting of multiple hBN-encapsulated graphene–MoS₂ heterostructure types (depicted in the associated illustration) arrayed along a single graphene monolayer. b,c, Zonal resistances as a function of potential in a two–potential versus counter–(b) and three–potential versus Pt pseudo reference (c)–electrode electrochemical configuration in a LiTFSI/PEO electrolyte at 325 K in the presence of a magnetic field, B, of 0.5 T. Electrochemical doping of three regions of the device in a (demarcated by the assigned contact number) are monitored. Intercalation (indicated by the arrows) initiates at 0.6 V more positive potentials at zones B and D (structures III and II) than at A (structure I). d, Conventional cyclic voltammetric electrochemical current response (gray) of the entire device overlaid with the resistances of the various device regions over the course of the sweep. CV cannot distinguish between the intercalation of G/MoS₂ and G/hBN regions in this device. e, Hall resistance, R_{xy} , as a function of magnetic field at 1.8 K for the different regions of the device after electrochemical polarization up to -5.0 V, displaying the resulting Hall carrier densities obtained. f–h, magnetoresistance data at 1.8 K for zones A (f), C (g), and D (h), showing associated SdH carrier densities, n_{SdH} extracted from the periodicities of oscillations in B^{-1} . i, Temperature dependence of resistance for the various device regions between 200 and 1.8 K during warming.

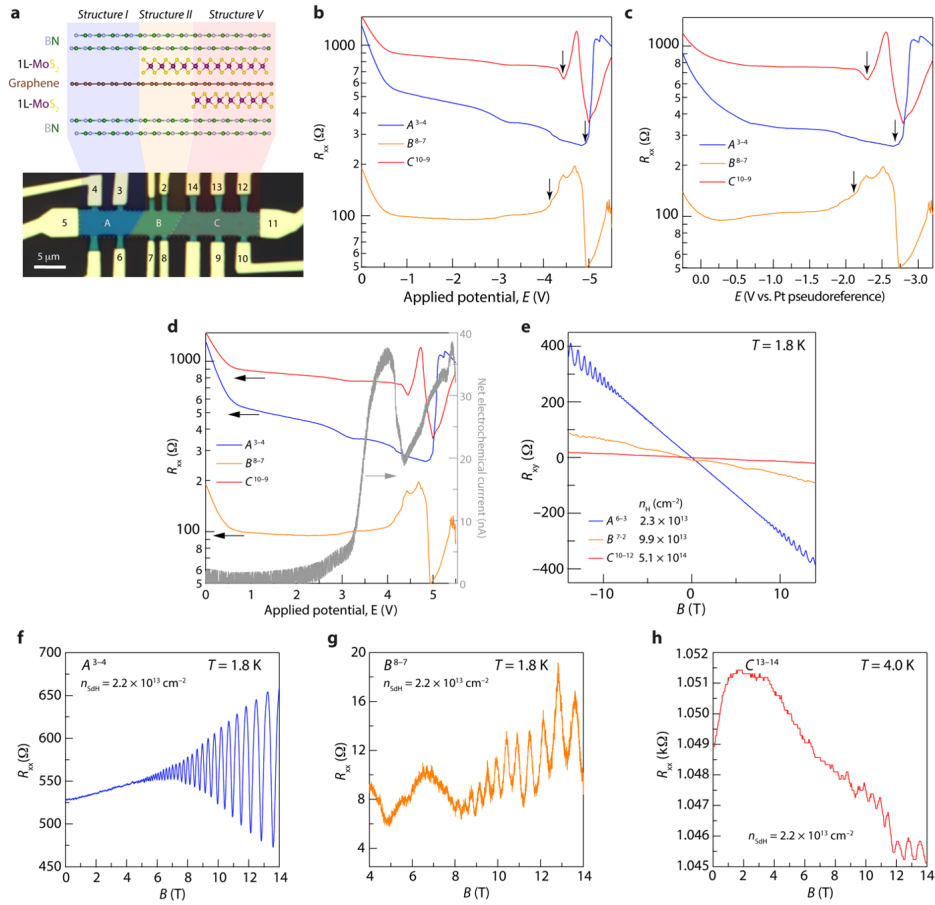


Figure 2.6: Optical micrograph (false color) of a device consisting of multiple hBN-encapsulated graphene-MoS₂ heterostructure types (depicted in the associated illustration) arrayed along a single graphene monolayer. b,c, Zonal resistances as a function of potential in a two-potential versus counter-(b) and three-potential versus Pt pseudo reference (c)-electrode electrochemical configuration in a LiTFSI/PEO electrolyte at 325 K in the presence of a magnetic field, B , of 0.5 T. Electrochemical doping of the three regions of the device in a (demarcated by the assigned contact number) are monitored. Intercalation (indicated by the arrows) initiates at ~ 0.7 V more positive potentials at zones B (Structure II) and C (Structure V) than at zone A (Structure I). d, Conventional cyclic voltammetric electrochemical current response (gray) of the entire device overlaid with the resistances of the various device regions over the course of the sweep. CV cannot distinguish between the intercalation of G/MoS₂ and G/hBN regions in this device. e, Hall resistance, R_{xy} , as a function of magnetic field at 1.8 K for the different regions of the device after electrochemical polarization up to -5.5 V, displaying the resulting Hall carrier densities obtained. f-h, Magnetoresistance data at 1.8 K for regions A (f), B (g), and C (h) that reveal associated SdH carrier densities, n_{SdH} from the periodicities of oscillations.

Parameter	Structure I	Structure II
	Intercalated ($E = -5.5$ V) hBN/Graphene/hBN	Intercalated ($E = -5.0$ V) hBN/MoS ₂ /graphene/hBN
n_H	$2.3 \times 10^{13} \text{ cm}^{-2}$	$1 \times 10^{14} \text{ cm}^{-2}$
n_{sdH}	$2.2 \times 10^{13} \text{ cm}^{-2}$	$2.0 \times 10^{13} \text{ cm}^{-2}$
m^*	$0.099m_0$	$0.11m_0$
T_D	30.5 K	36.2 K
τ_q	39.9 fs	33.6 fs
l	40 nm	34 nm
μ_q	$712 \text{ cm}^2 \text{ V}^{-1} \text{ s}^{-1}$	$557 \text{ cm}^2 \text{ V}^{-1} \text{ s}^{-1}$
μ_{Hall}	$462 \text{ cm}^2 \text{ V}^{-1} \text{ s}^{-1}$	$270 \text{ cm}^2 \text{ V}^{-1} \text{ s}^{-1}$

Figure 2.7: Comparison of transport parameters for two classes of intercalated heterostructures. The relative similarity in quantum scattering time and mean free compound support for the contention that SdH oscillations observed for intercalated Structure II arise from the graphene sublayer

creating heteroarchitectures wherein we design in-plane variations to the structure type along a single graphene monolayer, as depicted in Fig. 2.6a, we quantitatively examine the dichalcogenide hetero-layer effect. Simultaneous measurement of the transport characteristics at different lateral sections of the heterostructure devices during electrochemical polarization (Fig. 2.8b) reveals that the onset of G/MoX₂ intercalation takes place at about $\Delta E^0 = +0.5 \text{ to } +0.75 \text{ V}$ vs. that of G/hBN. Notwithstanding the significantly more negative potential that MoX₂ layers are subjected to, it is noteworthy that the dichalcogenides in these G/MoX₂ heterostructures are not decomposed to lithium polychalcogenides as occurs in the bulk³⁴, indicating a widened window of electrochemical stability. An effect of dimensional confinement on the conversion reaction voltage has been previously observed in MoS₂/carbon-nanofiber hybrids³⁵. In these systems, the outstanding cycling performance is attributed to the restriction of polysulfide/Mo^o nucleation and confinement of product diffusion. We anticipate that such mechanisms could be pronounced in these 2D heterostructures. Low temperature plots of Hall resistance, R_{xy} , as a function of magnetic field (Fig. 2.8b, bottom left) allow us to precisely identify the total carrier density (and for that matter, lithium ion capacity) in each re-

gion of the device. Consequently these vdW stacks unequivocally demonstrate the critical role of direct graphene–MoX₂ heterointerfaces in markedly enhancing the carrier/charge capacities in vdW heterostructure electrodes. We find that sandwiching a graphene monolayer between layers of MoX₂ (Structures V and V*), thereby creating two graphene–dichalcogenide heterointerfaces produces intercalation capacities more than double those of the “isomeric” Structure III region within the same device (Fig. 2.8b, bottom right). Similar intercalation behaviors were observed in multiple devices, confirming the proposition of using intimate vdW contact between different 2D layers as a means of favorably manipulating the equilibrium potentials and capacities in intercalation electrodes. The intercalation onset potentials of the different structures (Figure 2.8c) emphasize that G/MoX₂ interfaces dominate the intercalation properties, since the onset of intercalation is effectively identical across Structures II to V, and distinctly lying between those of Structure I and bulk MoX₂. Capacities (Fig. 2.6c inset) as high as $6.2 \times 10^{14} \text{cm}^{-2}$ are attainable in Structure V devices. However, in all these structures, the graphene density (n_{SDH}) exhibits a maximum value of $\sim 2 \times 10^{13} \text{cm}^{-2}$, indicative of a strong preference for charge transfer to the dichalcogenide layers ($\sim 3 \times 10^{14} \text{cm}^{-2}$ each). Assuming additive Li⁺ capacities, we can estimate the electrochemically accessible capacity of each vdW interface as plotted in Figure 2.8d, showing the ≥ 10 -fold superiority of the G/MoS₂ interface compared to other interfaces. Therefore, the atomic heterointerfaces of vdW materials represent a new material platform to realize engineered functional interfaces for energy conversion and storage. These results highlight the criticality of the graphene heterolayer in enhancing electrochemical charge accumulation in MoX₂ while also directing intercalation at a more negative voltage than that of bulk MoX₂.

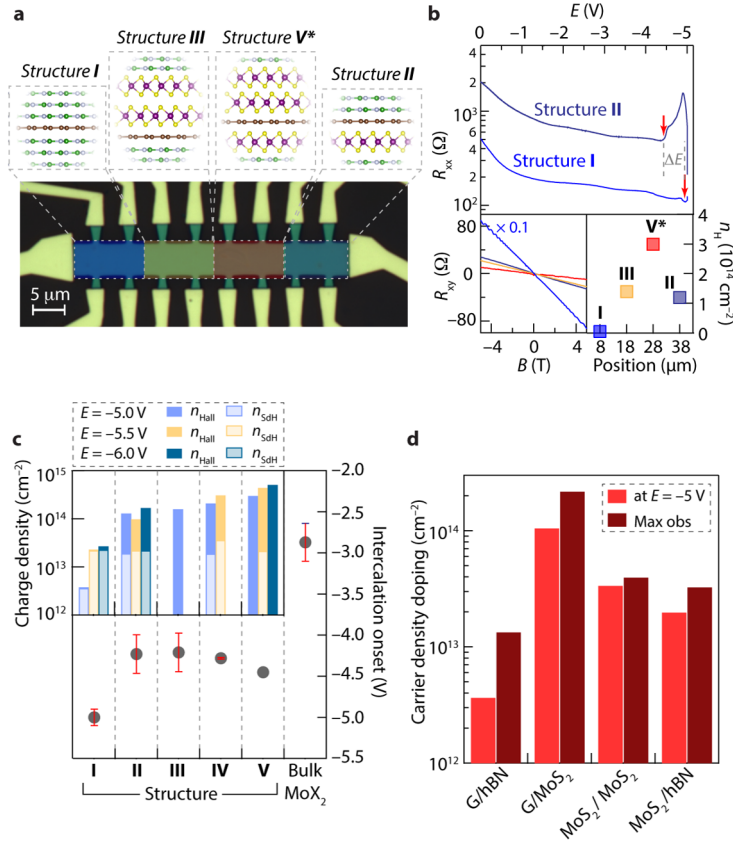


Figure 2.8: a, Optical micrograph (false color) of a device consisting of multiple hBN-encapsulated graphene–MoS₂ heterostructure types (depicted in the associated illustration) arrayed along a single graphene monolayer. Scale bar: 5 μm . b, Top: Four terminal resistance, R_{xx} , as a function of applied potential during electrochemical gating of two regions of the device in a demarcated by the assigned contact number. Intercalation (revealed by the sudden rise in resistance indicated at the red arrows) proceeds at $\Delta E^0 \sim 0.6\text{V}$ more positive potentials at the graphene–MoS₂ interface than at the graphene–hBN interface. Bottom left: Hall resistances, R_{xy} , as a function of applied field, B, following polarization of the device in a to -5.0V . Bottom right: Hall carrier densities determined from contacts in each of the four regions of the device. c, Onset potentials from intercalation of vdW heterostructures and bulk MoX₂ devices. Inset: Mean charge densities (intercalation capacities) achieved after intercalation of devices based on Structures I–V. Hall carrier densities (n_H), indicative of the total density in the heterostructure, are depicted by the overall bar height, whereas the graphene partial carrier densities determined from SdH quantum oscillation data (where available) are indicated by the lighter sub-bars. d, Estimated doping level of each interface based on results in c.

2.4 RAMAN & PHOTOLUMINESCENCE SPECTROSCOPY STUDIES

While the transport in the intercalated MoS₂/G is largely dominated by conduction through high mobility graphene, as we will discuss later, further insight into the participation of MoS₂ in this elec-

trochemical reaction is provided by operando Raman and photoluminescence (PL) spectroelectrochemistry. Fig. 2.9a shows PL data acquired over the course of an E sweep revealing distinct changes to the optical profile of the semiconducting $1H-$ (D_3h symmetry) MoX_2 layer. Specifically, we find the PL peak consistent with the formation of negatively charged trions (A)³⁶ appears at the later stage of intercalation process ($E < -3$ V), signifying strong n-doping in MoS_2 layer. These data indicate that a highly doped $1H-\text{MoS}_2$ phase persists immediately prior to the main intercalation stage, beyond which the PL is fully quenched and Raman (Fig. 2.10a) spectral features of the MoS_2 (and graphene) layer are lost due to Pauli blocking^{27,37,34}. Deintercalation by reversing the polarization back to 0 V recovers the original graphene spectral features, yet reveals marked changes in the Raman spectrum of MoS_2 as shown in Figure 2.9b. Most conspicuously, a series of weak, low wavenumber peaks between ~ 150 and 230 cm^{-1} emerge. These peaks grow in intensity with increasing number of MoS_2 layers, confirming their association with the dichalcogenide and are still present, albeit slightly diminished, after annealing for 1 h at 300°C (Figure 2.9b, inset). In contrast the Raman peaks for the E_{2g}^1 and A_{1g} modes recover some spectral intensity after annealing. The aforementioned changes in PL and Raman response are even more clearly observed in the corresponding spectroscopic spatial maps (Figs. 2.9c–f and Figure 2.10c–g). These spectroscopic results are as expected for an intercalation-induced structural phase transition from the semiconducting H phase to a metallic T (D_3d symmetry with octahedral Mo coordination)-type phase with an additional lattice distortion (usually denoted as T'), which is favored upon intercalation and/or electron doping of $2H-\text{MoS}_2$ ^{38,39,40}. This phase is metallic and therefore the PL is strongly quenched. The low wavenumber Raman features are characteristic of the so-called “J” modes of T and T' phases of MoS_2 ^{41,42,43,44}. The 154 and 226 cm^{-1} peaks are attributed to the J_1 and J_2 modes of $T'-\text{MoS}_2$ and the 184 cm^{-1} feature is assigned to the J_1 mode of $T-\text{MoS}_2$. The corresponding J_2 mode for $T-\text{MoS}_2$ is expected at $\sim 203 \text{ cm}^{-1}$ and therefore explains the low wavenumber tail of the $T' J_2$ peak as seen in Figure 2.9b. Notably, we have not observed the emergence of any Raman signatures for lithium polysulfides (746 cm^{-1}) during the

entire intercalation–deintercalation processes, suggesting the overall chemical integrity of MoS₂ remained intact upon lithiation, with a mixed phase of metastable T' - and T'' -MoS₂ persisting upon deintercalation, and partial recovery of H -MoS₂ after annealing. We also performed magnetotransport measurements to determine carrier densities induced by intercalation. The total carrier densities for Structure II stacks attain values approaching $n_H = 2 \times 10^{14} \text{cm}^{-2}$, between three and ten-times the maximal densities observed for intercalated Structure I ($n_H = 2 - 7 \times 10^{13} \text{cm}^{-2}$)²⁷.

2.5 TRANSMISSION ELECTRON MICROSCOPY OF INTERCALATION PROCESS

Finally, to develop a more comprehensive understanding of the mechanism of intercalation at these 2D interfaces and to inform our explanation of these differences in interface capacity, we explore the crystallographic and electronic structure evolution of these layers upon lithiation and delithiation. We fabricate Structure II stacks on 50 nm amorphous holey silicon nitride membranes (Figure 2.11a), and use scanning transmission electron microscopy (STEM) imaging to interrogate these devices in the pristine state before intercalation (Figure 2.11b) and after one cycle (Fig. 2.11c). As expected, data from the pristine heterostructure are fully consistent with that of H -MoS₂ (Fig. 2.11b). The onset of intercalation results in an increasingly disordered MoS₂ lattice evinced by the progressive splitting of the MoS₂ Bragg spots in the selected area electron diffraction (SAED) patterns. Importantly, even before the peak in R_{xx} we see this signature of disorder at the edges of the heterostructure, whilst the interior appears pristine. Full intercalation results in the observation of a ring in SAED (Figure 2.11c, inset). Insightfully, aberration-corrected imaging (Figure 2.9c) uncovers crystalline order within domains that are approximately 5–10 nm in size as indicated by fast Fourier transforms (FFT) of the atomic resolution images in specified regions (Figure 2.11c, right). Inverse FT permits us to resolve this 2D nanocrystalline domain structure. We also distinctly observe ~ 1 nm-sized defects in the metal dichalcogenide layer that are reminiscent of what has been reported in previous TEM studies of chem-

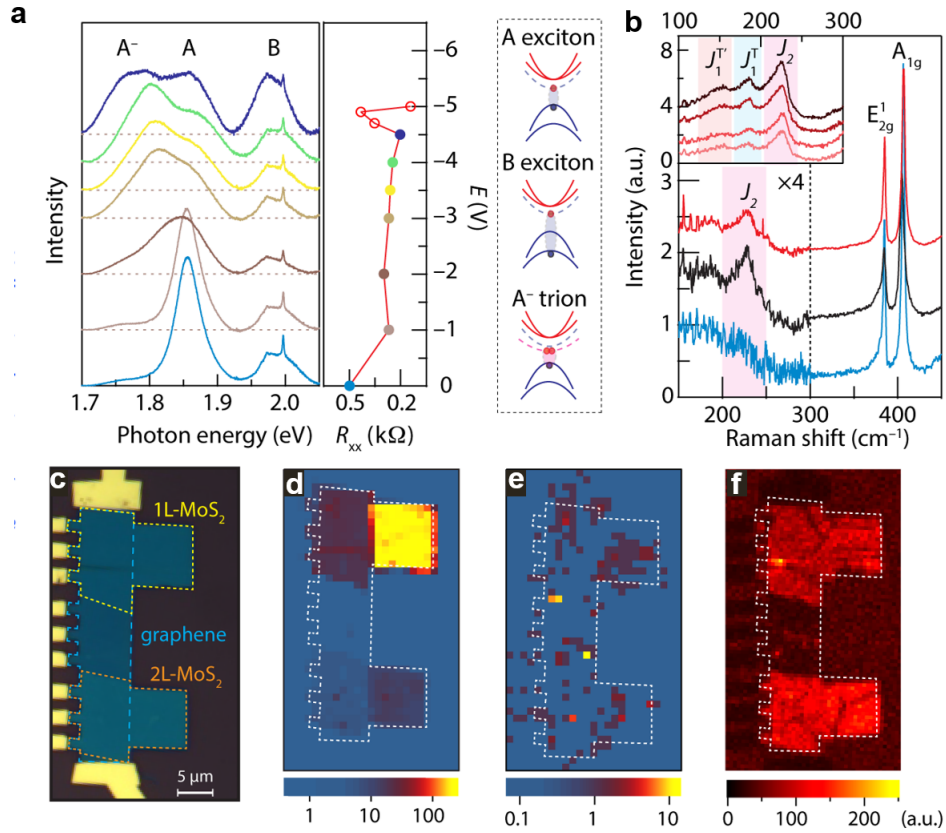


Figure 2.9: a, Operando photoluminescence (left) and resistance (middle) measurements acquired at a graphene-MoS₂ device over the course of a potential sweep at 325 K. The three pronounced spectral features are assigned to neutral excitons, A and B, due to the spin-split valence bands of the dichalcogenide, as well as the formation of negatively charged trions, A⁻. Spectral baselines are offset (dashed grey lines) to, and color-matched with their associated resistance-potential data points. b, Ex situ Raman spectra of a pristine device (bottom), after one cycle to -5 V and back to 0 V (middle), and after annealing for 1 h at 573 K (top). Inset shows Raman spectra after one intercalation-deintercalation cycle and annealing (573 K, 1 h) of hBN-encapsulated (from bottom to top) MoS₂, G/MoS₂, 2L-MoS₂, and G/2L-MoS₂. d, Optical micrograph of an hBN-encapsulated device consisting of a singular graphene monolayer straddling a monolayer MoS₂ flake on one end and a bilayer MoS₂ flake at the other as demarcated by the dashed lines. Scale bar: 5 μm. c-f, Ex situ photoluminescence (c,d) and Raman spatial maps of the device in d at room temperature before intercalation (d) after intercalation and deintercalation (e) and following annealing for 1 h at 573 K (f). The Raman map in f pertains to the 200–250 cm⁻¹ window and therefore represents the J₂ peak of T/T⁻-MoS₂.

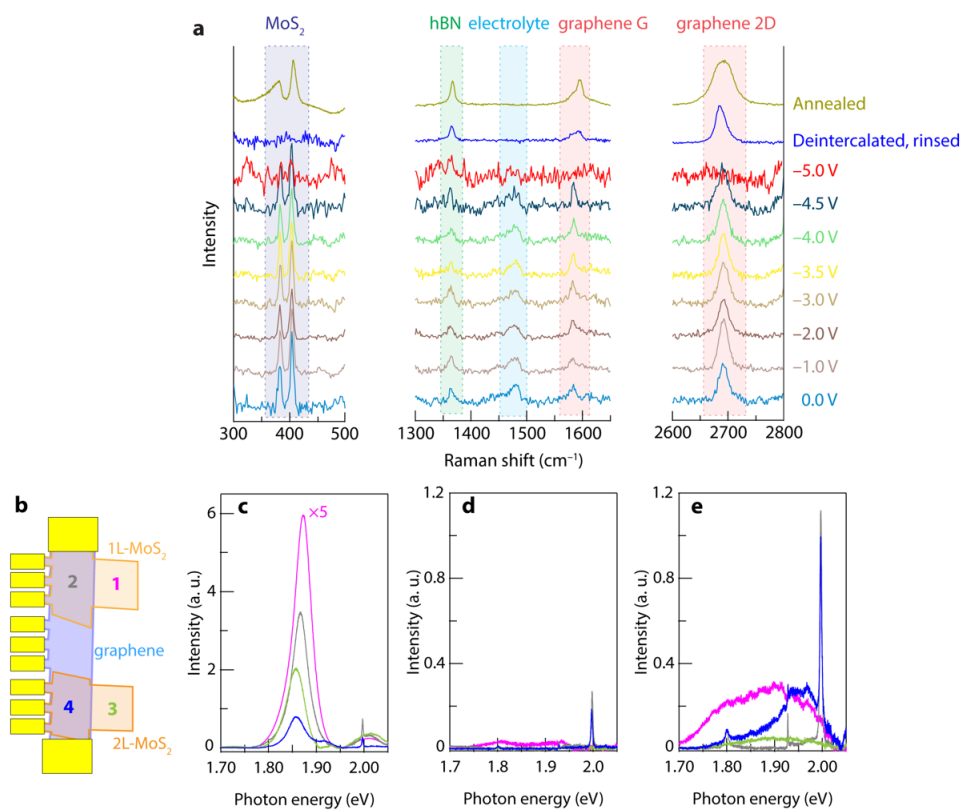


Figure 2.10: a, Raman spectra of an hBN-graphene-MoS₂ Structure II device over the course of electrochemical intercalation, showing the disappearance of graphene and MoS₂ spectral features after full intercalation at -5.0 V, consistent with Pauli blocking in addition to the 2H → 1T' phase transition of MoS₂. Deintercalation returns graphene peaks, and annealing at 300 °C for 1 h restores the 2H-MoS₂ peaks. Each spectrum is offset for clarity. b-g, Schematic diagram (b), photoluminescence spectra (c-e).

ically (*nBuLi*)-lithiated and exfoliated MoS₂³⁹. These defects were attributed to beam damage during imaging, which is a possibility for these studies as well owing to the long exposure times required before and during atomic resolution imaging. However, this structural disruption is perhaps more likely caused by the strain introduced into the MoS₂ layer during lithiation and the attendant progression of the H- to T' phase transformation along the lattice. This leads to pronounced wrinkles in bulk MoS₂ crystals³⁴, polycrystallinity in few-layer nanoflakes⁴⁵ of MoS₂, as well as visible cracks in the MoX₂ layer of our larger devices upon deintercalation. In our ex situ data of deintercalated structures we cannot observe the characteristic zig-zag superlattice structure of the T' phase even though we see clear evidence for this phase in Raman spectra (Figure 2.9b). Notably extended beam exposure is known to relax T'-MoS₂ to T-MoS₂³⁹, and additional studies involving lower beam energies as well as the development of an in situ electrochemical TEM methodology for these 2D stacks may be required to observe this phase in vdW heterostructures by electron microscopy imaging.

2.6 DENSITY FUNCTIONAL THEORY (DFT) COMPUTATIONS

The tuning of intercalation potentials using vdW heterostructures is well explained by the modification of theoretical Li binding energetics as observed in density functional theory (DFT) computations which were performed by our collaborators in the Kaxiras group (Fig. 2.12). First, these calculations reveal that the T-MoS₂ phase has a considerably stronger binding affinity for Li atoms than H-MoS₂. Thus a local phase transformation upon doping should lead to a cooperative effect wherein it becomes increasingly favorable to intercalate Li into that local vdW region as the dichalcogenide undergoes the semiconductor to metal H- to T'- transformation. Furthermore, since hBN is an inert, wide-gap insulator and non redox-active, the energetics of initial Li intercalation are only slightly perturbed in the case of hBN/T-MoS₂ compared to T'-MoS₂/T'-MoS₂. Contrarily, graphene (G) heterolayers have a substantially stronger attenuating effect on the binding energy of Li, yet still the reaction is

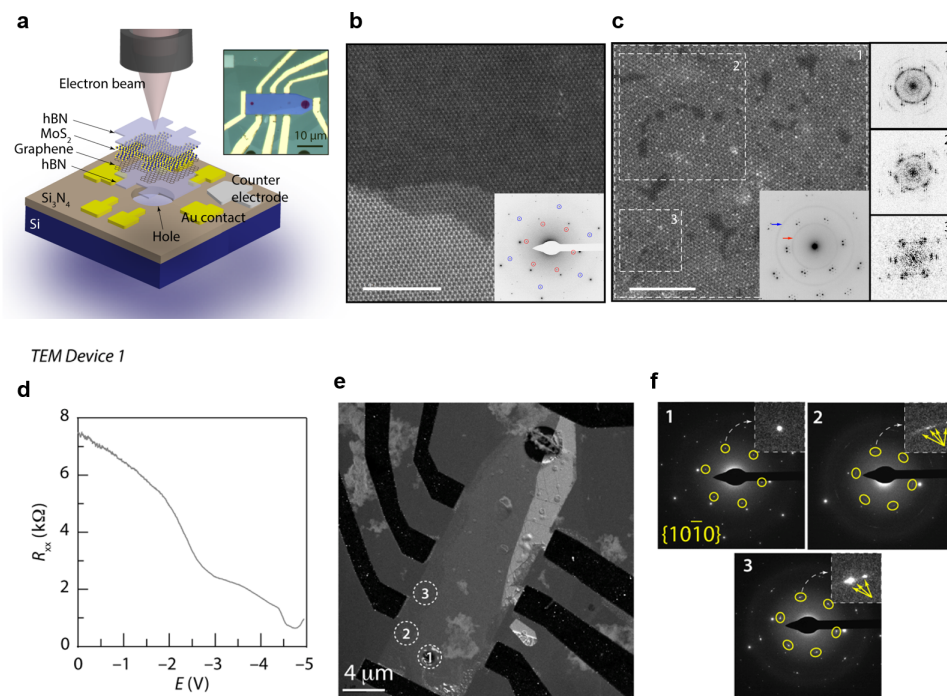


Figure 2.11: **a**, Schematic for vdW heterostructure device assembled onto amorphous holey silicon nitride membranes and subjected to one cycle of intercalation and deintercalation followed by (scanning) transmission electron microscopy, (S)TEM analysis. Inset shows optical microscope image of the one such device. Scale bar $10\ \mu\text{m}$. **b,c**, High angle annular dark field (HAADF) STEM images of Structure II devices before (**b**) intercalation and after one cycle (**d**). Scale bars: $5\ \text{nm}$. Insets show selective area electron diffraction (SAED) patterns using a $300\ \text{nm}$ sized aperture. Diffraction features originating from $10\bar{1}\bar{0}$ and $11\bar{2}\bar{0}$ planes of MoS_2 are marked with red and green circles/arrows, respectively. In **c**, fast Fourier transforms (FFT) obtained from the regions indicated with the dashed boxes are shown on the right, showing local crystallinity over $5\ \text{nm}$ domains. **d**, Resistance, R_{xx} , as a function of applied potential, E , of an hBN/ MoS_2 /G vdW heterostructure fabricated onto a $50\ \text{nm}$ holey amorphous silicon nitride membrane. The electrochemical reaction is suspended as the upturn in R_{xx} is commencing by immediately sweeping the potential back to $0\ \text{V}$. **e**, $g\text{-MoS}_2 = 1120$ dark field (DF) TEM image of the device after removal of the electrolyte. **f**, Selected area electron diffraction (SAED) patterns acquired from the regions designated 1, 2, and 3 in **b**. SAED data reveal a pristine MoS_2 structure in region 1, but splitting of the Bragg spots (insets) at the edges of the heterostructure (regions 2 and 3) are indicative of the formation of two or more domains.

more exergonic than that of Li with hBN/G or G/G⁴⁶ (Fig. 2.10a). As a result, we observe a positive shift in intercalation potential for G/ MoS_2 vs. hBN/G in Figs. 2.8a and c. Taken together, the results of all figures are consistent with the electrochemical reaction scheme that is presented in Figure

2.12c. This mechanism involves charge transfer to both graphene and MoX₂ in initial stages of the electrochemical gating process. Very dilute concentrations of Li⁺ ions are intercalated at modest potentials into MoX₂/hBN (and MoX₂/MoX₂) heterointerfaces. However, on the basis of SAED data of our heterostructures and prior observations of sluggish chemical lithiation of bulk MoS₂, Li⁺ ion intercalants of these interfaces appear most concentrated proximate to the heterostructure–electrolyte interface (where the electric field is certainly strongest and some T'-MoS₂ may be formed locally from electrostatic double-layer gating). The G/MoX₂ interface possesses a unique intercalation potential that is lower than that of G/hBN and as such, this is the next interface to undergo intercalation. Eventually a highly doped, 2D nanocrystalline T'-MoX₂ is formed upon complete intercalation of the graphene–dichalcogenide heterostructure.

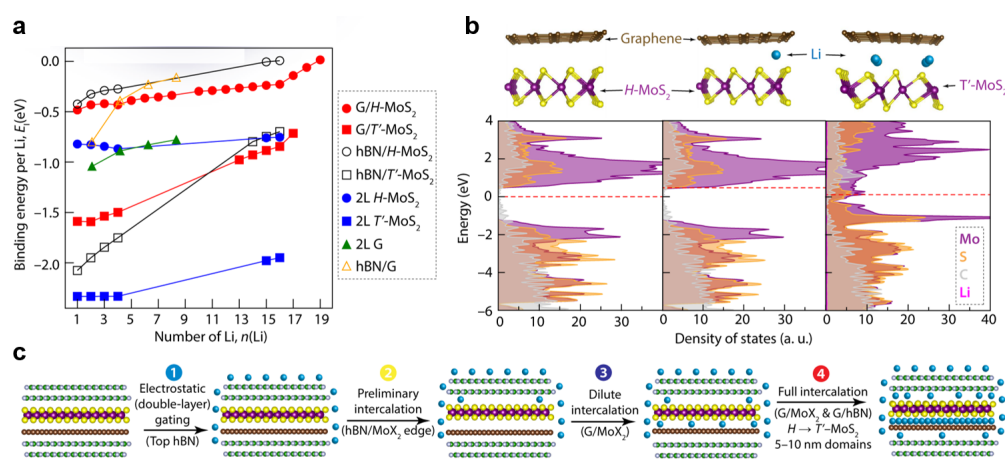


Figure 2.12: a, Computed lithium atom binding energy as a function of number of lithium atoms added to a supercell consisting of a layer of 4×4 unit cells of graphene and 5×5 unit cells of MoS₂. b, Computed top relaxed structures (top) and density of states, DOS, plots (bottom) for the pristine (left) and four-Li intercalated structure. 2L-graphene and hBN/G data are adapted from ref 33. c, Mechanism of vdW heterostructure intercalation based on experimental and computational data. [computation is performed by Daniel T. Larson in the Kaxiras group] [Reproduced from ref⁴⁷]

2.7 CONCLUSION

We note that typically, in battery electrodes consisting of layered material composites, carbonaceous additives like graphene serve primarily to improve cyclability, particularly over the course of additional conversion reactions that can form insulating and structurally expanded conversion phases^{25,26,48,49}. These approaches do not seek to create or exploit a direct vdW contact between individual atomic layers as a means of manipulating the intercalation reaction itself. Our observations for Li-ion intercalation at individual atomic interfaces motivate the use of vdW heterostructuring as a promising strategy in designing new intercalation materials by manipulating the ion storage modes and critical “job-sharing” characteristics of hybrid electrodes. In this regard, our results reveal that the low resistivity of graphene does not necessarily imply that it possesses the majority of electronic charge in the composite material. The vdW heterointerface hosts the Li⁺ ions, but it is the MoX₂ layer that is in fact the most highly electron-doped. Yet we conclude that the exceptional electronic mobility of graphene (sufficient to display quantum oscillations even after ion intercalation) furnishes a lower-resistance electronic pathway, notwithstanding a lower partial carrier density, which allows its immediate interface with the MoX₂ layer to undergo ionic doping more efficiently than adjacent MoX₂/MoX₂ homointerfaces. This decoupling of the electron from the ion in an electrochemical scheme is distinct from the case encountered in chemical lithiation reactions where the electron and ion donors are identical (e.g. organolithium reagents). Beyond battery technology, novel ion insertion and ion transport behavior in vdW heterostructures could enable increased control over selectivity in ion separations relevant to detoxification and desalination of water^{50,51}.

Furthermore, our demonstrated control over intercalation energetics, the resultant spatial carrier density profile, and realization of ultra-high charge densities using vdW heterointerfaces opens up new possibilities for 2D plasmonic device schemes⁵² that would require large variations in charge density. The *T'* metal dichalcogenide phases observed here are also especially interesting as potential precursors

of 2D topological insulators⁵³. To advance these areas, it may be important to devise approaches that mitigate the strain imposed on vdW layers upon association with intercalant species, since this can compromise the pristine crystallographic integrity of the atomically thin layers as we have observed.

3

Diffusion Study of Cations $[\text{AlCl}_4^-]$ into Few layer Graphene

3.1 INTRODUCTION

The rapid development of portable electronic devices, the promise of electric vehicles, and advances in the production of electricity from renewable sources have increased the demand for safe and low-cost

electrochemical energy storage devices^{54,55}. Although lithium-ion batteries (LIBs)⁵⁶ are widely used in portable consumer electronics and are rapidly entering into transportation and grid-scale storage sectors, the future of all types of Li-based batteries is the subject of much debate^{57,58}. The main limitations of LIBs include unresolved safety issues, slow charging, limited cycle lifetime, under-utilization, stress-induced material damage, capacity fade, and possibility of thermal runaway⁵⁷. In addition, lithium is a finite resource and its production faces geological, technical, and economic constraints with increased extraction costs projected for the future^{59,60}. These issues have prompted the pursuit of so-called “beyond Li-ion” batteries that use less lithium and/or use metals other than lithium^{55,59}.

Recently, rechargeable Al-based batteries utilizing AlCl_4^- ions have intrigued researchers as promising alternatives to LIBs. Three main factors make Al an attractive material for next-generation energy storage devices: First, because Al is the most abundant metal in the Earth’s crust and can be handled in air, materials extraction and device fabrication costs of Al ion-based batteries (AIBs) could, in principle, be low by comparison to those of LIBs. Second, the stability of Al to ambient conditions could lead to rechargeable batteries with significantly reduced concerns over safety. Third, owing to its relatively light weight and theoretical three-electron redox capability, AIBs could, in principle, not only offer a higher volumetric capacity (8046 Ah L^{-1}) than Li, Na, K, Mg, Ca, and Zn, but also a higher gravimetric capacity (2980 Ah Kg^{-1}) than Na, K, Mg, Ca, and Zn^{54,57,58,61}. In addition, compared to alkali-ion batteries, AIBs may deliver energy at a much more economically feasible rate (i.e. cost per kWh) because of the cost savings associated with the use of Al, leading to more rapid market penetration of this technology.

Notwithstanding the promise of AIBs, progress on rechargeable AIBs has failed to compete with that of other battery systems over the past three decades. Arguably the greatest contributors to the slow development of AIBs are: (i) the challenge of finding suitable cathode materials and electrolytes that are capable of operating near room temperature, and (ii) packaging problems and poor overall device stability due to corrosive electrolytes^{58,61}. Recent advances that include the use of ionic liquid

(IL) electrolytes have resulted in the extraordinary cycling performance of AIBs^{54,61,62,63,64,65,66,67,68}. In these systems, a metallic Al anode is combined with a graphitic cathode and a chloroaluminate IL (typically produced from a mixture of anhydrous AlCl_3 and a quaternary ammonium chloride salt like 1-ethyl-3-methylimidazolium chloride, EMICl) electrolyte, from which Al can be reversibly deposited and stripped with a high Coulombic efficiency ($>99.5\%$), without formation of dendrites and with a discharge voltage of about 2 V. One of the hallmarks of these chloroaluminate batteries is their impressively high charging rates, which have been attributed to very fast anion diffusion within the graphite cathode. However, unlike LIBs, the fundamental interfacial intercalation chemistry and ion transport dynamics within the cathode remain to be investigated in AIBs. One critical unknown is the intrinsic chloroaluminate ion diffusion rate in graphite, which would define the upper limit for the charging rate. Likewise, rationally tailoring cathodes that can offer higher discharge voltages requires measurements of electrochemical behavior at individual mesoscopic crystals of the intercalation host materials. Comparing such single-particle electrochemical analyses with more traditional ensemble battery cell measurements then enables the deconvolution of intrinsic physicochemical properties from the impact of additives and other extrinsic factors related to cell construction.

Here, I perform systematic investigations into the electrochemistry and diffusion dynamics of AlCl_4^- intercalation into graphite. We fabricate mesoscopic on-chip electrochemical cells with graphitic single crystals of controlled dimensionality—from few-layer graphene to bulk graphite flakes—and perform operando variable temperature charge transport measurements and optical microscopy. These measurements allow us to probe the intercalation reaction at the thinnest limit of the bulk intercalation compound (four-layer graphene) and to determine an upper bound for the diffusion coefficient of AlCl_4^- in graphite. Taken together, our studies provide fundamental insights into the chloroaluminate–graphite system and establish a methodological framework for the design and measurement of new candidate AIB materials with improved performance.

3.2 ELECTRO-INTERCALATION IN 2D LIMITS OF THE $\text{AlCl}_4^-/\text{GRAPHITE}$ SYSTEM

We began by exploring the electrochemical properties of the graphite- AlCl_4^- intercalation compound in the 2D limit with operando electronic transport measurements. We fabricated Hall bar devices containing few-layer graphene (2–6 layers) stacked between two 10–30 nm thick hexagonal boron nitride (hBN) crystals. The fabrication steps are demonstrated in figure 3.1.

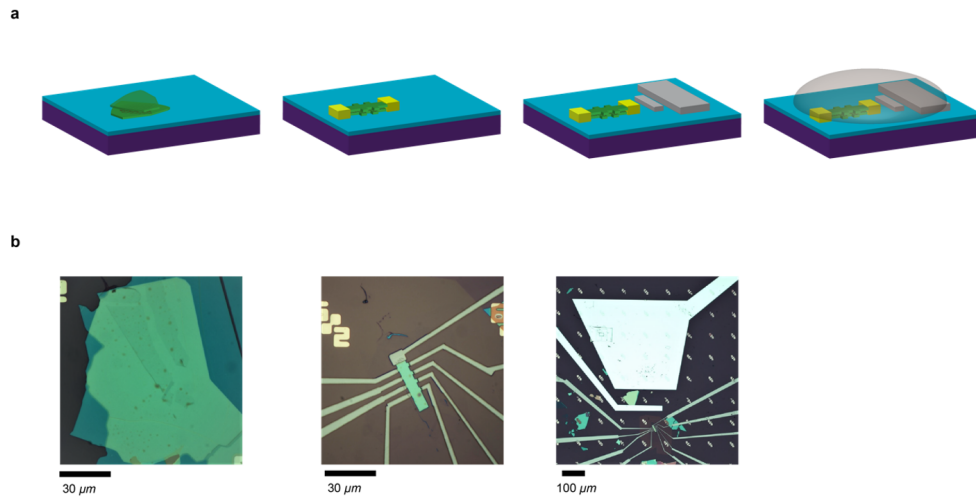


Figure 3.1: **a**, Schematic of fabrication steps to make microelectrochemical cell, showing a stack on a Si/SiO_2 substrate, formation of a Hall bar and deposition of an Au contacts, deposition of Ti/Al counter electrode(CE) and reference electrode (RE), and coverage of the device by an electrolyte droplet. **b** Optical micrographs of the fabrication steps depicted in (a).

We then constructed an on-chip electrochemical cell (Fig. 3.2a,b) consisting of this hBN/4LG/hBN Hall bar as the working electrode (WE), and two separate Al electrodes to serve as the counter electrode (CE), and pseudoreference electrode (RE). The WE, RE, and CE were then covered by a $\sim 10\mu\text{L}$ droplet of AlCl_4^- -EMI, which was prepared from a $\sim 3:2$ molar ratio of AlCl_3 and EMICl (see Appendix B). In addition to the electrochemical current response (I), standard AC transport measurements were used to measure the longitudinal resistance (R_{xx}) of the Hall bar WE at 300 K as the potential (E) at the WE was swept from 0 V to +2.0 V vs. the Al-RE with a sweep rate of 2 mV/s.

Beginning with a four-layer graphene (4LG) device, examining plots of both R_{xx} and I as a function of potential E (Fig. 3.2c) throughout the sweep provides insight into the fundamental steps in the intercalation reaction. The plot of R_{xx} shows two distinct regions: First, between 0 to 1.8 V, R_{xx} decreases only slightly, by less than 8 % compared to R_{xx} at 0 V. At 1.8 V, R_{xx} decreases precipitously after a small initial upturn and then remains unchanged from 1.85 V to 2.0 V. In the plot of I as a function of E , minimal change in I occurs until a significant increase at ~ 1.6 V, followed by the onset of a sharp increase in current at 1.8 V. To investigate the origin of these changes, we cooled these mesoscopic devices to 4 K under three applied biases (0 V, 1.55 V, and 2.0 V) and performed Hall effect measurements that allow us to precisely measure the carrier density in the graphene layers. At 0 V, the positive slope of the Hall resistance curve reveals electron doping of the pristine 4LG, and we calculate a 2D carrier density, n_{2D} , of $3 \times 10^{13} \text{cm}^{-2}$. At 1.55 V and 2.0 V, the slopes of the Hall resistance curves are positive (Fig 3.3), which is the manifestation of holes as charge carriers, and n_{2D} at 2.0 V is $4.4 \times 10^{14} \text{cm}^{-2}$. These changes in n are summarized in Fig. 3.2d.

Combined, these measurements provide key insight into the crucial steps in the intercalation of graphite by chloroaluminate ions and the ultimate capacity limits of the system. The initial decrease in R_{xx} , which is accompanied by a small change in I , yet switches the graphene from n-type to p-type conductor, is attributed to the purely electrostatic gating effect of the electrochemical double layer. As we have shown previously for Li+ intercalation, the initial upturn in R_{xx} at 1.8 V that coincides with an onset of a large increase in I arises because intercalation leads to decreased electronic mobility owing to increased scattering between electrons in the graphene layers and chloroaluminate anions in the van der Waals (vdW) gap^{27,47}. This decreased mobility causes the resistance to increase initially but is then overwhelmed by the greatly increased hole carrier density that also accompanies AlCl_4^- intercalation, resulting in a subsequent sharp drop in resistance. These charge transport measurements thus allow us to interrogate the intercalation mechanism directly, in a manner that is not conflated with side reactions as in the sole measurement of I . Our measurements also allow us to estimate an approximate

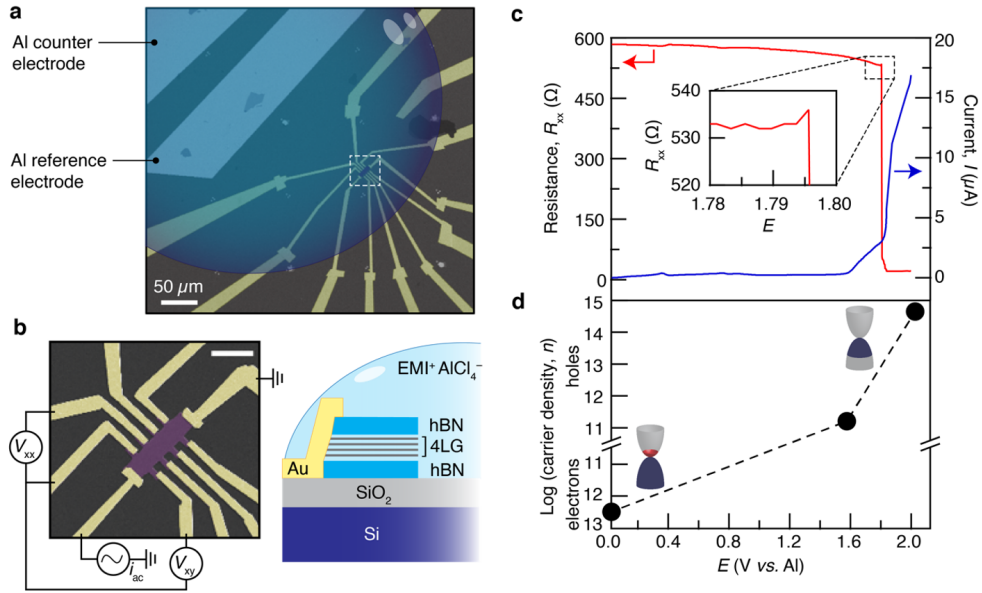


Figure 3.2: a, Optical micrograph of on-chip electrochemical cell for transport measurements during intercalation. b, False-color scanning electron micrograph of the region indicated with the dashed box in a showing hBN/4LG/hBN Hall bar working electrode, along with a cross-sectional schematic. Scale bar: 10 μm. c, Longitudinal resistance, R_{xx} , and electrochemical current response, I , as a function of potential, E vs. Al pseudoreference electrode. d Carrier densities extracted from Hall effect measurements as a function of E , showing transition from electron-doping to hole-doping.

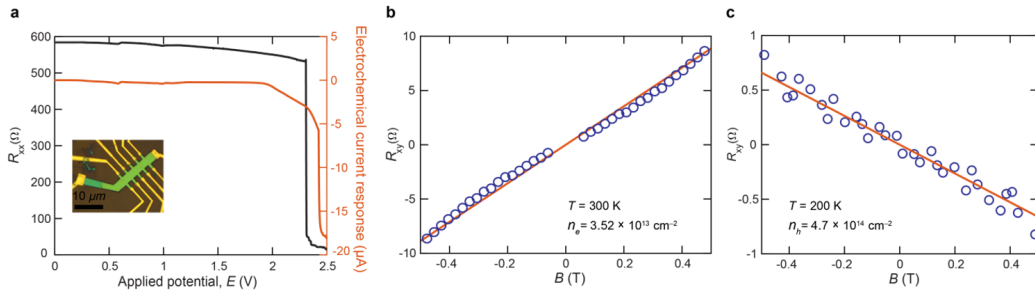


Figure 3.3: a, Plot of longitudinal resistance, R_{xx} , and electrochemical current vs applied potential with inset showing optical micrographs of devices. b,c, Transverse resistances, R_{xy} vs magnetic field, B , b before and c after polarization to 2.5 V, showing measured Hall carrier densities, n , which change from electron carriers (at 0 V) to hole carriers (2.5 V).

limit for the capacity of carbon-based chloroaluminate intercalation compounds; the Hall carrier density of fully intercalated 4LG devices, (Fig. 3.2d) translates into a capacity of $\sim 85 \text{ mAh g}^{-1}$. In this estimate, we consider only the three graphene–graphene vdW interfaces of the hBN/4LG/hBN heterostructure as active for intercalation (thus neglecting the two peripheral hBN/G vdW interfaces). This assumption is based on previous studies that showed >10 -fold decreased proclivity for hBN/G interfaces to intercalate Li^+ ions compared to that of G/G interfaces^{27,47}. Analogous experiments at 2LG achieved a carrier density of $1.0 \times 10^{12} \text{ cm}^{-2}$ at 2.5 V, which is more than two orders of magnitude lower than that observed for the aforementioned 4LG system. These results are consistent with only electrostatic gating, but no substantial intercalation in the 2L limit up to 2.5 V. The dissolution of contact electrodes prohibited potential excursions in excess of 2.5 V. It is noteworthy that the staging limits for chloroaluminate–graphite intercalation compounds are typically stage 4.

3.3 DYNAMIC OF ION DIFFUSION IN CONTINUUM LIMIT (RANDOM WALK)

While enhancing the ion accumulation is a dominant goal in energy storage research communities, fast charging/discharging, aging and working in harsh conditions limit use of the new materials as cathode/anode in storage energy unit. To address these problems, we need to understand the dynamics of ion diffusion inside the anode/cathode of the electrochemical cell. When ions start to intercalate between layers' host, they move very random and are constrained with boundary conditions. Previous studies show that ions movements inside the host has strong connections to a random walk problem. Diffusion and random walks are two processes which have similar mathematical descriptions in the continuous limit (steps in time and space are infinitesimally small)⁶⁹. Therefore, the results from one of these processes can be used to interpret or predict the results for the other.

Here, we consider the process of AlCl_4^- intercalation as a random walk in two dimensions. In high-density intercalation, the process can be considered linear with respect to time. Figure 3.4 illustrates

a path for an ion inside a host. We model movement of the ion from one spot to another by the probability function $c(x = k\Delta x, t = m\Delta t)$ which determines ion presence in a given position x at time t where k is a number of finite step in position and m is a number of finite step in time .

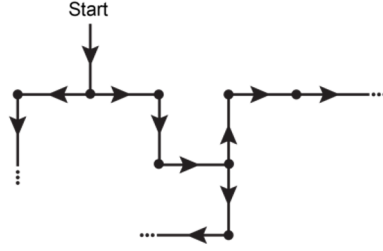


Figure 3.4: schematic diagram for 2D random walk path for an ion moving inside graphite

We combine the probabilities of being at that spot and moving to left or right. Equation 3.1 shows the probability of being ion in the spot based on a step time:

$$c[k\Delta x, (m + 1)\Delta t] = \frac{1}{2}c[k\Delta x, (m)\Delta t] + \frac{1}{4}c[(k - 1)\Delta x, (m)\Delta t] + \frac{1}{4}c[(k + 1)\Delta x, (m)\Delta t] \quad (3.1)$$

Initial conditions at $k = 0$ is : $c[0, 0] = 1, c[k\Delta x, 0] = 0, k \neq 0$ By using Taylor expansion and continuous limits, we define the next steps as following:

$$c[(k \pm 1)\Delta x, m\Delta t] = c[k\Delta x, (m)\Delta t] \pm \Delta x \frac{\partial c}{\partial x} + \frac{1}{2} \Delta x^2 \frac{\partial^2 c}{\partial x^2} \pm \frac{1}{6} \Delta x^3 \frac{\partial^3 c}{\partial x^3} + O(\Delta x^4) \quad (3.2)$$

$$c[k\Delta x, (m \pm 1)\Delta t] = c[k\Delta x, (m)\Delta t] \pm \Delta t \frac{\partial c}{\partial t} + O(\Delta t^2) \quad (3.3)$$

By substituting the equation 3.2,3.3 into 3.1, we have:

$$\begin{aligned}
c[x, t] + \Delta t \frac{\partial c}{\partial t} + O(\Delta t^2) &= \frac{1}{2}c[x, t] + \frac{1}{4}\{c[x, t] - \Delta x \frac{\partial c}{\partial x} + \frac{1}{2}\Delta x^2 \frac{\partial^2 c}{\partial x^2} - \frac{1}{6}\Delta x^3 \frac{\partial^3 c}{\partial x^3} + O(\Delta x^4)\} \\
&+ \frac{1}{4}\{c[x, t] + \Delta x \frac{\partial c}{\partial x} - \frac{1}{2}\Delta x^2 \frac{\partial^2 c}{\partial x^2} + \frac{1}{6}\Delta x^3 \frac{\partial^3 c}{\partial x^3} + O(\Delta x^4)\}
\end{aligned} \tag{3.4}$$

$$\Delta t \frac{\partial c}{\partial t} = \frac{1}{4}\Delta x^2 \frac{\partial^2 c}{\partial x^2} + O(\Delta t^2, \Delta x^4) \longrightarrow \frac{\partial c}{\partial t} = \frac{\Delta x^2}{4\Delta t} \frac{\partial^2 c}{\partial x^2} \tag{3.5}$$

$$D = \frac{\Delta x^2}{4\Delta t} \tag{3.6}$$

By neglecting higher order terms, we derive the diffusion constant D .

This is the simple model, one can estimate the ion diffusion constant by observing intercalation area (change (Δx^2) as function of time (Δt)).

3.4 CHLOROALUMINATE AlCl_4^- ION DIFFUSION VIA OPTICAL MICROSCOPY

To estimate the diffusion coefficient of AlCl_4^- ions in graphite-based electrodes, we assembled a two-electrode on-chip electrochemical cell under an optical microscope (Fig. 3.5). We observed reversible intercalation in an ~ 80 nm thick graphite crystal, manifested by changes in the optical contrast across the flake, which occurs due to a combination of interlayer expansion and changes in dielectric constant due to intercalation-induced doping^{70,34,7}. As anticipated by the transport measurements shown in Fig. 3.2, no contrast change occurs when the applied potential between the graphite and counter electrode is less than 1.85 V. As the bias is increased beyond 1.9 V, we see evidence of AlCl_4^- ions intercalating into, and diffusing through the graphite lattice with a well-defined staging behavior. These optical changes are reversed when the potential returns to 1.5 V, however the flake is left with some

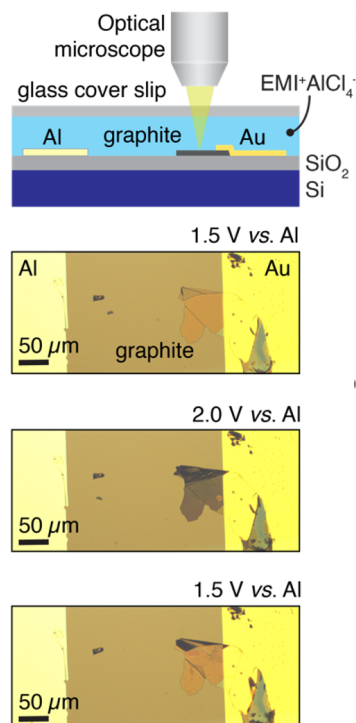


Figure 3.5: Top: Schematic showing on-chip spectroelectrochemical cell for intercalation and simultaneous optical measurements of graphite flakes. Bottom: Optical micrographs of an 80 nm graphite flake with $E = 1.5$ V (before intercalation), 2.0 V (intercalation commenced), and 1.5 V (after deintercalation) at 300 K.

additional wrinkles from this intercalation–deintercalation cycle. Fig. 2b shows a series of optical microscope images taken over a period of 2 s as under a bias of 1.9 V. These images clearly display the movement of the diffusion front with time, and the intercalated area was extracted from the image at each time point (fig 3.6), allowing estimation of the diffusion coefficient, D , for AlCl_4^- in graphite by linear regression analysis of the temporal evolution of intercalated area (Fig. 3.6 c) using a simplified continuum model. In this model, the D is related to the change in area ΔA and time as shown in Eq 3.6. The resultant D based on equation 3.7 we extract from the room temperature measurements of Figs. 3.6 b,c is $\sim 1.1 \times 10^{-6} \text{ cm}^2 \text{ s}^{-1}$.

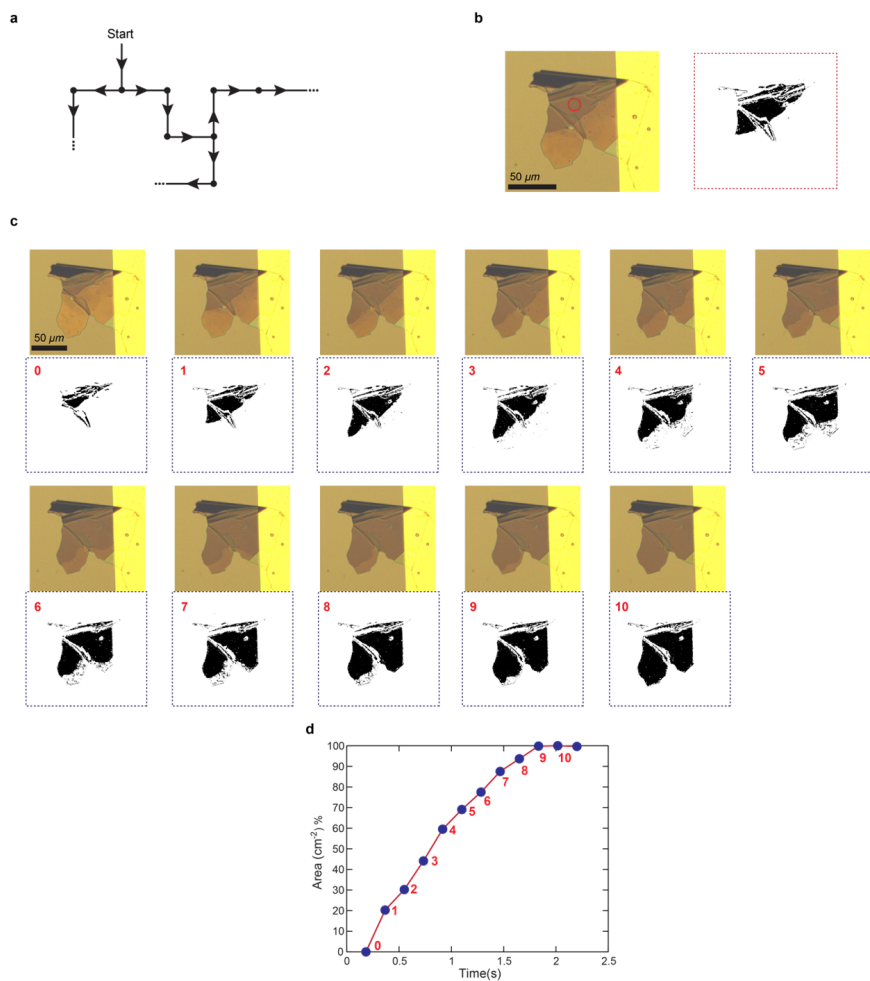


Figure 3.6: a 2D random walk path for an ion moving inside graphite. b Optical micrograph of graphite flake with Au contact, with accompanying binary images created by MATLAB's Image Thresholding toolbox. c Optical micrographs and corresponding binary images of graphite flake as CE potential is held at 1.9 V at 300K, showing how the ions diffuse to cover the flake. d Plot of ion coverage area vs. time determined from images in (c).

3.5 AlCl_4^- DIFFUSION STUDY INTO DISK SHAPE ELECTRODE

Previous studies have shown that a disk geometry is useful in studying diffusion through a material, as it creates boundary conditions equal at all edges and directions. Devices for diffusion characterization were fabricated by patterning disk shapes onto graphite flakes using electron-beam lithography followed by reactive-ion etching. Al contacts and a Al counter electrode were deposited by electron beam evaporation. Variable-temperature diffusion experiments were performed in an argon-filled glovebox. First, a 20 μL droplet of electrolyte was deposited onto the device, which was kept in a temperature-controlled sample holder.

Ion intercalation was performed by applying a potential between the CE and graphite electrode. An optical microscope equipped with a high-resolution camera was used to record videos of the intercalation process at different temperatures between 320 and 220 K. After collecting videos of intercalation at desired voltages and temperatures, we processed images of the graphite electrodes throughout the intercalation process using MATLAB's Image Thresholding toolbox to create RGB masks to extract binary image based on desired color. Video frames were analyzed to extract the ion coverage area of the electrode. A complete visualization of this technique is presented in Figures 3.8 and 3.9, with additional details of our diffusion calculations below. Diffusion coefficients are calculated when the ion coverage area varies linearly with time, which occurs in the range of 20–70% coverage (Fig 3.8).

These ion dynamics were then probed over a wide temperature range of 320–220 K by fabricating disk-shaped graphite electrodes with thicknesses of 40–50 nm. We note that with decreasing temperature, higher potentials were required to initiate intercalation as monitored by optical contrast, which may be attributed to changes in equilibrium potential and/or changes to ohmic losses through the electrolyte in this two-electrode configuration. Regardless, D can be determined for each condition as summarized in Fig. 3.9d. At 320 K, we extract $D = 9.6 \times 10^{-6} \text{ cm}^2 \text{ s}^{-1}$, a value approaching the diffusion coefficient of chloride ions in water at room temperature (ca. $2 \times 10^{-5} \text{ cm}^2 \text{ s}^{-1}$)⁷¹. Since

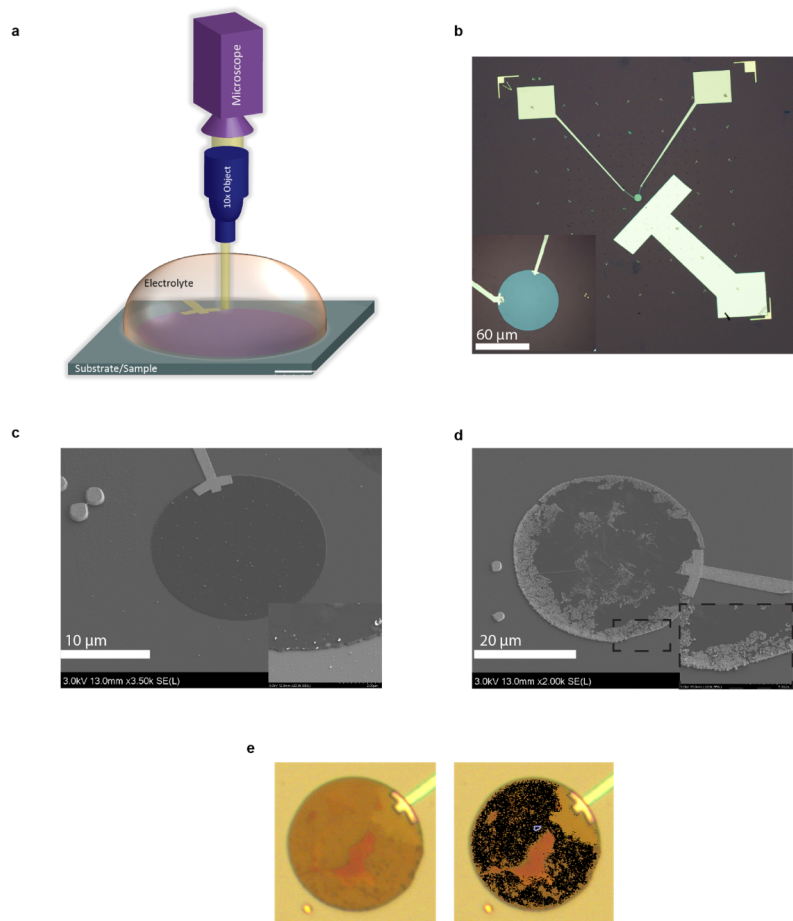


Figure 3.7: **a**, Schematic of space- and time-resolved microscopy for studying AlCl_4^- intercalation into graphite disk. **b**, Optical micrograph of device containing 40nm-thick graphite disk. **c** SEM image of graphite disk before intercalation, with inset showing disk edge. **d** SEM image of graphite disk after intercalation, with inset showing the disk edge where wrinkles have appeared on the disk. **e** Optical micrographs of on-chip graphite disk, showing creation of a binary image in MATLAB's Image Thresholding toolbox.

practical cathodes consist of polycrystalline materials and also contain additives and binders, the values for D we obtain serve as upper bounds for chloroaluminate ion diffusion in graphitic cathodes. Employing this diffusion constant, we can also evaluate the performance of AIBs constructed with cathodes of varying composition and microstructure.

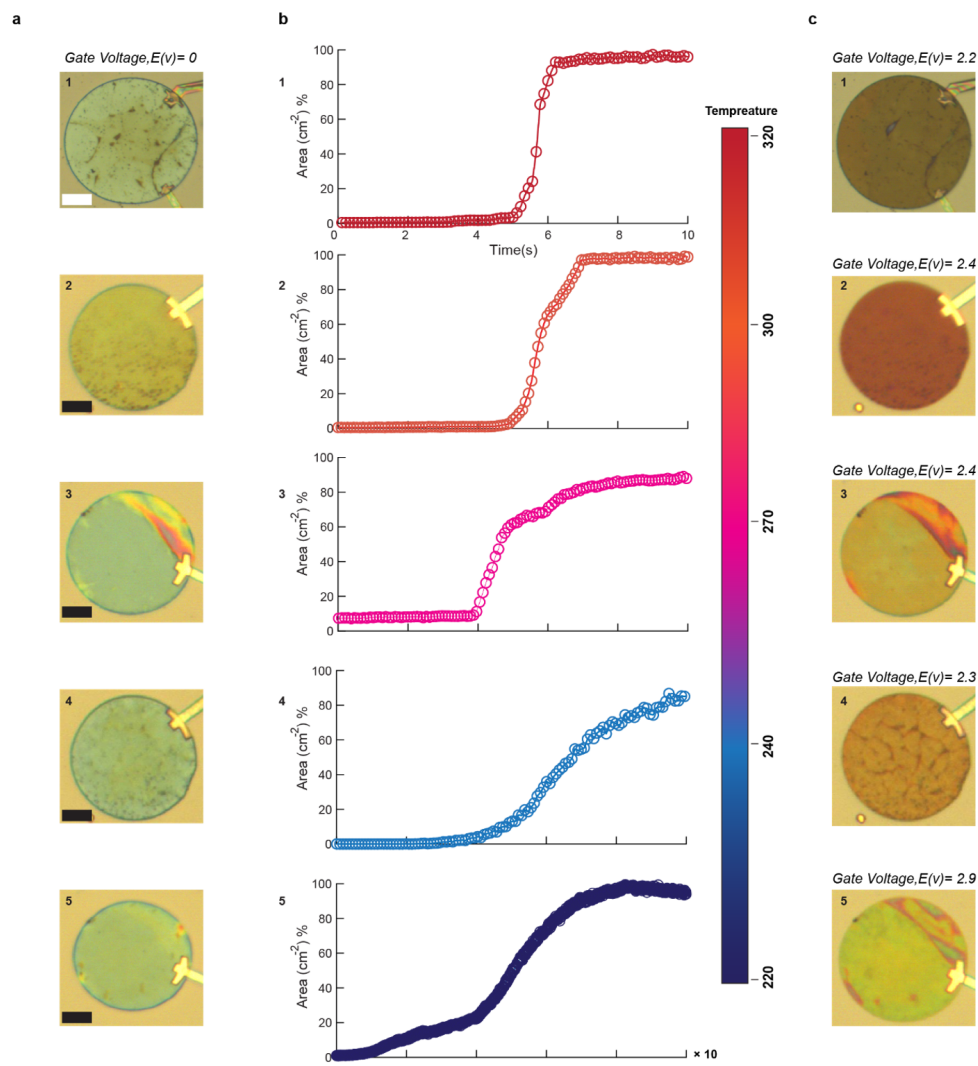


Figure 3.8: a, (1-5) Graphite disk images before intercalation at 0 V. Scale bars = 15 μm (1), 10 μm (2-5). b, (1-5), Ion coverage area for each disk vs. time at different temperatures and fixed potential, labeled in (c). x-axis is multiplied by 10 in (5). c, (1-5), Optical micrographs of intercalated disks at corresponding temperatures and the fixed voltage.

3.6 CONCLUSION

Understanding the underlying electrochemical processes in battery materials is essential to improving battery performance. Charge transport measurements were performed to gain insight into the elec-

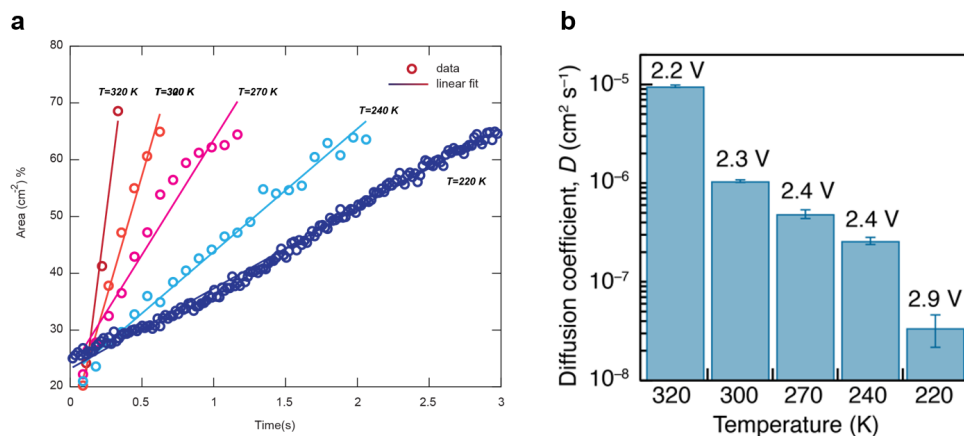


Figure 3.9: a, Plot of intercalation area as a function of time used to estimate chloroaluminate ion diffusion constant. Data are shown for linear regions of coverage area increase, between 20–70% coverage. b, Chloroaluminate diffusion coefficients measured at different temperatures, also showing the potential at which the optical analysis was performed.

trochemistry of AlCl_4^- intercalation into few-layer graphene and thick graphite flakes. These measurements uncovered the intercalation behavior of the 2D limit of the chloroaluminate–graphite intercalation compound and allowed estimations of the limiting capacity that might be expected from AIBs comprising graphitic cathodes. Transport of AlCl_4^- within thin graphite crystals was revealed by optical microscopy, leading to a quantitative determination of the chloroaluminate diffusion coefficient as $9.6 \times 10^{-6} \text{ cm}^2 \text{ s}^{-1}$ at 320 K and $3.4 \times 10^{-8} \text{ cm}^2 \text{ s}^{-1}$ at 220 K. Our results thus establish that controlling the nanoscale morphology of graphitic anodes will be especially important to optimizing the performance of AIBs. These studies also provide a mesoscopic device framework for probing the fundamental physicochemical phenomena underlying the operation of practical battery devices and exemplify how to make connections between these approaches and more conventional electrochemical measurements.

4

Electron Transport in Organic and Semi Organic layered materials

4.1 INTRODUCTION

In this chapter, we discuss electrical transport in organic molecule based low dimensional materials ; MOFs and graphullerene . The growth details and other characterization techniques of these molec-

ular crystals are described in these works⁷²⁻⁷³. MOFs and organic materials are very sensitive to heat and electron beam (e-beam) for device fabrication. In order to overcome these challenges, we introduce a device fabrication method that is the solvent and e-beam free lithography process and can be performed inside inert environment such Argon or nitrogen filled glovebox. This advanced high resolution stencil mask technique brings us the possibility of having high quality devices which are reliable to explore the intrinsic properties of new sensitive materials.

4.2 AIR & SOLVENT FREE DEVICE FABRICATION

A high-resolution stencil mask technique was used to fabricate rigorously air-free devices inside the glovebox. This process is free of solvents and polymers and helps to preserve the quality of the crystals, eliminating possible artifacts that might arise from conventional lithography processes using solvent-based methods and conducting paints usually applied as contacts for bulk crystals. The process starts with the fabrication of the stencil masks. The mask is based on a Si/Si₃N₄ (500 nm) substrate. Multiple windows of 200µm×200µm squares are patterned by photolithography. For the largest patterns, 500µm×500µm squares were used. Stencil masks were fabricated from Si₃N₄(500 nm)/Si(300 µm)/Si₃N₄(500 nm) wafers. At first, a combination of photolithography, reactive ion etching, and wet etching (potassium hydroxide solution) was used to create 200 and 500 µm square windows of Si₃N₄. The silicon was etched to make a silicon nitride window. Subsequently, the desired patterns of devices were written with photolithography on the windows. Then, the silicon nitride was etched with a reactive ion etcher to finish the mask fabrication.

We used a micro-positioner to align and place the prefabricated Si₃N₄ masks on transferred flakes. To place the mask on the substrate, we applied a small amount of grease (Apiezon H) near the edge of the mask. Then the mask was placed on a desired position using a micropositioner. It is important to press the mask well to minimize the gap between the mask and the crystal. If the gap is too large, it

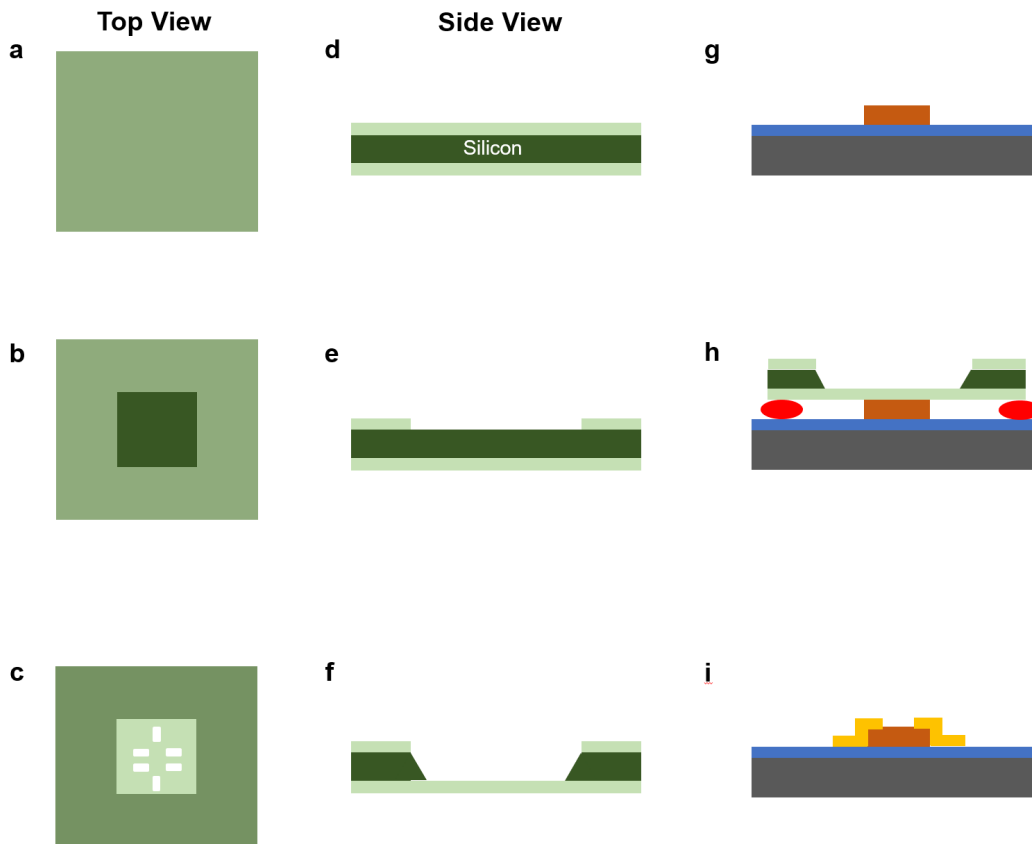


Figure 4.1: a-c, Double sided Silicon nitride substrate used to fabricate window and final contacts pattern via photolithography and dry/wet etching. d-f, side view of steps from a to c. g exfoliated flake on top of designated substrate. h, aligning the patterned window to the flake with micropositioner. We use a small amount of grease to attach the silicon nitride window to the substrate. i, depositing metal as contacts and removing the mask.

will generate deposition shadows around the pattern that could short the device. Once the mask was well-positioned, we finished the device fabrication by evaporating metal. Gold and palladium electrical contacts were tested, and the palladium electrode seems to provide a better electrical connection. The final device was isolated, mounted on a 16 pins chip-carrier, and wire-bonded inside the glovebox. Finally, the chip-carrier was covered with glass and loaded into the cryostat for the measurements.

4.3 ELECTRICAL TRANSPORT SINGLE CRYSTALS OF 2D MOFs $\text{Ni}_3(\text{HITP})_2$

MOFs are hybrid inorganic/organic crystals that can possess features distinct from many crystalline materials^{74,75}: intrinsic porosity, nm-scale lattice parameters, flexible mechanics, and a rich structural and compositional diversity enabled by advances in both organic and inorganic chemistry in three dimensions. The vast majority of MOFs are insulators and have been used in applications that benefit from high surface areas and chemical tunability, such as gas capture and catalysis. Conductive MOFs represent a new type of hybrid inorganic/organic conductor in addition to non-porous coordination polymers and hybrid perovskites, which have recently demonstrated high conductivities and superconductivity⁷⁶ and promising performances for optoelectronics⁷⁷, respectively. 2D layered MOFs where metals and redox-active ligands form extended π -d conjugated sheets (Fig. 1.5), have shown the highest conductivities and are predicted to exhibit rare transport phenomena including, for instance, the quantum anomalous Hall effect⁷⁸. However, due to poor synthetic control and small crystallite size, charge transport and structural studies for the 2D MOFs have generally relied on polycrystalline films/pellets and powder X-ray diffraction (PXRD), where grain boundaries and anisotropy obscure the intrinsic properties. Only a handful of single crystal devices have been reported including a room-temperature conductivity value for a 2D MOF⁷⁹, for a 2D coordination polymer,⁸⁰ and for some less-conductive 3D MOFs^{81,82}. Despite $\text{Ni}_3(2,3,6,7,10,11\text{-hexaiminotriphenylene})_2$ ($\text{Ni}_3(\text{HITP})_2$) possessing one of the highest conductivities for a porous MOF and having demonstrated promise for various applications, its conduction is poorly understood; calculations have predicted $\text{Ni}_3(\text{HITP})_2$ to be metallic but results of experiments on polycrystalline pellets down to 80 K have been interpreted as semiconducting⁸³. Here, with isolated crystals, we reveal the distinct layer stacking for $\text{Ni}_3(\text{HITP})_2$, the metallic nature of single crystals of $\text{Ni}_3(\text{HITP})_2$, and the importance of transport in the out-of-plane direction despite the presumed dominance of in-plane transport for 2D MOFs. The details of transport analysis for $\text{Cu}_3(2,3,6,7,10,11\text{-hexahydroxytriphenylene})_2$ ($\text{Cu}_3(\text{HHTP})_2$) has been this in

our paper⁷³. Here, we focus on electrical transport for $\text{Ni}_3(\text{HITP})_2$.

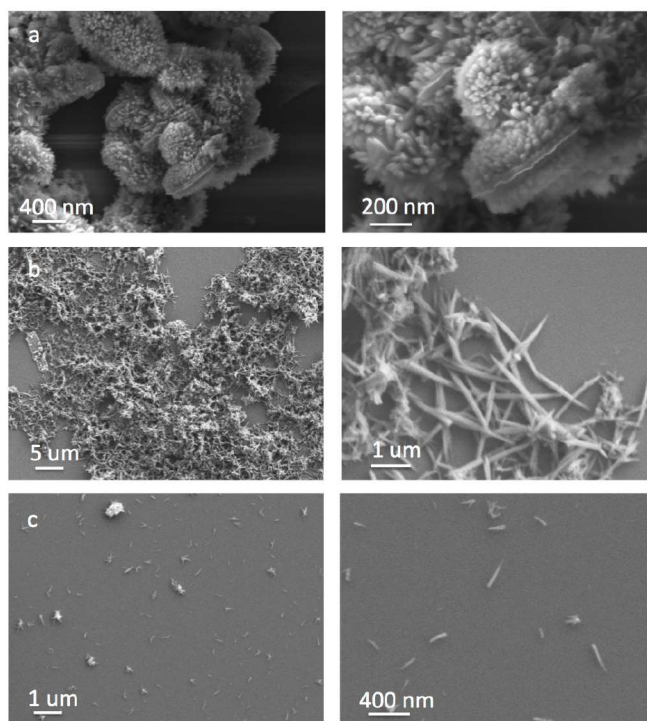


Figure 4.2: a, using new conditions with NiCl_2 and sodium acetate in an open vial b, and using a 10X higher concentration of sodium acetate with nickel nitrate in a closed vial.c, The use of NH_4OH generally yielded $\text{Ni}_3(\text{HITP})_2$ morphologies that were difficult to isolate individual crystals from as the crystals appear to emanate from a shared base. The use of sodium acetate led to isolated rods in appreciably higher yields and were used for TEM and device fabrication.

To understand charge transport in our 2D MOFs, we isolated individual crystals of $\text{Ni}_3(\text{HITP})_2$, and measured their conductivity as a function of temperature. Fig 2 published in ref¹³ generated an interconnected nanocrystalline morphology (Figure 4.2), which has been challenging to isolate crystals from. Here, we obtain isolated rods of $\text{Ni}_3(\text{HITP})_2$ up to $\sim 2 \mu\text{m}$ in length and $\sim 200 \text{ nm}$ in diameter. Devices were fabricated by drop-casting suspensions of $\text{Ni}_3(\text{HITP})_2$ rods onto Si covered by SiO_2 substrates and using electron-beam lithography and metal evaporation to deposit Ti/Pd contacts on top of the rods (Fig. 4.3a). A DC current-voltage (I-V) sweep for a representative device (Fig. 4.5b) yielded four-probe conductance values G of 1.3 mS at 295 K and 0.7 mS at 1.4 K, and

two-probe values of 0.25 mS at 295 K and 0.13 mS at 1.4 K. A reversible decrease in conductance is observed when a magnetic field is applied (Fig. 4.3b, inset), and the magnitude of this change decreases as the temperature T increases from 1.4 K (top) to 10 K (bottom). Such low temperature enhanced increased magnetoresistance suggest positive magneto resistance originated from the shrinking of electronic impurity wave function under a magnetic field. However, potential mixing between Hall and longitudinal resistance in our device geometry requires proper multiterminal magnetotransport in the future study.

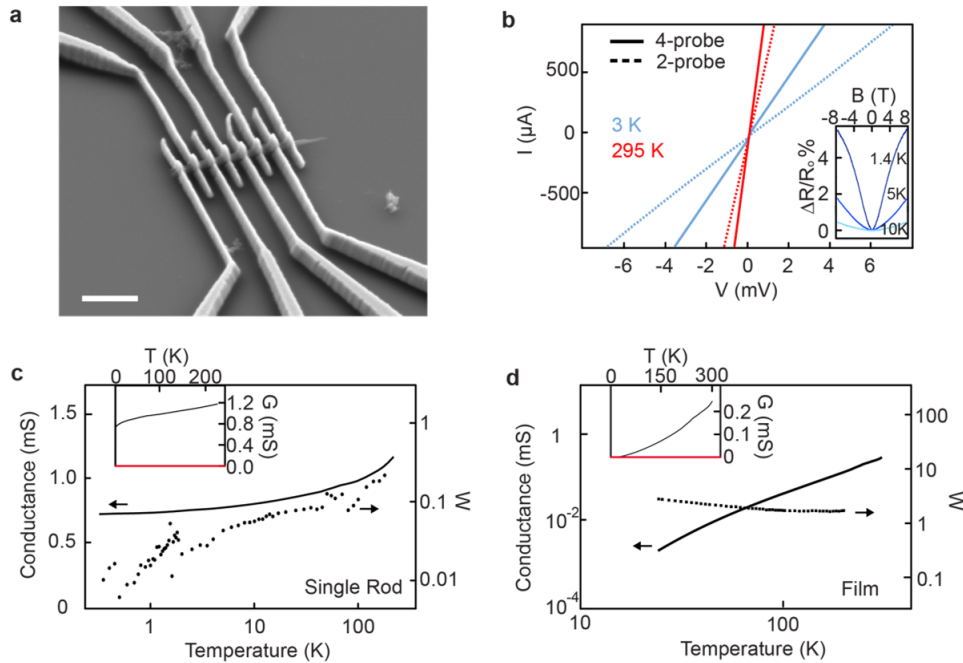


Figure 4.3: **a**, SEM of a single rod $\text{Ni}_3(\text{HITP})_2$ device with Ti/Pd contacts. Scale bar, 1 μm . **b**, Current–voltage plots of a single rod $\text{Ni}_3(\text{HITP})_2$ device at 295 K (blue) and 1.4 K (black). Inset: Normalized magnetoresistance at several fixed temperatures. **c,d** 4-probe temperature-dependent conductance (solid line; left axis) of a single rod device (c) and a polycrystalline film device (d) of $\text{Ni}_3(\text{HITP})_2$ and their corresponding Zhabrodskii plots with their reduced activation energy (dotted lines; right axes). Inset: Temperature-dependent conductance plotted with linear axes.

We find that further decreasing the temperature from 1.4 K to 0.3 K (Fig. 4.3c); red solid line, left axis) decreased the four-probe conductance negligibly. Variable temperature (VT) measurements on

three additional $\text{Ni}_3(\text{HITP})_2$ rod devices showed a similar weak, positive dependence on temperature. In contrast, a four-probe VT measurement of a polycrystalline $\text{Ni}_3(\text{HITP})_2$ film device (Fig. 4.3d; black solid line, left axis) revealed a conductance that decreased by orders of magnitude over a smaller temperature range.

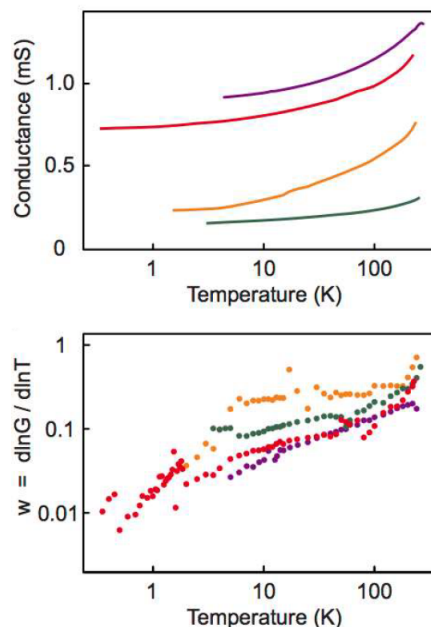


Figure 4.4: Top, Temperature dependent conductance traces for four $\text{Ni}_3(\text{HITP})_2$ devices. Bottom, Zabrodskii plot showing reduced activation energy (w) as a function of temperature for the four traces.

To understand the VT behavior for these single rod and polycrystalline devices, we plot the activation energy $W(T) = d \ln G / d \ln T$ vs temperature T in a logarithmic scale as shown in Fig. 4.3c and Fig. 4.3d (dashed lines, right axes). This Zabrodskii plot scheme has been used for doped organic polymers⁸⁴, quantum dot films⁸⁵, and other systems⁸⁶, where the negative slope of the Zabrodskii plot indicates localization behaviors with a reduced activation gap. We observe a positive slope for all single rod devices, indicating metallicity in the absence of the strong localization at low temperatures. A small reduced activation energy value that decreases as temperature decreases is consistent with a

non-zero conductance value as temperature goes to 0 K (Fig. 4.3c inset). For the polycrystalline film device, we observe a negative slope in the Zhabrodskii plot, indicating a semiconducting nature, where the conductance approaches 0 as temperature goes to 0 K (Fig. 4.3d inset). Literature precedence^{86,87} and additional data (Fig 4.4) are consistent with our interpretation of metallicity in $\text{Ni}_3(\text{HITP})_2$.

With the aid of single crystal device data, we make observations relevant to understanding transport in conductive 2D MOFs. First, $\text{Ni}_3(\text{HITP})_2$ system, rod devices with significant out-of-plane contributions show conductivities greater than their polycrystalline pellet measurements. The out-of-plane transport is often disregarded in the literature compared to in-plane transport, but is consistent with band structure and density of states calculations, which show that C, N, and Ni contribute to these out-of-plane bands. Second, Zhabrodskii plots show a positive slope for single crystal $\text{Ni}_3(\text{HITP})_2$ devices but a negative slope for its polycrystalline film, indicating intrinsic metallic conducting nature of single crystal MOFs, while the non-metallic behavior of polycrystalline film could be extrinsic to the materials. Additional work is needed to further understand the role that anisotropy and grain boundaries contribute to polycrystalline transport. Importantly, for organic systems and quantum dot films, by controlling film preparation and the material's surface, conductance can be increased by orders of magnitude; similar strategies may yield significant increases in polycrystalline MOF transport. Last, we note that literature reports have attempted to claim metallicity or a semiconducting nature for various MOFs or coordination polymers by analyzing high temperature polycrystalline pellets or by applying Arrhenius equations to weak temperature dependences, which may lead to incorrect interpretations of small band gaps. We show that although the out-of-plane conduction for $\text{Ni}_3(\text{HITP})_2$ devices decreases with temperature, the Zhabrodskii analysis at low temperatures and single crystals are critical in determining the nature of its conduction.

4.4 HALL EFFECT MEASUREMENT IN SINGLE CRYSTALS OF 2D MOFs $\text{Ni}_3(\text{HHTP})_2$

A major bottleneck towards exploring MOFs properties has been crystal growth, especially within the basal plane where high conductivity and topologically nontrivial properties are expected. Indeed, even basic experiments such as a Hall effect measurement of the basal plane have not been possible because the basal plane domain size afforded by conventional crystal growth techniques has thus far been limited to less than 200 nm, which is under the spatial resolution limit for multi-terminal device fabrication using lithography techniques^{88,79,89,14,13}. As such, one of the key challenges preventing a deeper understanding of the electronic properties of these materials has been the growth of sufficiently large single crystals. Our collaborator at MIT developed a biophase method to grow large single crystal of 2D MOFs⁷². Basically the reaction is confined in liquid liquid interfaces. The summary of growth shows in Fig 4.5. In this work, we demonstrate the growth of single crystals of Ni-CAT-1 ($\text{Ni}_3(\text{HHTP})_2$; HHTP = 2,3,6,7,10,11-hexahydroxytriphenylene). This material is chosen as the testbed for a new growth technique for 2D π MOFs that promotes the growth of plate-shaped rather than needle-shaped single crystals.

Optical microscope and scanning electron microscope (SEM) images of large single-crystal plates of Ni-CAT-1 grown by the method described above are shown in Fig. 4.6. The morphology of these crystals strongly contrasts with previously reported Ni-CAT-1 needle-shaped crystals. The lateral dimension of the solution-solid grown crystals is more than two orders of magnitude larger than the needle-shaped ones.

The large single crystals of Ni-CAT-1 permit measurements of electrical properties of the basal plane in 2D π MOFs. To minimize damage to the 2D π MOFs during device fabrication, we placed four electrical contacts using a stencil mask technique rather than conventional electron beam lithography (Fig 4.7). The stencil mask avoids electron beam resist coating, baking, and direct electron-beam exposure. Details of the sample fabrication techniques and conductivities are given in Fig. 4.8. Con-

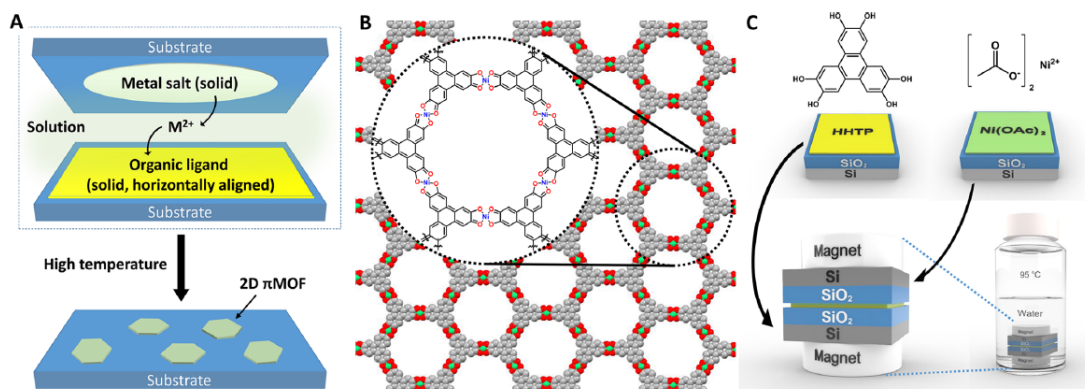


Figure 4.5: (A) Schematic illustration of the solution-solid growth of 2D π MOFs. The organic ligands are introduced in the solid phase and react with metal ions that are dissolved in water. The dense and aligned organic molecules increase the basal-plane growth rate. The high reaction temperature accelerates the reaction rate and ensures high crystallinity. The small volume and high aspect ratio of the reaction solution facilitate planar crystal growth. (B) MOF layer structure of Ni-CAT-1. (C) Schematic of the growth method. HHTP film is grown by vacuum thermal evaporation, and $\text{Ni}(\text{OAc})_2$ is drop-cast on a separate substrate. The two substrates are pressed together so that the two reactants are opposite each other. Teflon-coated magnets are used to press the two substrates with a pressure of 50 kPa at room temperature. The ensemble is placed in water and heated at 95 °C. Typical growth conditions are from 40 nm-thick film of HHTP, a drop-cast film of $\text{Ni}(\text{OAc})_2$ from 20 μL of 10 mM methanol solution, and a reaction time of 12 h.

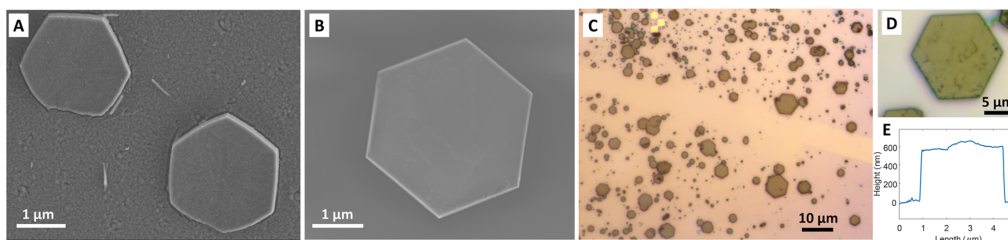


Figure 4.6: (A) SEM image of Ni-CAT-1 crystals after a reaction time of 1 h. (B) SEM image of crystals grown after 12 h. No residual HHTP is observed surrounding the Ni-CAT-1 crystals, and the sharp edges and corners indicate increased crystallinity. (C,D) Optical microscope images of the crystal plates on a Si/SiO_2 substrate. (E) Thickness profile of the crystal grown from 40 nm of HHTP. The thickness can be varied by adjusting reaction conditions.

ventional 4-probe pressed pellet samples provided important comparisons with the single crystal devices. Thus, the peak basal-plane single-crystal electrical conductivity of the Ni-CAT-1 crystals is 2 S/cm, with an average of 0.8 S/cm, whereas the conductivity of a polycrystalline pressed-pellet sample is 3.6×10^{-3} S/cm, similar to two previously reported values. In other words, the conductivity

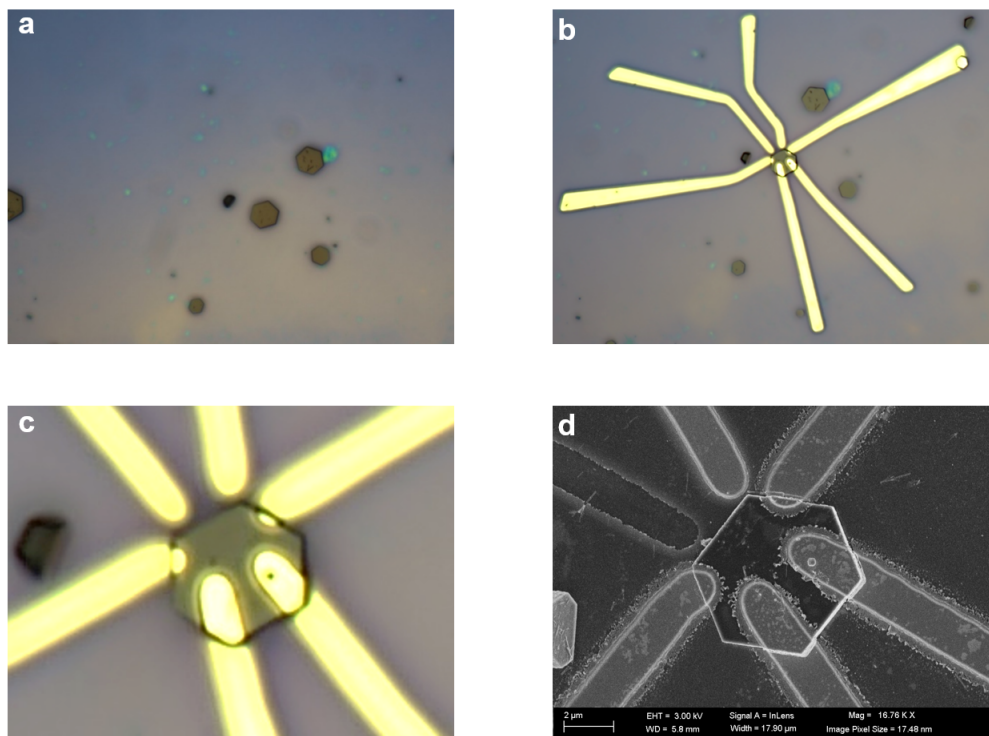


Figure 4.7: a, optical picture of the Ni-CAT-1 crystal. b,c shows the fabricated device via stencil mask technique. we deposited 600 nm Au to make electrical contacts to the flake. d, SEM micro picture of the device to extract the height of the flake.

of a polycrystalline pressed pellet of Ni-CAT-1 is lower by more than two orders of magnitude, as may be expected given the grain boundaries and contributions from the lower, out-of-plane, c axis conductivity estimated at 10×10^{-4} S/cm from a two probe device. The presence of traps at grain boundaries is further confirmed by a temperature-dependent conductivity study (Fig. 4.9A), which gives an activation energy of 0.09 eV for the single crystal, and 0.14 eV for the pressed pellet devices.

A Hall measurement on a single crystal device of Ni-CAT-1 provided unique insight into the nature of in-plane electrical transport in 2D π MOFs. The Hall coefficient obtained from fitting the data in Fig. 4.9G, (-0.46 ± 0.14) cm³/C, is relatively small compared to the conductivity. This suggests that

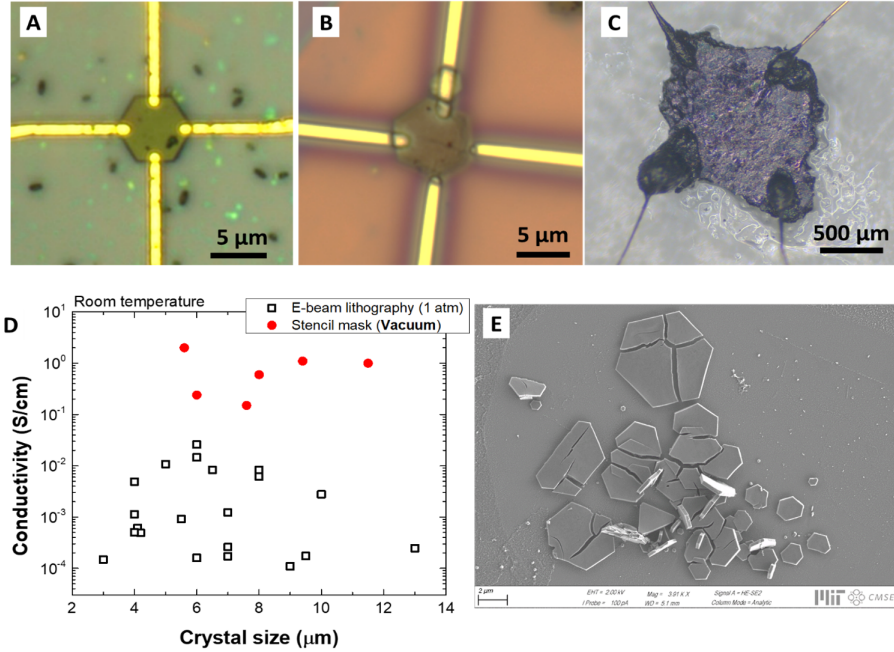


Figure 4.8: (A C) Optical microscope images of fabricated devices. (A) A device made by electron beam lithography (B) A device fabricated with stencil mask technique. (C) A pressed-pellet device. (D) Electrical conductivities with various crystal sizes using the two fabrication methods. Note that the electrical conductivity increases by one order of magnitude under vacuum. All the devices fabricated with the stencil mask technique were measured under vacuum and the others were measured in an ambient environment. The electron beam lithography conditions were destructive to the crystals. The fabrication yield was about 50%, and the measured conductivity varies by two orders of magnitude for 21 samples. The stencil-mask samples show higher conductivity than electron beam samples and spread over one order of magnitude. Although the electron beam process was destructive, the best-measured conductivity of electron beam samples was similar to the stencil mask process. Therefore, further optimization of growth and fabrication parameters are required to use the electron beam lithography process. (E) An example of the single-crystal fracture after device fabrication with electron-beam lithography technique. Some crystals, especially bigger ones, tend to crack easier.

the origin of the high conductivity in this particular material is a high carrier concentration rather than fast carrier transport. Given its small bandgap of 0.2 eV, Ni-CAT-1 may intrinsically possess high densities of electrons and holes at room temperature. However, assuming n-type behavior, consistent with the sign of the Hall coefficient, gives an electron density of $(-1.4 \pm 0.42) \times 10^{19} \text{ cm}^{-3}$, which corresponds to 1% of HHTP-site density, and a corresponding electron mobility of $(0.16 \pm 0.049) \text{ cm}^2/\text{V.S}$. Whereas the single crystals of Ni-CAT-1 generate a distinct Hall effect, we were unable to

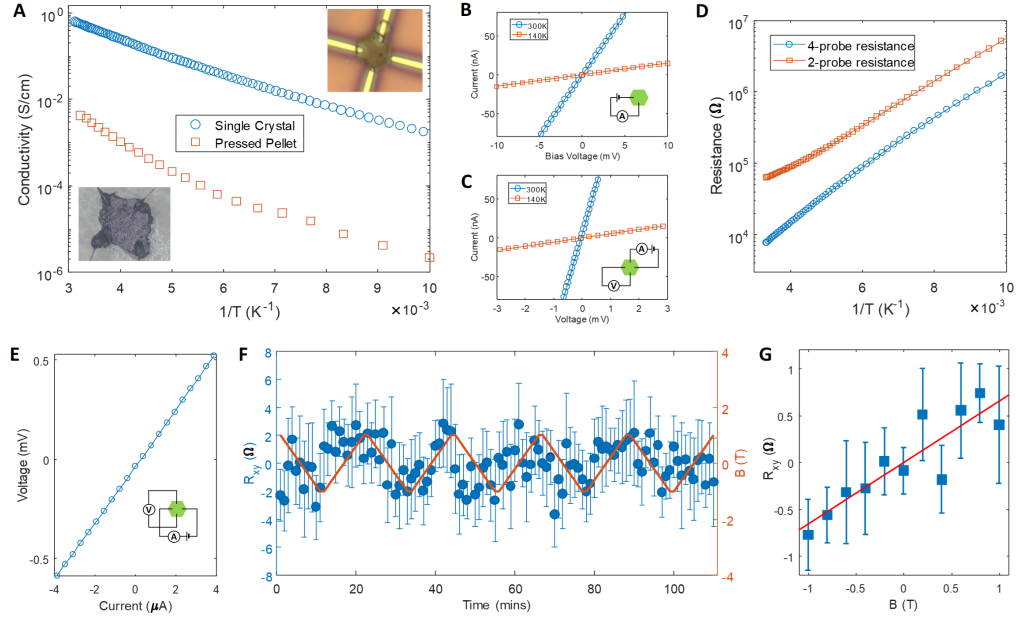


Figure 4.9: . (A) Temperature dependence of electrical conductivity along the basal plane of a single crystal and of a pressed pellet. Inset: optical microscope images of single-crystal and pressed-pellet devices. (B and C) Current–voltage (I–V) curves of 2-probe (B) and 4-probe (C) measurements on a single crystal. (D) Temperature dependence of 2-probe and 4-probe resistance. (E) I–V characteristics of Hall measurement at room temperature and 1 T. (F) Hall resistance (R_{xy} , blue circle) as a function of time, while the magnetic field (B, red line) is slowly swept between -1 and 1 T. The Hall resistance is determined from the slope of I–V curve in (E) and subtracting magnetic-field independent offset (Figure S14). (G) Mean Hall resistances as a function of the magnetic field. The Hall coefficient is -0.46 ± 0.14 cm^3/C , indicating that the high conductivity of Ni-CAT-1 originates from a high carrier density. Error bars are the standard error of the mean.

measure the Hall effect in pressed pellet samples due to suppression of the charge carrier mobility by grain boundaries. Recalling that the pressed pellet samples also exhibited nearly three orders of magnitude decrease in conductivity, these measurements provide an important direct assessment of charge carrier densities in 2D π MOFs and confirm that the single crystal samples exhibit significantly superior electronic properties overall.

Biphase solution-solid growth of large planar single crystals of Ni-CAT-1 allow characterization of its intrinsic electronic properties along the 2D plane. Based on these promising results, we further anticipate that applications of this growth technique will enhance the performance of other,

highly-conductive 2D π MOFs. Future studies of single-crystal 2D π MOFs should clarify fundamental structure-property relationships and allow measurement of intrinsic electronic and topologically-protected properties.

4.5 GRAPHULLERENE : SUPERATOMIC COUSIN OF GRAPHENE

C_{60} fullerene, the first synthetic carbon allotrop⁹⁰, is a geometrically closed, polycyclic polymer composed solely of carbon atoms (Fig. 4.10). This polymer is infinite in the literal sense of not having any termini, but it is obviously quite finite in being the size of a normal, albeit large, molecule. Graphene, another allotrope of elemental carbon⁹¹, is also a polymer of carbon atoms, but in this case, the polymerization leads to a geometrically open result: infinite, two-dimensional (2D) sheets (Fig. 4.10). In this report we disclose a new 2D polymer of C_{60} , which we synthesize by linking C_{60} molecules into layered, graphene-like hexagonal sheets (Fig. 4.10). By analogy to graphene and graphite, we have dubbed this material graphullerene and its 3D vdW solid, graphullerite.

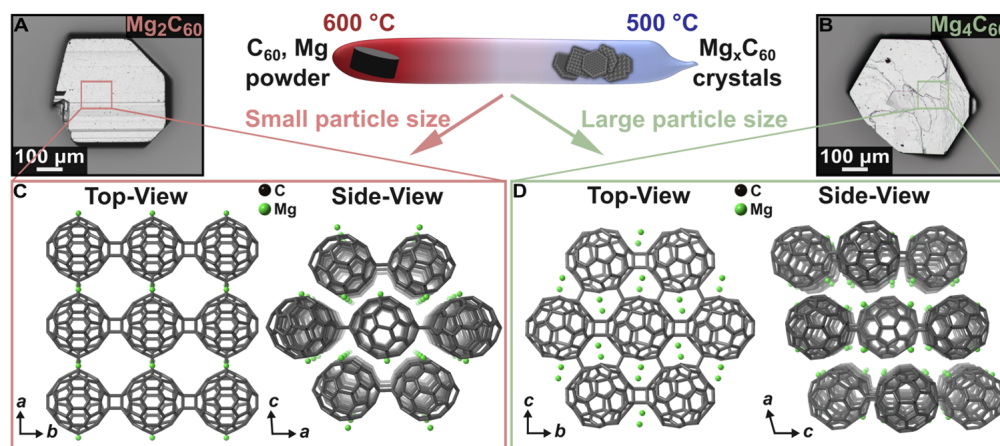


Figure 4.10: Schematic illustration of the CVT technique employed for the growth of single crystals. Optical micrographs of crystals of (A) $(Mg_2C_{60})_2$ and (B) $(Mg_4C_{60})_2$. Crystal structures of (C) $(Mg_2C_{60})_2$ and (D) $(Mg_4C_{60})_2$, with the top-view of a single layer for each compound alongside the side-view, showing the layered structures of the crystals.

Our chemical strategy to prepare graphullerene was inspired by a recent study of Yamanaka and

coworkers⁹², who employed the chemical vapor transport (CVT) approach to grow single crystals of metal-doped polyfullerides. First, we grow single crystals of Mg-doped polyfulleride (Mg_4C_{60}). These polyfullerides are obtained by pressing a pellet of C_{60} and Mg powder under inert atmosphere, which is then sealed in a fused silica tube under vacuum, and placed in a horizontal furnace with a temperature gradient (Fig. 4.10a). Large black hexagonal crystals (hundreds of micrometers in lateral dimensions), with a metallic luster, are obtained at the cold end of the tube (Fig. 4.10b). Single crystal X-ray diffraction (SCXRD) reveals that the crystals have a layered structure, and display a quasi-hexagonal lattice, with each C_{60} forming eight covalent σ -bonds to six neighbors within a molecular plane. Four of these make single connections between the C_{60} molecules, and each of the other two pairs doubly connects the C_{60} 's (Fig. 4.10c). The synthesis yields highly reduced sheets with 4 Mg counterions per fullerene. The counterions are closely associated with each individual layer (Fig. 4.10c), and not shared between layers; hence, the layers are only weakly bonded to each other, predominantly through vdW interactions. Single crystals of (Mg_4C_{60}) were recently grown by Hou et al. as well, using a similar CVT approach⁹³.

To create a vdW C_{60} polymer material that can be mechanically exfoliated, we attempted to remove the Mg from the Mg_4C_{60} lattice by immersing the crystals in different aqueous acidic solutions, expecting Mg to form water-soluble salts with the conjugate bases. Suspending Mg_4C_{60} in dilute aqueous solutions of acetic acid or nitric acid leaches out most of the Mg, yielding $\text{Mg}_{0.5}\text{C}_{60}$, as determined by energy dispersive X-ray spectroscopy (EDS). By suspending the $\text{Mg}_{0.5}\text{C}_{60}$ crystals in N-methylpyrrolidone at 180° C, we completely remove the Mg counterions (Fig. 4.11a). Upon examining the graphullerite crystals using scanning electron microscopy (SEM), we find that the crystals remain intact following Mg deintercalation (Fig. 4.11a, inset). With Mg taken out, the remaining material is entirely and purely carbon, yet it is not C_{60} ; it is a new vdW solid, graphullerite (C_{60} in the Figures). Note that the lack of long-range registry of the covalent layers along the stacking direction, indicated by the broadening of the powder X-ray diffraction (PXRD) peaks, has thus far prevented

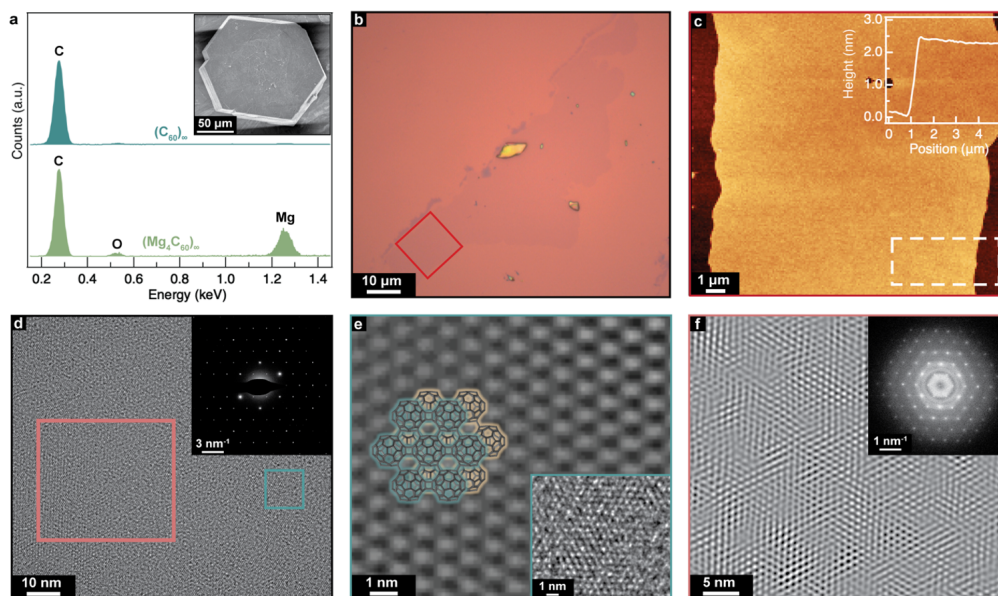


Figure 4.11: a, Elemental composition of single crystals before (Mg_4C_{60}) and after (C_{60}) treatment with a dilute acetic acid solution, as determined by EDS. The absence of the oxygen peak in the spectrum of graphullerite implies that the observed oxygen peak in Mg_4C_{60} crystals corresponds to oxidized Mg species and not the fullerene sheets. Inset: SEM image of a graphullerite crystal. b, Optical micrograph of mechanically exfoliated graphullerene. c, AFM image of the bilayer selected in red in (b). d, TEM image of a few-layer graphullerene flake prepared by mechanical exfoliation on a TEM grid. Inset: Selected area electron diffraction pattern from a $100 \times 100 \text{ nm}^2$ region of the flake. Low magnification TEM image of this flake is shown, iFFT of the area selected in green in (d), which is magnified in the inset. The filtering removes the aperiodic pixel noise and represents the lattice superstructure, showing that each C_{60} is connected to six neighboring fullerenes in a molecular plane. f, iFFT image of the area selected in pink in (d). The high degree of crystallinity can be observed in the Fourier transform (inset) and the electron diffraction pattern in (d).

structural determination using SCXRD.

The van der Waals structure of Mg_4C_{60} and observations of facile spontaneous exfoliation in air led us to speculate that pristine materials could be exfoliated. Through mechanical scotch tape exfoliation, uniform flakes with micrometer scale lateral dimensions were reliably obtained (Figure 4.12a). Exfoliated Mg_4C_{60} flakes are found to have thicknesses of roughly 5 layers, as derived from the flake thickness ($4.8 \pm 0.1 \text{ nm}$) and the interlayer crystallographic axis length (0.875 nm per layer) (Figure 4.14b).

The two-dimensional structure of Mg_4C_{60} inspired investigations into the electronic structure of

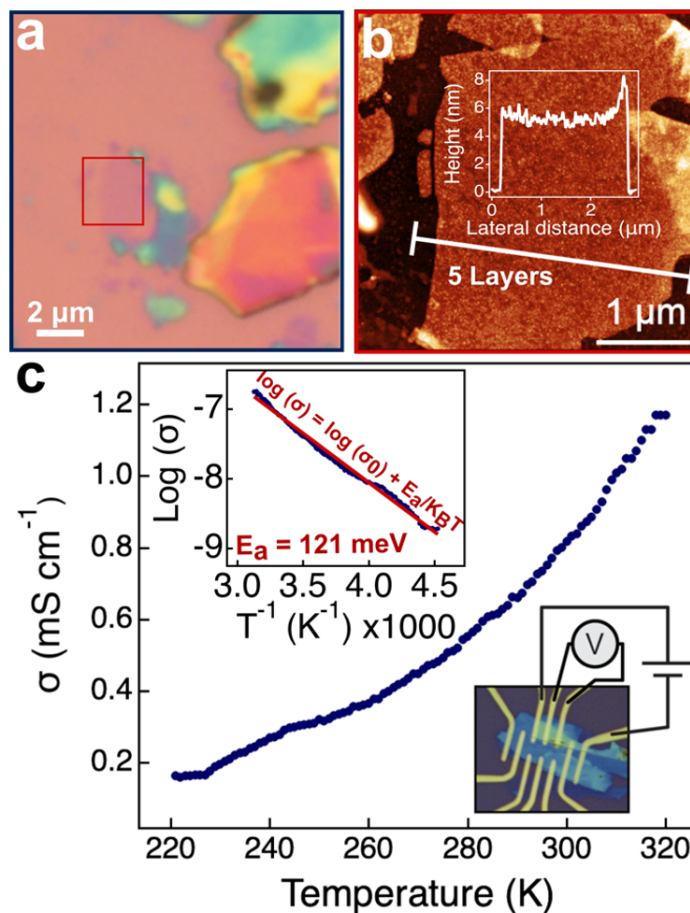


Figure 4.12: SEM images of (A) (Mg_4C_{60}) and (B) (Mg_2C_{60}) crystals. The weakly bonded flaky morphology of (Mg_4C_{60}) is seen in the magnified image of the area selected in beige. (C and D) Optical micrographs of mechanically exfoliated crystals: (Mg_4C_{60}) crystals are easily exfoliated to produce few-layer flakes (C), while (Mg_2C_{60}) breaks into small pieces (D). (E) AFM image of the flake selected in red in (C). (F) Log of the conductance versus temperature. Pink and green lines are the data for (Mg_2C_{60}) and (Mg_4C_{60}), respectively. A fit to a thermally activated (Arrhenius) model is given by the dashed lines. A typical device and corresponding 4-terminal measurement scheme are shown in the inset.

these materials, which reveal that Mg_4C_{60} is semiconducting along the in-plane direction. The ability to exfoliate the crystals allowed us to fabricate rigorously air-free devices and eliminate possible artifacts that might arise from using solvent based conducting paints usually used for applying contacts on bulk crystals. Four-terminal transport measurements on ~ 100 nm thick flakes show that the conductivity increases with increasing temperature with a room temperature conductivity of $\sigma = 0.82$

mS cm⁻¹ (Figure 4.12c). This positive dependence between temperature and electronic conductivity indicates that Mg₄C₆₀ is semiconducting. Fitting an Arrhenius thermal activation model reveals an extremely low activation (E_a) threshold of 121 meV along the in-plane direction (Figure 4.12c, inset), suggesting that electrons can easily traverse covalently bonded fullerenes. Our attempts to measure the conductance along the cross-plane direction showed that Mg₄C₆₀ is highly insulating along the stacking direction ($R > 2 \text{ G Ohm}$), emphasizing that charge-transport is likely facilitated by the small cofacial distance and covalent bonding within a molecular plane. Though the crystallographic structure of Mg₄C₆₀ is weakly disrupted by air exposure, the electronic structure transitions from semiconducting to electronically insulating upon air-exposure. This evolution implies that the charge-carriers measured in the pristine material are introduced via reduction by Mg and removed through atmospheric oxidation. Also, we attempted to fabricate with a few layer graphullerite. Due to semiconducting nature of the material, we had a problem to make metal reliable contacts to them. One of the next step would be contact engineering for this novel material to explore their properties in lower temperature.

To realize the technological promises of 2D materials, it is critical to grow macroscopic single crystals that can provide high-quality macroscopic flakes with clean surfaces. We have presented a new chemical strategy to grow a 2D polymer of C₆₀ as large single crystals that are readily exfoliatable. The ability of graphullerite to withstand grinding, oxidation, and treatment with acid highlights the strong in-plane covalent bonding between the fullerenes. Graphullerite vdW crystals are charge neutral and the exfoliated molecularly-thin flakes have no residual counterions or impurities, providing a unique platform for the investigations of confined light, and the construction of quantum materials-based devices

5

Heavy Fermions in the 2D Limits

5.1 INTRODUCTION

Crystals with strongly interacting electrons exhibit fascinating properties that challenge basic concepts of physics and expand our knowledge of possible electronic states. One of the most successful strategies to prepare so-called strongly correlated materials is to design crystalline solids in which localized magnetic moments can entangle with itinerant electrons to produce a coherent narrow band of

heavy fermions. The basic ingredients of such heavy fermion materials are a lattice of local magnetic moments (typically from f -elements with unpaired spins) and a sea of metallic conduction electrons. These materials are most commonly found in 3D intermetallic metals that have one of their elements from the lanthanide or actinide series (most commonly Ce, Yb or U)^{19,20,16,17}.

The realization of 2D heavy fermion materials offers entirely new approaches to tune this coupling and to access these quantum phases, opening up a myriad of opportunities. Confining the electrons to two dimensions increases their interactions due to the reduced Coulomb screening, which may strengthen quantum fluctuations. Moreover, 2D materials prepared from vdW crystals can be stacked, strained, twisted and integrated into heterostructures and gateable electronic devices, providing new possibilities for manipulating the heavy fermion state. While a few notable low-dimensional heavy fermion materials have been theoretically proposed and experimentally reported, including epitaxially-grown CeIn₃/LaIn₃ superlattices and related structures⁹⁴, ³He bilayers⁹⁵ and 1T/1H TaS₂ 2D heterostructures⁹⁶, a genuine 2D vdW material with an intrinsic heavy fermion ground state has not yet been discovered. In our search for such a material, we identified CeSiI⁹⁷ as a promising candidate because (i) the spin $\frac{1}{2}$ state of the Ce atoms is ubiquitous in heavy fermion compounds; (ii) previous electrical transport measurements and Zintl-Klemm formalism suggest a metallic character; and (iii) the crystal structure of CeSiI points to weakly interacting vdW layers and a highly dimensionally-confined electronic system.

In this chapter, first, I introduce CeSiI as promising candidate to study Kondo physics at low dimensions. I then describe the device fabrication and complexity of it to prepare the proper platform to study electrical transport in this system. Also, I will present the magneto transport measurements which reveal some evidence about the Fermi surface reconstruction and Kondo lattice formation in CeSiI down to the few layer level. At the end, I will discuss transport study atomically thin CeSiI in the limit of 4 unit cell thickness.

5.2 CeSiI NEW CANDIDATE FOR 2D HEAVY FERMIONS

The Roy group at Columbia university synthesized single crystals of CeSiI from the high temperature reaction of Ce, Si and CeI₃ in Nb ampules welded shut under Ar and encapsulated in sealed fused silica tubes⁹⁸. The highly air sensitive crystals isolated from this reaction are thin hexagonal plates with a copper metallic sheen (Fig. 5.1a). The crystal structure of CeSiI (Fig. 5.1b), determined by single crystal X-ray diffraction (SCXRD), is remarkable: each layer consists of a nearly flat 2D honeycomb sheet of Si (i.e. silicene), sandwiched between two triangular layers of Ce atoms (Fig. 5.1c). The vdW layers are capped with iodine atoms and stacked along the c-direction to produce a trigonal lattice with space group $P\bar{3}m1$ (Fig. 5.1d). Crystals of CeSiI can be mechanically exfoliated on Si wafers with a 100 nm Si₃N₄ layer to produce flakes of various thicknesses with lateral dimensions of tens of microns as measured by optical microscopy (Fig. 5.1e). Using this method, we were able to isolate flakes as thin as trilayers, determined by atomic force microscopy (AFM) (Fig. 5.1f). Even thinner flakes could also be identified by optical microscopy. The average layer thickness measured by AFM on mechanically exfoliated flakes is ~ 1.3 nm, in excellent agreement with the layer thickness determined from SCXRD data (~ 1.2 nm).

Our collaborator showed that the first time the heavy fermion state of bulk CeSiI using a comprehensive set of thermodynamic (heat capacity, magnetic susceptibility and electrical transport) probes. By measuring the electrical transport properties of few-layer flakes, I demonstrate the possibility of achieving a dimensionally confined heavy fermion material and exploring the layer dependence of its behavior down to the 2D regime. We find that the transport characteristics of a thinner flake is typical of antiferromagnetic heavy fermion compounds and is analogous to the bulk transport characteristics measured on single crystal devices. The quintessential experimental evidence for heavy fermion behavior is the Sommerfeld coefficient (γ) calculated from heat capacity. The Sommerfeld coefficient is proportional to the effective electron mass, and therefore a larger γ is generally attributed to stronger

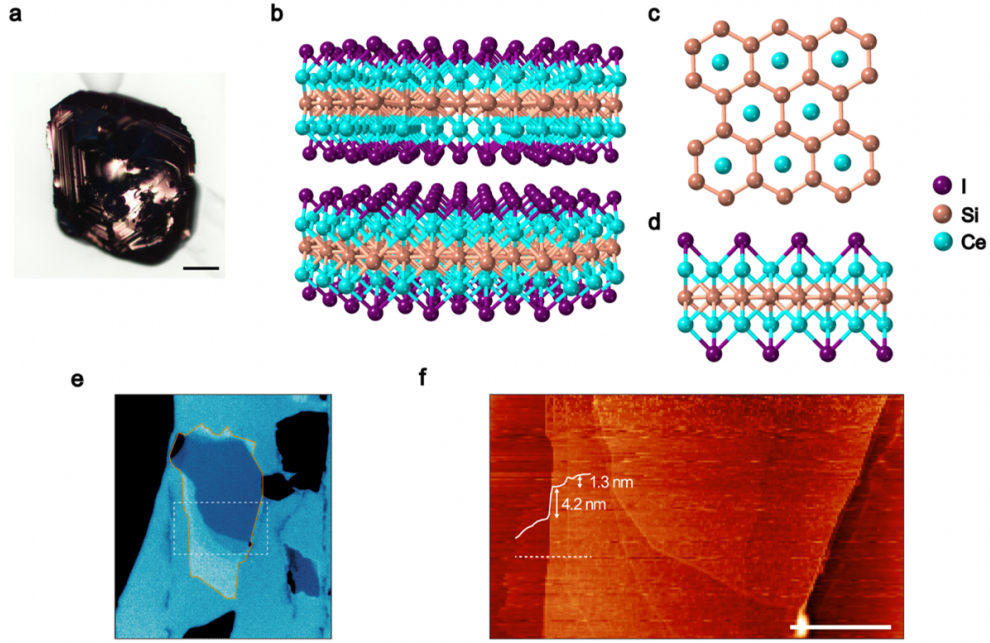


Figure 5.1: **a**, An image of a CeSiI crystal with a scale bar of $100 \mu m$. **b**, The layered crystal structure of CeSiI. **c**, A top view of the crystal structure with the iodine atoms removed to show the silicene layer. **d**, A side view of CeSiI. **e**, An optical image of a CeSiI crystal exfoliated with scotch tape on a Si_3N_4 wafer with the flake outlined in orange. **f**, An AFM image of the same thin flake with the step height overlaid.

electronic correlations. Figure 5.2a displays the heat capacity (C) of CeSiI single crystals at different applied magnetic fields (B) with a distinct λ -type second-order transition around ~ 7 K attributed to antiferromagnetic (AFM) ordering of the Ce atoms, as discussed below. The value of γ is extracted from the fit of the heat capacity data according to the equation:

$$\frac{C}{T} = \gamma + \beta T^2 \quad (5.1)$$

where β represents a proportionality constant for the phonon contribution to C . Extrapolation to $T = 0$ K of the fits of the C/T versus T^2 graph (Fig. 5.2b) above the Neel temperature ($T_N = 7$ K)

gives $\gamma = 0.15 \text{ J mol}^{-1} \text{ K}^{-2}$ at $B = 0 \text{ T}$, implying moderate electronic correlations and the existence of a heavy fermion state. As B increases, γ also increases due to stronger interactions between the heavy quasiparticles, reaching $0.35 \text{ J mol}^{-1} \text{ K}^{-2}$ at $B = 9 \text{ T}$ (inset of Fig. 5.2b). Like other antiferromagnetic Ce-based heavy fermion systems, CeSiI displays a significantly larger γ below T_N , indicating the formation of heavier quasiparticles in the magnetic state. Additional heat capacity measurements on pressed pellets of single crystals give similar values of $\gamma = 0.19 \text{ J mol}^{-1} \text{ K}^{-2}$ and $0.17 \text{ J mol}^{-1} \text{ K}^{-2}$. Heat capacity measured down to dilution fridge temperatures also confirms the large effective electron mass even with an impurity at $T \sim 1 \text{ K}$.

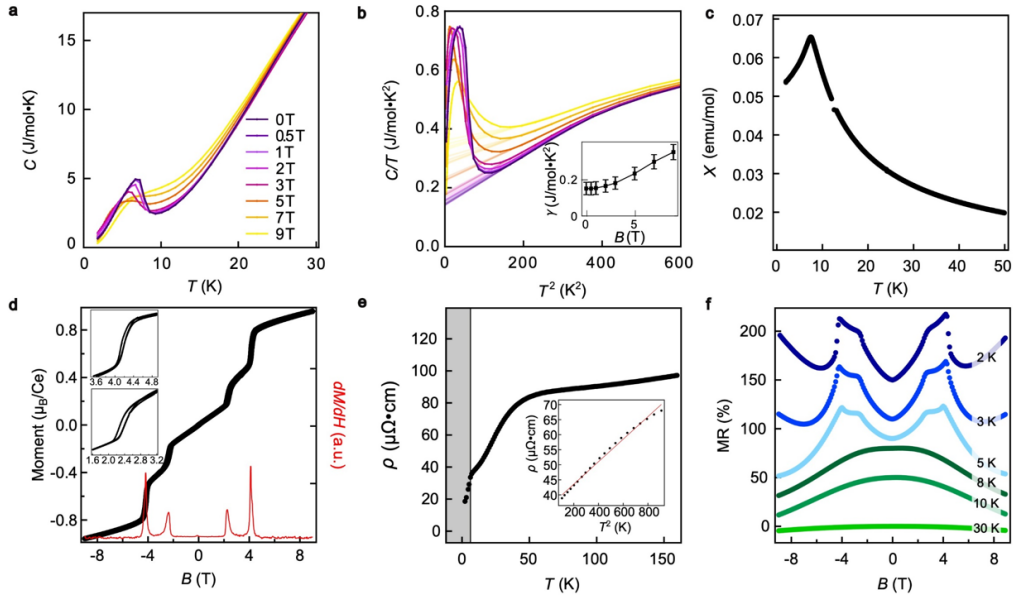


Figure 5.2: **a**, Heat capacity of CeSiI crystals at different fields. **b** C/T fit extrapolated to 0 K to determine the Sommerfeld coefficient. The inset shows the change in the coefficient as a function of magnetic field. **c**, The magnetic susceptibility as a function of temperature measured with a field of 1 T with $B \parallel c$. **d**, The field-dependent moment in Bohr magnetons per Ce atom. The red curve displays the derivative. Both insets show the hysteresis loop for both metamagnetic transitions. **e**, The temperature dependence of the resistivity and its derivative with the antiferromagnetically ordered lattice indicated by the grey highlighted region. The inset displays the resistivity as a function of T^2 with the red line displaying the Fermi liquid fit. **f**, The magnetoresistance at multiple temperatures.[measurements was done by our collaborator at Columbia]

To better understand the heat capacity anomaly near 7 K, our collaborator measured the magnetic susceptibility (χ) of bulk CeSiI single crystals. With B parallel to the crystallographic c -axis, the temperature dependence of χ displays a sharp maximum at 7 K (Fig. 5.2c), indicating the onset of AFM order. For $B \parallel c$ -axis, the magnetization (M) at $T = 2$ K increases linearly with field, consistent with AFM ordering. With increasing B , we observe two distinct metamagnetic transitions (Fig. 5.2d), occurring at 2.3 and 4.1 T, with the first reaching a magnetization plateau at $0.4 \mu_B/\text{Ce}$ and the second reaching a magnetization of $\sim 0.9 \mu_B/\text{Ce}$ at $B = 9$ T. Both of these transitions contain a small open hysteresis and are only observed below T_N , suggesting they are associated with ordering of the Ce moments. Similar magnetic plateaus have been observed in magnetically frustrated triangular lattice materials, other Ce-based heavy fermion compounds, and the heavy fermion system, URu_2Si_2 , due to Fermi surface reconstruction. Though the magnetic structure in the plateau region of CeSiI has not been identified, a recent neutron diffraction study suggested that geometric frustration and possible cycloidal ordering of the Ce moments could explain the magnetic transitions observed here. Furthermore, the expected magnetic ground state of a $S = 1/2$ system is confirmed with an estimated entropy close to $R\ln(2)$ determined from the heat capacity data (where R is the ideal gas constant).

In addition to confirming the overall metallicity of CeSiI, electrical transport measurements on bulk single crystals show clear evidence of competition between the RKKY-mediated magnetic order and the Kondo lattice behavior. The temperature dependence of the resistivity (ρ) features a sharp anomaly at 7 K resulting from the AFM ordering (Fig. 5.2e). More revealingly, the curve does not follow the typical trend of a metal. Instead of decreasing and saturating at a residual resistance, the material experiences a large drop in resistivity around 50 K due to the ordering of Kondo singlets into a coherent Kondo lattice, leading to reduced scattering of the conduction electrons. Such a drop in resistivity at the onset of the Kondo lattice is typical of heavy fermion systems. The low-temperature behavior above the magnetic ordering temperature follows Fermi liquid behavior with a linear relationship between ρ and T^2 (inset of 5.2e). Below T_N , the magnetoresistance (MR) presents two dis-

tinct peaks that align exactly with the metamagnetic transitions in the M versus B curves (Fig. 5.2f). These peaks disappear above T_N , indicating they are related to the magnetic order. Unlike the M vs. H curve, the MR does not display a hysteresis at the metamagnetic transitions, and instead exhibits a change in slope from one transition to the next. The arrangement of the spins after the second transition causes a drastic decrease in resistance and from here, the continued increase in field causes a positive magnetoresistance to occur. The exact magnetic origin of these transitions and their angle dependence is currently under exploration along with how the existence of the Kondo lattice and its interplay with the magnetism potentially affects them.

5.3 AIR & SOLVENT FREE DEVICE FABRICATION FOR FEW LAYER CesiI

The verification of the 2D electronic system and the inherent layered structure of CesiI makes 2D transport an exciting avenue to explore the effect of dimensionality on its heavy fermion behavior. With the air sensitivity exhibited by bulk crystals, exfoliated flakes are more reactive and because of this device fabrication is extremely complex. CesiI crystal was mechanically exfoliated onto SiO₂/Si substrates inside Argon glovebox with <0.1 ppm O₂ and H₂O. The substrate was baked on hot plate at 300 C for more than 24 hours to remove any water residue from the surface. Flakes of desired thicknesses were identified by optical contrast. We used a high-resolution stencil mask technique to fabricate the devices. This process is free of solvents and polymers and helped to preserve the quality of crystal. In addition, it can be done air free inside the glovebox. Stencil masks were fabricated from Si₃N₄(500nm)/Si(300nm)/ Si₃N₄(500nm) wafers. At first step, combination of photolithography, reactive ion etching and wet etching (potassium hydroxide solution) were used to create 200 and 500 μm square windows of Si₃N₄. Subsequently, the desired patterns of devices were written with photolithography on the windows. In the last step, we used reactive ion etching to remove Si₃N₄ in exposed patterned area. We used a micropositioner to align and place the prefabricated Si₃N₄ masks

on designated flakes. A small amount of vacuum grease (Apiezon H) was used to glue the mask to the substrate. We finished the device fabrication by evaporating Au metal as electrical contacts. Finally, the fabricated device is covered with hBN (thickness 20 to 40 nm) to provide extra protection from degradation. A flake down to 15-layers was obtained from the mechanical exfoliation of CeSiI onto Si wafers with a 285 nm SiO₂ layer (Figs. 5.3a). SiN membrane based stencil mask technique was used to fabricate devices inside the Ar filled glovebox. The fabricated device covered with 40 nm hBN prior to load in cryostat to provide extra protection against degradation due to loading process. AFM on the hBN covered device exhibits a flake thickness of 20 nm, corresponding to 15 atomic unit cell layers (Fig 5.4).

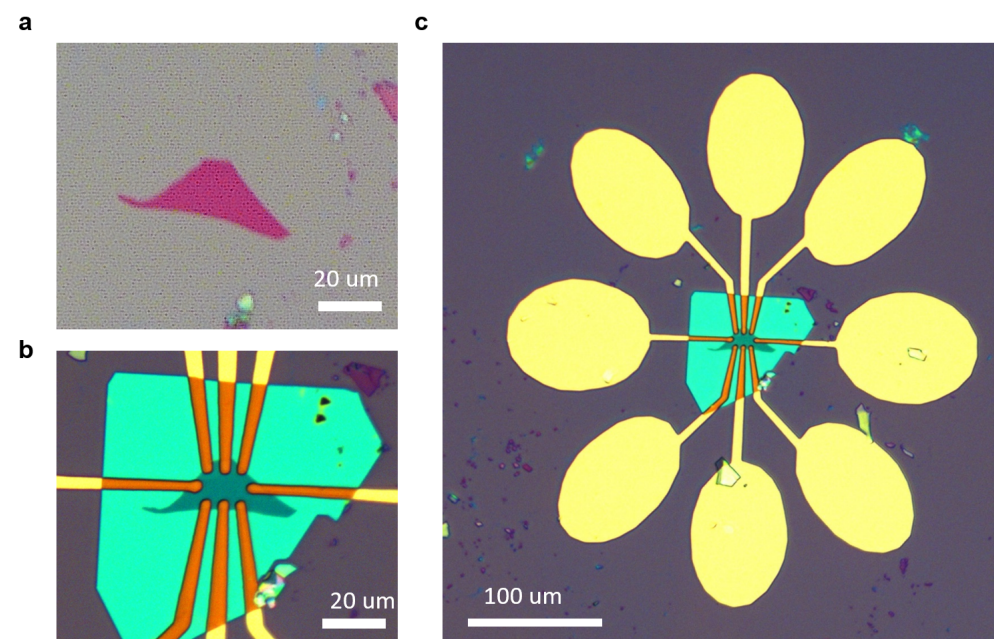


Figure 5.3: a, Optical micrograph 15 layers of CeSiI flake. the crystal exfoliated on a Si/SiO₂ substrate which was baked for more than 24 hr on hot plate at 300 C. b, final device covered with 40 nm hBN. the gold contact deposited with stencil mask technique. c, overall device picture with contact pads.

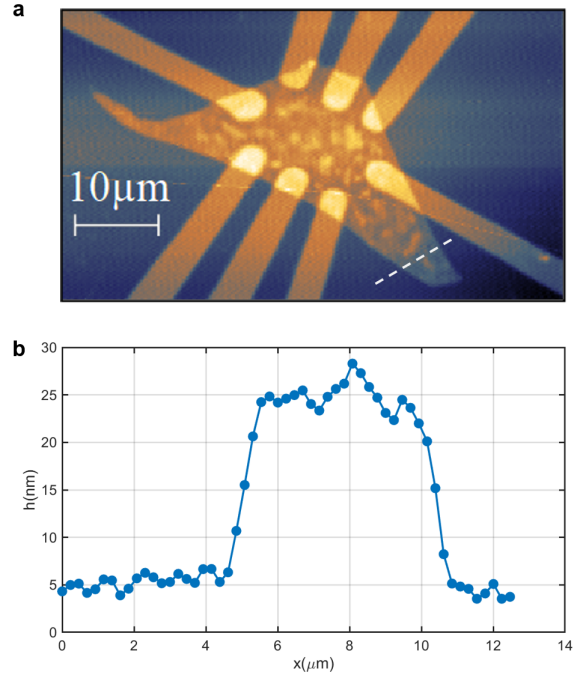


Figure 5.4: **a**, AFM of the device show after measurements. the scale bar is 10μm. the dash line cut is used to measure the thickness of flake. the dots on flake appeared due to degradation after unloading from glovebox. The AFM performed 10 minutes after unloading from cryostat to minimize the degradation. **b**, the line cut shows the height of the CeSiI covered flake. the height is about 20 nm which is equal to 15 layers of CeSiI (each layer is ~ 1.3 nm)

5.4 ELECTRICAL TRANSPORT : KONDO LATTICE ON FEW LAYER CESiI

The temperature dependence of the resistivity of the few layers device (Fig. 5.5) displays the same characteristics of the bulk single crystal measurement shown in Fig. 5.2e with an antiferromagnetic transition at ~7 K and the Kondo lattice formation at ~40 K. The decrease in the resistivity from the onset of the Kondo lattice indicates that the heavy fermion behavior persists at least down to 15 layers. Coherent states are developed in the Kondo lattice regime. The fermi liquid behaviour is expected for coherent state :

$$\rho(T) = \rho_0 + AT^2 \quad (5.2)$$

Figure 5.6a shows fitting for R_{xx} vs T^2 of sample between 10 K to 25 K. The linear fit line in this graph indicates the existence of Fermi liquid in Kondo lattice regime. We also fit the data for lower temperature between 2 K to 7 K (Fig 5.6b). The R_{xx} has T^2 dependency in magnetic order state. We need to perform measurement in lower T to understand the power law and nature of quasi particle exists in AFM state.

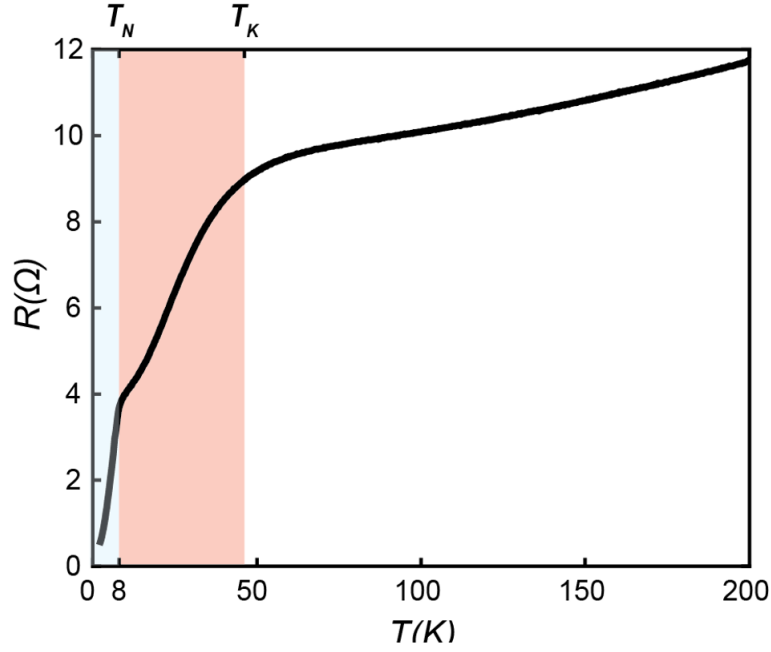


Figure 5.5: Longitudinal resistance, R_{xx} as temperatures, shows sudden dropping around 40 K (T_K) and 8 K (T_N). Coherent states are developed at both states.

5.5 MAGNETO-RESISTANCE AND FERMI SURFACE RECONSTRUCTION FOR FEW CE₂SI

We also measure the temperature dependent magneto resistance(MR) and Hall resistance on the few layer device. As shown in Fig. 5.7, the low temperature MR exhibits sharp kinks near the metamagnetic transitions (4 - 5 T B perpendicular to the flake) observed in magnetization below T_N , with two

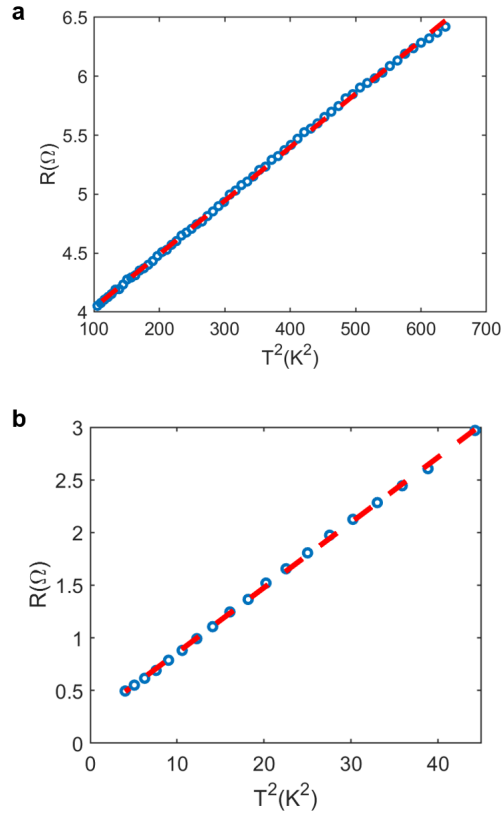


Figure 5.6: **a**, fermi liquid fit of R_{xx} depicts for 10 K to 25 K. **b**,fermi liquid fit of R_{xx} presents for 2 K to 6 K.

clear transitions observed. We can explain each of the kinks based on magnetic ordering transitions: The first kink happens around 2 T, potentially due to competing RKKY and Kondo interactions. The results can develop the R_{xx} plateaus between 2 T to 4 T, and above 4 T, the magnetic ordering to a paramagnetic state with localized magnetic moments.

Owing to atomically thin samples (20 nm), we also obtain higher resolution temperature dependent Hall measurements, allowing us to probe Fermi surface reconstruction through Kondo lattice formation. Figure 5.8 presents 2D plot of Hall resistance vs magnetic field from 120 K down to 2 K. The carrier density of any enclosed Fermi surface can be estimated from the differential Hall resis-

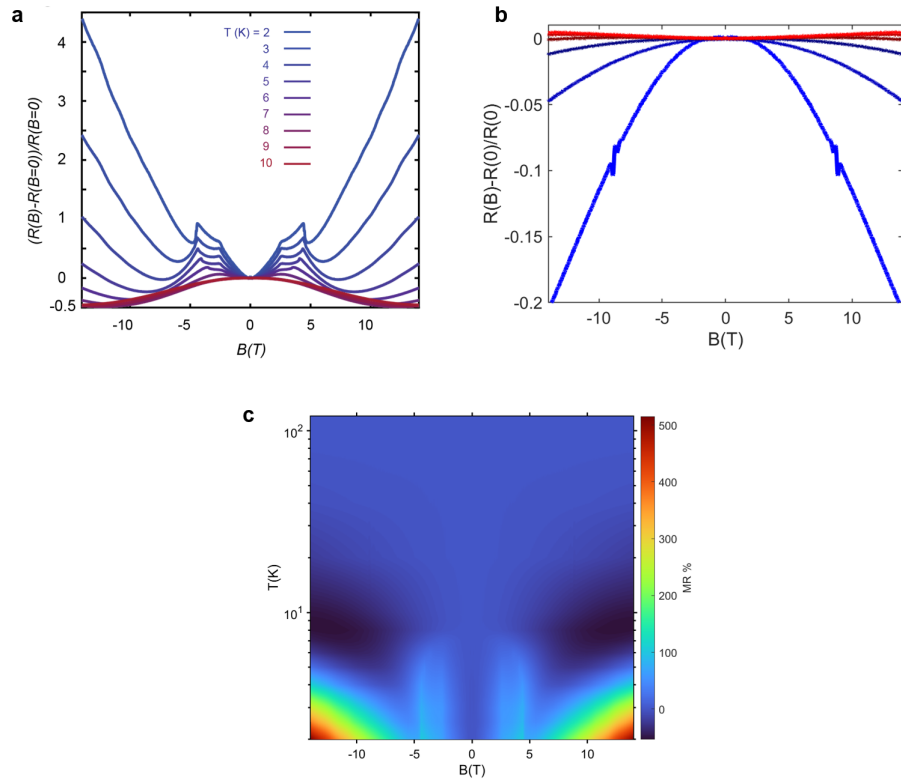


Figure 5.7: a,b, line cut from of 2D plots for 2 K to 120 K temperatures. the result show clear two magnetic transitions at 2 T and 4 T below 7 K. R_{xx} has negative MR above T_N . c, 2D plot of normalized Magnetoresistance change of R_{xx} for range of temperatures 2 K to 120 K as a function of B .

tance, dR_{xy}/dB at high and low magnetic field limits. Here we estimate at the net carrier density at the high magnetic field (8 T to 14 T) regime and the low magnetic field (-0.5 to 0.5 T) regime, separate by the metamagnetic transitions. We find that the Hall measurements exhibit three distinct temperature regimes in 2D plot: $T > T_{cob}$ (40 K), T_N (7 K) $< T < T_{cob}$ (40 K), $T < T_N$ (7 K). At high B , the Hall coefficient simply proportional to the total carrier density. The Hall slopes in this limit are found to be almost constant down to 20 K. The net carrier density is estimated to be $\sim 3.3 \pm 0.1 \times 10^{15} \text{ cm}^{-2}$ electrons per layer. At low B , on the contrary, the Hall slopes are affected by scattering process in microscopic scales. We find that the Hall coefficients between 120 K to 40K transforms from semi linear behavior at higher temperature to more nonlinear when temperature approach closer to T_{cob} .

The observed transition from linear to non-linear behavior of $R_{xy}(B)$ suggest a gradual formation of new transport channel with different carrier sign. Figure 5.10 shows dR_{xy}/dB obtained in these two different magnetic field limits as a function of T . We find that that dR_{xy}/dB in the both high and low magnetic field limits are negative for $T > T_{cob}$, but the low field dR_{xy}/dB changes its sign at T_{cob} . The total net carrier density at 2 K estimated from the low field limit is $\sim 1.2 \pm 0.2 \times 10^{15} \text{ cm}^{-2}$ holes per layer. As shown in Fig 5.10, we also note that sharp changes of the sign of dR_{xy}/dB are observed at magnetic field larger than the metamagnetic transitions field (4.5 T). This transition magnetic field B^* tends to increase with T persisting above T_N , suggesting the origin of this phenomena is not entirely due to magnetic ordering. Presence of B^* , combined with the gradually change of dR_{xy}/dB , proposes possibilities that at least two different Fermi surfaces, sharply reconstructed by magnetic fields, may contribute to electrical charge transports.

We also observed very slow Shubnikov–de Haas (sdH) oscillation in R_{xx} vs $1/B$ in high magnetic field in low temperature (Fig 5.11) on the top of the linear background. The carrier density extracts from these oscillations corresponds to $\sim 3.8 \times 10^{12} \text{ cm}^{-2}$. We need more measurements to figure out the origin of this SdH oscillation.

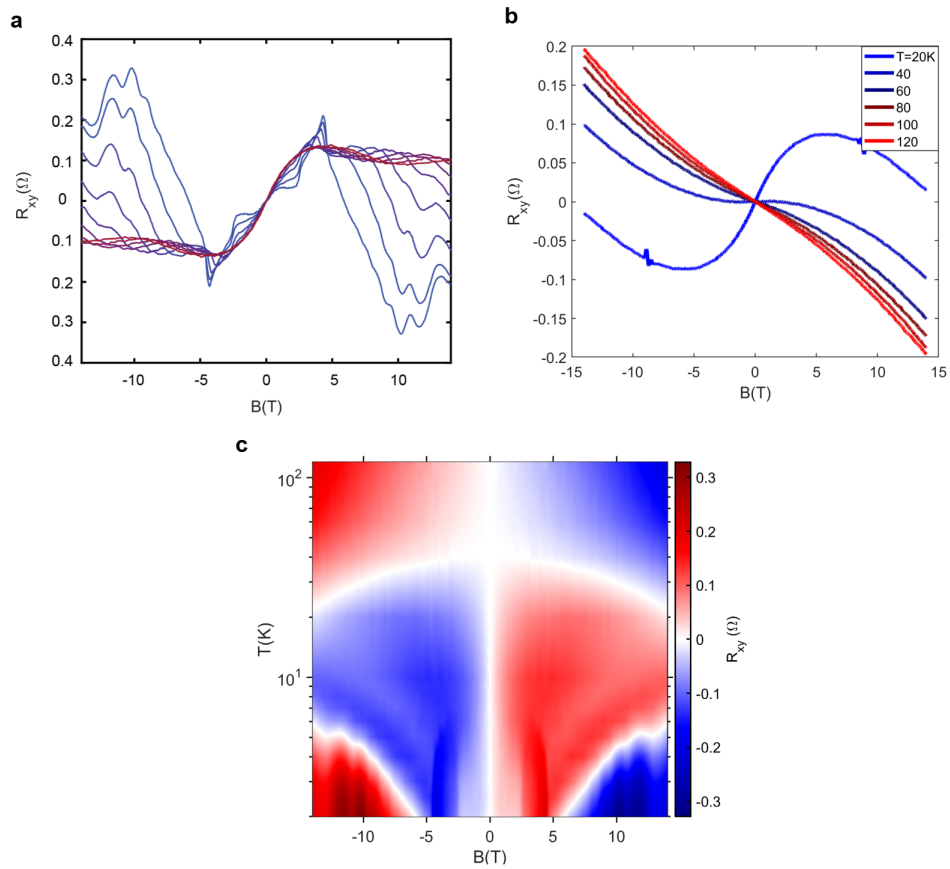


Figure 5.8: a,b, line cut from of 2D plots for 2 K to 120 K temperatures. the result show two different slope between 0 T and 4 T and above 4 T below 40 K. R_{xy} has almost linear above 80 K. c, 2D plot of Magnetoresistance of R_{xy} for range of temperatures 2 K to 120 K.

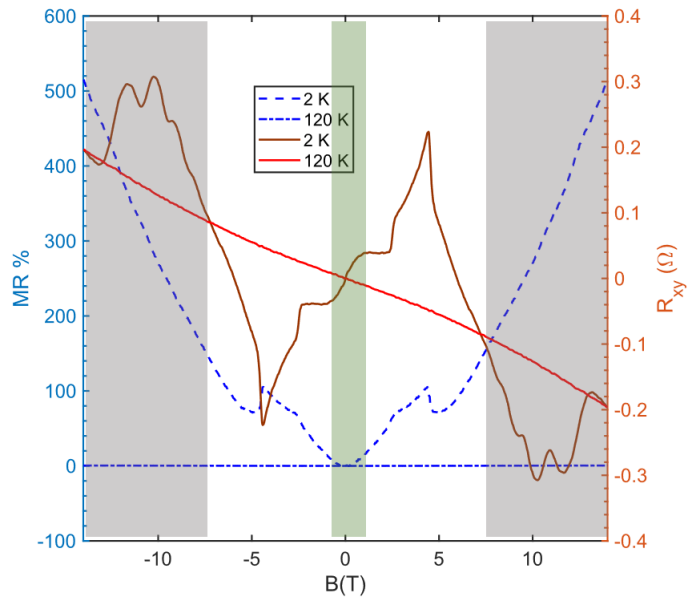


Figure 5.9: MR line cut from of 2D plots for 2 K and 120 K temperatures, the light gray and green area have been used to estimate hall coefficients for high and low magnetic field.

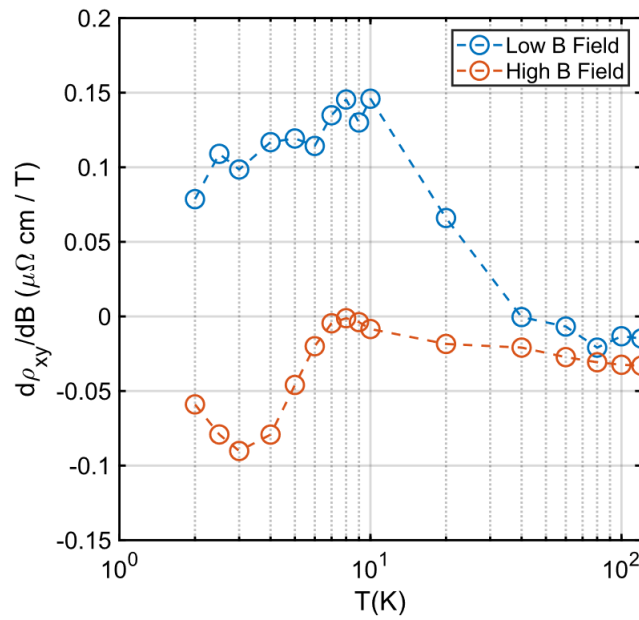


Figure 5.10: Differential Hall coefficients for high and low magnetic field as temperatures from 120 K down to 2 K.

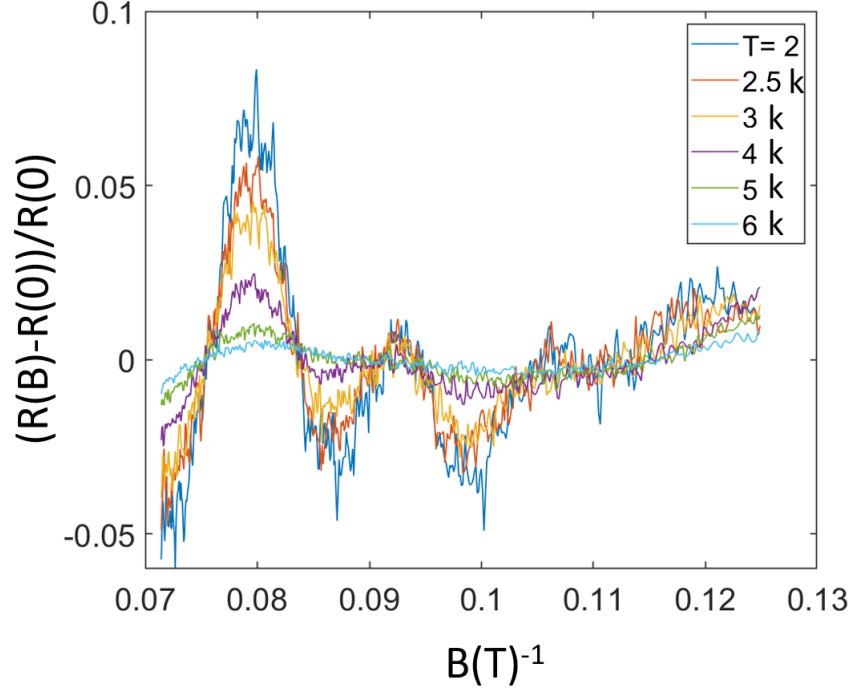


Figure 5.11: Shubnikov-de Haas oscillation in R_{xx} for T 2K to 6 K. we extracted the electron density of $\sim 3.8 \times 10^{12} \text{ cm}^{-2}$.

5.6 MAGNETO-RESISTANCES FOR 4 LAYERS CeSiI

We further push our device fabrication toward the samples in the atomically thin 2D limit . A preliminary device of 4 layers (Fig 5.12) strongly suggests that the heavy fermion behavior persists in the 2D regime. The resistivity versus temperature curve suggests that both the magnetic and Kondo lattice order still exists at the 4-layers limit . Furthermore, the magnetoresistance indicates that the metamagnetic transitions are still preserved. The existence of both the complex magnetism and the heavy fermion system in the 2D make CeSiI a promising candidate for manipulating the coupling between the magnetism and itinerant electrons with gating, strain, twisting, and incorporating into heterostructures. A recent theory study highlights strain and surface hole doping as promising avenues

for tuning the Kondo resonance of the CeSiI monolayer .

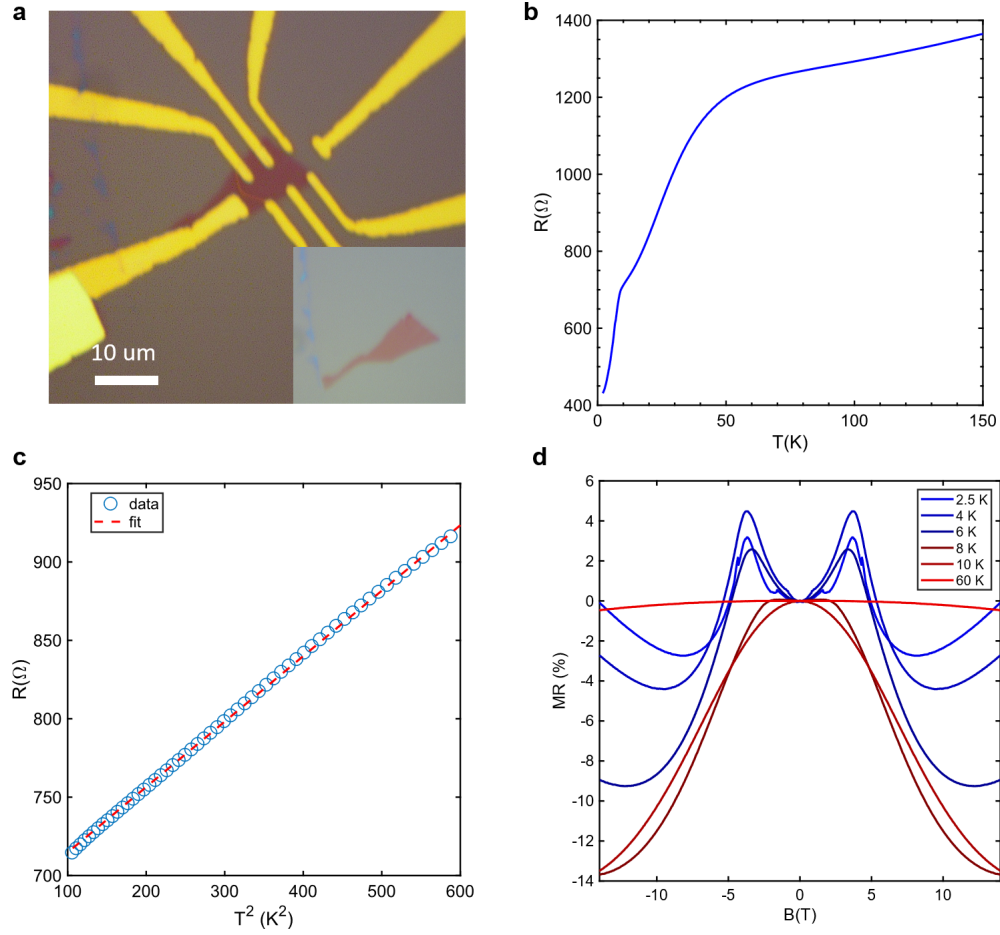


Figure 5.12: **a**, Optical micrograph 4 layers of CeSiI flake, inset shows the picture flake before fabrication . **b**, Longitudinal resistance, R_{xx} as temperatures, **c**, fermi liquid fit of R_{xx} depicts for 10 K to 25 K. **d**, Magnetoresistance of R_{xx} for range of temperatures 2.5 K to 60 K.

5.7 CONCLUSION

We have identified the first intrinsic vdW heavy fermion material, CeSiI, through bulk characterization including spectroscopy, transport, and magnetism. These measurements highlight the antiferromagnetic ordering from the RKKY interaction that directly competes with the formation of the Kondo

lattice shown to order at ~ 50 K in our electron transport. In addition, the moderately large Sommerfeld coefficient obtained from heat capacity, indicate the heavy fermion nature of CeSiI. This material can also be mechanically exfoliated down to atomically thin crystals. we demonstrate mesoscale device fabrication employing these thin flakes. Our initial electron transport measurements on thin flakes indicate that the antiferromagnetism and the Kondo lattice are maintained in the 2D. The discovery of a 2D vdW heavy fermion material opens the possibilities to obtaining a monolayer and exploring the complex phenomena in these heavy fermion systems in the 2D limits.

6

Outlook

Research in 2D materials has been extensively developed in the last two decades. Developing new methods bring possibilities to grow and manipulate conventional and new layered materials with unique properties. In this thesis, I discussed how to fabricate electronic devices and measure electrical and structural properties of engineered and new 2D material candidates.

In Chapter 2, I discussed electrochemical intercalation in finite discrete vdW hetero-structure layers. We used several techniques to characterize the intercalation process in the 2D limit and reveal

the process on the microscopic scale. The creation of vdW heterointerfaces between graphene and MoX_2 results in over 10-fold accumulation of charge in MoX_2 compared to $\text{MoX}_2/\text{MoX}_2$ homointerfaces, while enforcing a more negative intercalation potential than that of bulk MoX_2 by at least 0.5 V. This work clearly demonstrates the ability to engineer hetero-structures to host new ions. From this, we have tools to intercalate new ions into an engineered heterostructure host and create unique properties by manipulating non magnetic 2D materials with magnetic ions. Thus, inducing both superconductivity and magnetization could be an interesting avenue to explore as an extension of our work.

In Chapter 2, I described a technique to study ion diffusion dynamics. This methodology enables the evaluation of the energetics and dynamics of intercalation processes in atomically thin samples. The diffusion coefficient for AlCl_4^- , measured in 2D graphitic hosts approaches $10^{-5} \text{ cm}^2 \text{ s}^{-1}$ at 320 K, establishing the intrinsic upper limit. A useful extension of this work could be to study the diffusion of AlCl_4^- ions into composite layered materials (graphene/ MoS_2). Furthermore, we can use heavy ion intercalation to induce spin orbit coupling in few layer graphene.

In Chapter 4, I presented electrical transport measurements in two categories of novel layered materials. Metal Organic Frameworks (MOFs) are porous materials with extended tunability of lattice size and structure. We performed electrical transport measurements, specifically Hall effect measurements, of these MOFs. Our results on single crystal MOFs revealed metallic conductivity down to 0.3 K, which contrasts with apparent activated conductivity for polycrystalline films. Notably, single rods shaped MOFs exhibit conductivities up to 150 S/cm, which persist even after prolonged exposure to the ambient environment. In addition, we develop a growth method that generates single-crystal plates with lateral dimensions exceeding 10 μm , allowing the characterization of 2D basal-plane electrical properties of a representative 2D πMOF , Ni-CAT-1 ($\text{Ni}_3(\text{HHTP})_2$; HHTP, 2,3,6,7,10,11-hexahydroxytriphenylene). High quality crystals exhibit a measurable Hall effect and an electrical conductivity of up to 2 S/cm, two orders of magnitude higher than pressed-pellets. These single crystal

studies confirm that 2D MOFs hold promise as molecularly tunable platforms for fundamental science and applications where porosity and conductivity are critical. In the second part of this chapter, we introduce the newest graphene family member, graphullerene. Graphullerene is a few-layer superatomic cousin of graphene, made of C_{60} superatoms placed in an ion honeycomb lattice. This material is a semiconductor with high thermal conductivity and interesting optical properties. Future work on this material could involve investigating ionic liquid gating to tune the charge density and explore the possibility of superconductivity. Also, graphullerene has unique optical properties which we can combine with other 2D materials such as MoS_2 in order to study exciton formation in hybrid 2D heterostructures.

In Chapter 5, our report of a vdW metal with an intrinsic heavy fermion ground state provides a unique platform to probe its electron correlations at microscopic length scales and systematically explore its Doniach phase diagram. In fact, our results already hint at a magnetic field-induced quantum critical point, which in the future could be accessed using new tuning parameters enabled by the exfoliable nature of CeSiI, such as physical dimension, strain, symmetry breaking and heterostructuring. Combining these tuning parameters with synthetic modifications of the material could afford control over its Fermi energy, charting a path towards programmable effective electron mass. or the creation of a Kondo insulator state. Furthermore, suppression of magnetic order may lead to the emergence of superconductivity in correlated systems. In the future, one way to extend this study would be to lower the temperature with higher magnetic field of monolayer and bilayer CeSiI to explore the true 2D limit of a heavy fermion system. One could also perform a quantum capacitance measurement by creating a graphene/CeSiI hetero-structure to probe the thermodynamic properties at microscope scales.

A

Fabrication and characterization of Electrochemical Cell

Samples were fabricated in a way to that described in appendixA. In brief, mechanical exfoliation of Kish graphite (Covalent Materials Corp.) and molybdenum dichalcogenides, MoX_2 ($X = \text{S}, \text{Se}$) (HQ Graphene), onto p-doped silicon with 285 nm SiO_2 furnished crystals of the desired thickness, which were identified by optical contrast. Hexagonal boron nitride (h-BN) flakes of thickness 15–30 nm

were similarly exfoliated and used to pick up graphene and/or MoX₂ layers in the designated order. Finally, release of these stacks onto a second flake of h-BN resulted in h-BN-encapsulated heterostructures that were subjected to annealing in high vacuum for 30 min at 350 °C. For the devices fabricated on silicon nitride membranes, thinner h-BN flakes (≤ 5 nm) were used. Standard electron-beam lithography followed by evaporation of Cr/Pt (1 nm/9 nm) electrodes was used to define on-chip counter and pseudoreference electrodes. Reactive ion etching (RIE) using a mixture of CHF₃, Ar, and O₂ was subsequently used to shape the heterostructure into a Hall bar. Another round of lithography was used to delineate an etch mask that overlaps with the protruding legs of the Hall bar. Immediately following another RIE step, the same etch mask was used as the metal deposition mask with Cr/Pd/Au (5 nm/ 15 nm/70 nm) contacts. This resulted in a one-dimensional edge-contact to the active layers and low contact resistances.

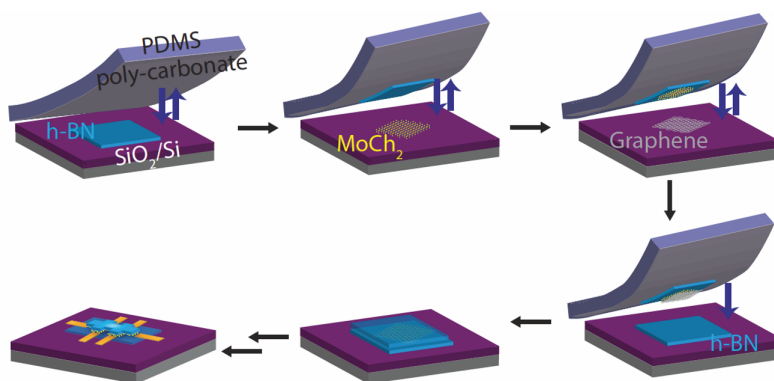


Figure A.1: Schematic illustration of stacking hBN/Gr/MoS₂/hBN to fabricate electrochemical cell. Dry transfer method has been used to make stack.

In an argon-filled glove box, 3.7 ml of anhydrous acetonitrile (dried with 3 Å molecular sieves; Sigma-Aldrich) was added to 0.3 g of polyethylene oxide (PEO; Sigma-Aldrich) and 50 mg of lithium bis(trifluoromethanesulfonyl)imide (LiTFSI). After stirring overnight, a 10–15 μl droplet of this electrolyte solution was cast onto the Si chip possessing the electrically contacted heterostructure stack,

such that the droplet encompassed both the stack and the counter/reference electrodes. Rapid evaporation of the acetonitrile solvent yielded a solid polymer electrolyte for electrochemical studies. Additional extraneous solvent was removed by vacuum-drying the electrolyte overnight. Immediately before measurements the measurement device was isolated from ambient moisture and oxygen using a glass coverslip affixed to the chip carrier with vacuum grease. The device was then removed from the glove box and transferred promptly to the cryostat and vacuum-sealed.

B

Diffusion study Micro-electrochemical cell fabrication

Graphite (Graphene supermarket) and hBN were mechanically exfoliated onto SiO₂/Si substrates and flakes of desired thicknesses were identified by optical contrast to obtain 10–30 crystals of nm hBN and four-layer graphene. hBN/graphene/hBN heterostructures were fabricated via a dry-transfer method, wherein a flake of hBN was used to pick up graphene, and subsequently released on top of another

hBN flake. The stack was annealed at 350 °C in high vacuum to remove surface residue and ensure good contact between flakes. electron-beam lithography followed by reactive ion etching was used to form a Hall bar shape in the heterostructure. Contacts to the Hall bar were deposited by thermal evaporation of Ti/AL (5/80 nm) or Ti (80 nm). Ti/Al (5 nm/100 nm) counter and reference electrodes were also deposited. An ionic liquid electrolyte was prepared in an argon glove box with O₂ and H₂O < 0.1 ppm by mixing 0.6 g of anhydrous AlCl₃ (99.99%, Sigma-Aldrich) with 0.4 g 1-ethyl-3-methylimidazolium chloride (98% Sigma-Aldrich). An exothermic reaction between these solids produced a pale-yellow liquid at room temperature. After stirring overnight, a 10–20 μL droplet of this electrolyte was dropcast on top of the device, ensuring that the counter electrode (CE), reference electrode (RE), and Hall bar workign electrode (WE) were covered by the droplet

Electronic transport measurements were performed in a Quantum Design Physical Property Measurement System (PPMS). To intercalate ions into the heterostructure, a potential was applied between the Pt CE and heterostructure WE at a rate of 2 mV/s (Keithley 2400) at 300 K. A voltmeter (Agilent 34401A Digital Multimeter) with a high internal impedance of >10 GΩ was used to measure the potential at the RE. Simultaneously, the resistance of the device was measured by applying an AC current (I_{sd}) of 100–500 nA using a lock-in amplifier (Stanford Research SR830). Longitudinal (V_{xx}) and transverse (V_{xy}) voltages were measured throughout using a lock-in amplifier, and longitudinal (R_{xx}) and transverse (R_{xy}) resistances were determined from the relationship $R = V/I_{sd}$. The Hall carrier density, n_H , was then calculated by $n_H = (I_{sd} B)/(V_{xy} e)$, where B is the applied magnetic field and e is the elementary charge. At the final applied potential (typically 2.5 V), the system was rapidly cooled to 200 K (10 K min⁻¹) to conduct additional transport measurements.



CeSiI Device Fabrication Complexity

Here, we discuss the sensitivity of CeSiI crystal in device fabrication. CeSiI is a highly sensitive material. Air and water could degrade even bulk crystal in less than a minute exposure into air. The exfoliation performs inside Argon glovebox with O_2 and $H_2O < 0.1$ ppm . We need to follow few steps to fabricate a reliable few layer device. First, we have to be sure the substrate that we will use for exfoliation should bake at least for more than 24 hr on hot plate 300 C. Presence of small amount of water on substrate surface speed up the flake degradation even in inert environment. The scotch tape

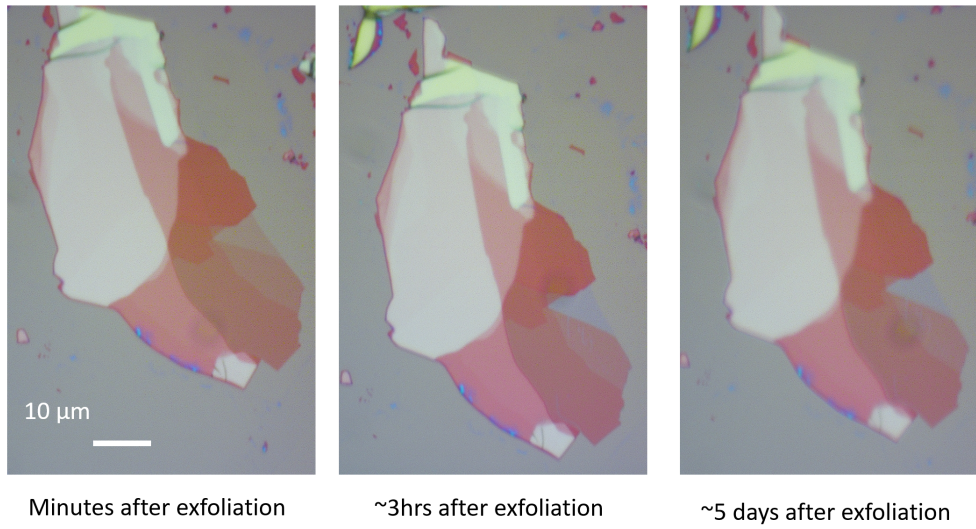


Figure C.1: the left picture shows the final fabricated device. the right picture depicts the electrolyte placed on top of the stack.

is used to exfoliate and thin down the bulk crystal. the exfoliated flakes are deposited on the Si/SiO₂ substrates. Fig C. 1 shows the degradation of monolayer exfoliated on Si/SiO₂. The flake color changes from light red to light blue. Interestingly, the degradation stops at bottom layer and the top layers are protected from degradation. few layers flake are usually very stable inside glovebox for even more than a week. the fabrication is done as the way mentioned in the main text via high resolution stencil mask technique. The final device needs to cover with hBN before loading inot cryostat. Cold PDMS dry transfer technique is used to pick up desired hBN. we pickup hBN at -105^0 C with PDMS. The hBN is placed at fabricated device and release slowly at 0 C. hBN solely can not make enough protection to save the device. we use thin cover glass slip to protect mounted device in a chip carrier. Grease is used to sealed the glass slide. we minimize the loading process to cryostat. after loading into the cryostat, we pump out the chamber area to high vacuum as fast as possible. Even with fast loading process and all protections, some device dies after few minutes loaded inside the cryostat. Figures C2, C3 present few devices with and without hBN before loading and after unloading from cryostat.

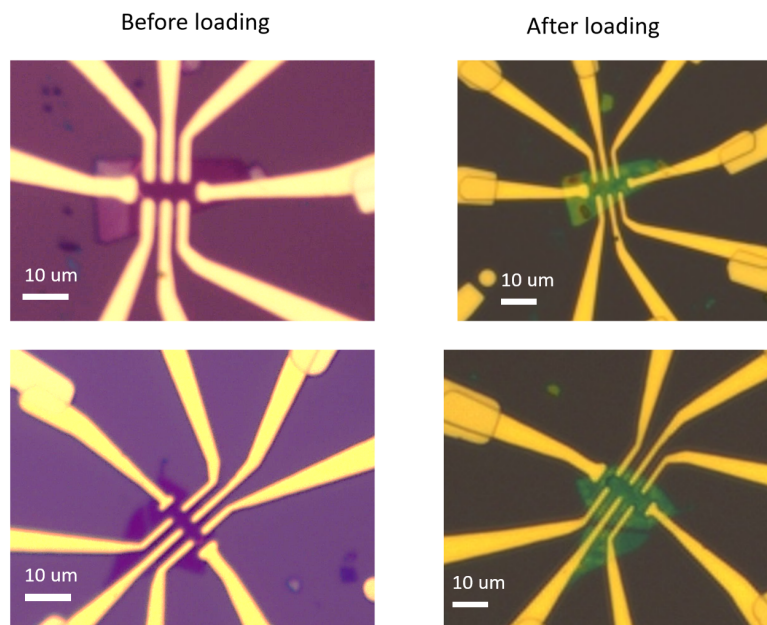


Figure C.2: The left picture shows the final fabricated device before loading. the right picture shows the device after unloading while it has still covered with glass slide.the degradation changes the flakes color. It turns them to green from purple.

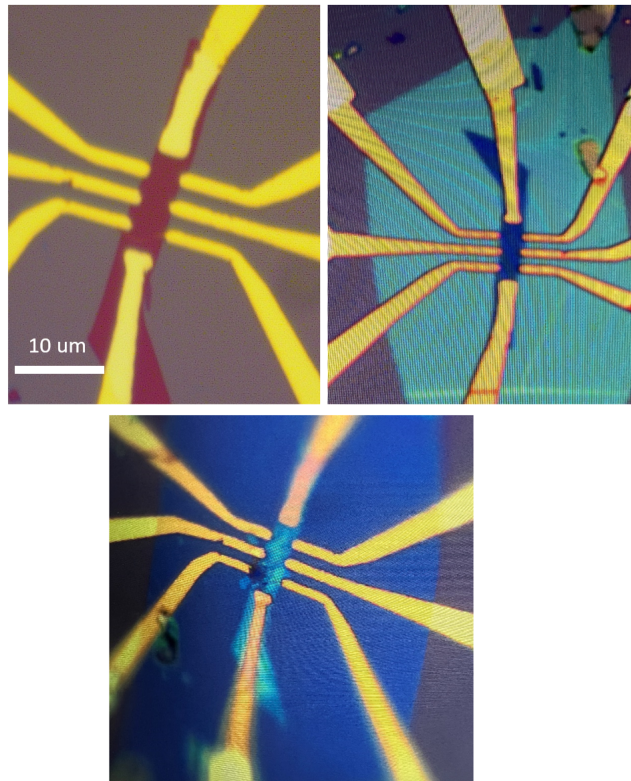


Figure C.3: The top left picture shows the final fabricated device before loading. the top right micrograph depicts the device after covered with 40 nm hBN. the bottom picture shows the device after unloading while it has still covered with glass slide. we can see clearly the device degraded.

Bibliography

- [1] K. S. Novoselov, A. K. Geim, S. V. Morozov, D.-e. Jiang, Y. Zhang, S. V. Dubonos, I. V. Grigorieva, and A. A. Firsov, *science* **306**, 666 (2004).
- [2] R. Peierls, in *Annales de l'institut Henri Poincaré*, Vol. 5 (1935) pp. 177–222.
- [3] L. D. Landau, *Phys. Z. Sowjetunion* **11**, 26 (1937).
- [4] A. K. Geim and I. V. Grigorieva, *Nature* **499**, 419 (2013).
- [5] G. Dresselhaus, J. T. Nicholls, and M. S. Dresselhaus, in *Graphite Intercalation Compounds II* (Springer, 1992) pp. 247–345.
- [6] N. Emery, C. Hérold, J.-F. Maréché, and P. Lagrange, *Science and technology of advanced materials* (2009).
- [7] Y. Guo, R. B. Smith, Z. Yu, D. K. Efetov, J. Wang, P. Kim, M. Z. Bazant, and L. E. Brus, *The journal of physical chemistry letters* **7**, 2151 (2016).
- [8] L. Sun, M. G. Campbell, and M. Dincă, *Angewandte Chemie International Edition* **55**, 3566 (2016).
- [9] D. Sheberla, J. C. Bachman, J. S. Elias, C.-J. Sun, Y. Shao-Horn, and M. Dincă, *Nature materials* **16**, 220 (2017).
- [10] E. M. Miner, T. Fukushima, D. Sheberla, L. Sun, Y. Surendranath, and M. Dincă, *Nature communications* **7**, 1 (2016).
- [11] A. J. Clough, J. W. Yoo, M. H. Mecklenburg, and S. C. Marinescu, *Journal of the American Chemical Society* **137**, 1118 (2015).
- [12] M. G. Campbell, S. F. Liu, T. M. Swager, and M. Dinca, *Journal of the American Chemical Society* **137**, 13780 (2015).
- [13] D. Sheberla, L. Sun, M. A. Blood-Forsythe, S. Er, C. R. Wade, C. K. Brozek, A. Aspuru-Guzik, and M. Dincă, *Journal of the American Chemical Society* **136**, 8859 (2014).

- [14] J.-H. Dou, L. Sun, Y. Ge, W. Li, C. H. Hendon, J. Li, S. Gul, J. Yano, E. A. Stach, and M. Dincă, *Journal of the American Chemical Society* **139**, 13608 (2017).
- [15] A. Hirsch, *Nature materials* **9**, 868 (2010).
- [16] P. Coleman, arXiv preprint cond-mat/0612006 (2006).
- [17] A. C. Hewson, *The Kondo problem to heavy fermions*, 2 (Cambridge university press, 1997).
- [18] J. Kondo, *Progress of theoretical physics* **32**, 37 (1964).
- [19] S. Wirth and F. Steglich, *Nature Reviews Materials* **1**, 1 (2016).
- [20] G. Stewart, Z. Fisk, and M. Wire, *Physical Review B* **30**, 482 (1984).
- [21] M. Armand and J.-M. Tarascon, *nature* **451**, 652 (2008).
- [22] J. B. Goodenough and K.-S. Park, *Journal of the American Chemical Society* **135**, 1167 (2013).
- [23] P. Simon, Y. Gogotsi, and B. Dunn, *Science* **343**, 1210 (2014).
- [24] J. Maier, *Angewandte Chemie International Edition* **52**, 4998 (2013).
- [25] E. Pomerantseva and Y. Gogotsi, *Nature Energy* **2**, 1 (2017).
- [26] M. Chhowalla, H. S. Shin, G. Eda, L.-J. Li, K. P. Loh, and H. Zhang, *Nature chemistry* **5**, 263 (2013).
- [27] S. F. Zhao, G. A. Elbaz, D. K. Bediako, C. Yu, D. K. Efetov, Y. Guo, J. Ravichandran, K.-A. Min, S. Hong, T. Taniguchi, *et al.*, *Nano letters* **18**, 460 (2018).
- [28] M. Kühne, F. Paolucci, J. Popovic, P. M. Ostrovsky, J. Maier, and J. H. Smet, *Nature nanotechnology* **12**, 895 (2017).
- [29] L. Wang, I. Meric, P. Huang, Q. Gao, Y. Gao, H. Tran, T. Taniguchi, K. Watanabe, L. Campos, D. Muller, *et al.*, *Science* **342**, 614 (2013).
- [30] A. Das, S. Pisana, B. Chakraborty, S. Piscanec, S. K. Saha, U. V. Waghmare, K. S. Novoselov, H. R. Krishnamurthy, A. K. Geim, A. C. Ferrari, *et al.*, *Nature nanotechnology* **3**, 210 (2008).
- [31] D. K. Efetov and P. Kim, *Physical review letters* **105**, 256805 (2010).
- [32] D. Shoenberg, *Magnetic oscillations in metals* (Cambridge university press, 2009).
- [33] H. Cao, J. Tian, I. Miotkowski, T. Shen, J. Hu, S. Qiao, and Y. P. Chen, *Physical Review Letters* **108**, 216803 (2012).

- [34] F. Xiong, H. Wang, X. Liu, J. Sun, M. Brongersma, E. Pop, and Y. Cui, *Nano letters* **15**, 6777 (2015).
- [35] C. Zhu, X. Mu, P. A. van Aken, Y. Yu, and J. Maier, *Angewandte chemie* **126**, 2184 (2014).
- [36] K. F. Mak, K. He, C. Lee, G. H. Lee, J. Hone, T. F. Heinz, and J. Shan, *Nature materials* **12**, 207 (2013).
- [37] L. Malard, M. A. Pimenta, G. Dresselhaus, and M. Dresselhaus, *Physics reports* **473**, 51 (2009).
- [38] V. Petkov, S. Billinge, P. Larson, S. Mahanti, T. Vogt, K. Rangan, and M. G. Kanatzidis, *Physical Review B* **65**, 092105 (2002).
- [39] G. Eda, T. Fujita, H. Yamaguchi, D. Voiry, M. Chen, and M. Chhowalla, *ACS nano* **6**, 7311 (2012).
- [40] F. Ma, G. Gao, Y. Jiao, Y. Gu, A. Bilic, H. Zhang, Z. Chen, and A. Du, *Nanoscale* **8**, 4969 (2016).
- [41] G. Eda, H. Yamaguchi, D. Voiry, T. Fujita, M. Chen, and M. Chhowalla, *Nano letters* **11**, 5111 (2011).
- [42] X. Yin, Q. Wang, L. Cao, C. S. Tang, X. Luo, Y. Zheng, L. M. Wong, S. J. Wang, S. Y. Quek, W. Zhang, *et al.*, *Nature communications* **8**, 1 (2017).
- [43] X. Fan, P. Xu, D. Zhou, Y. Sun, Y. C. Li, M. A. T. Nguyen, M. Terrones, and T. E. Mallouk, *Nano letters* **15**, 5956 (2015).
- [44] A. Singh and U. V. Waghmare, in *2D Inorganic Materials beyond Graphene* (World Scientific, 2018) pp. 389–442.
- [45] Y. Wang, J. Z. Ou, A. F. Chrimes, B. J. Carey, T. Daeneke, M. M. Alsaif, M. Mortazavi, S. Zhuiykov, N. Medhekar, M. Bhaskaran, *et al.*, *Nano letters* **15**, 883 (2015).
- [46] S. N. Shirodkar and E. Kaxiras, *Physical Review B* **93**, 245438 (2016).
- [47] D. K. Bediako, M. Rezaee, H. Yoo, D. T. Larson, S. Zhao, T. Taniguchi, K. Watanabe, T. L. Brewer-Thomas, E. Kaxiras, and P. Kim, *Nature* **558**, 425 (2018).
- [48] J. Sun, H.-W. Lee, M. Pasta, H. Yuan, G. Zheng, Y. Sun, Y. Li, and Y. Cui, *Nature nanotechnology* **10**, 980 (2015).
- [49] L. Oakes, R. Carter, T. Hanken, A. P. Cohn, K. Share, B. Schmidt, and C. L. Pint, *Nature communications* **7**, 1 (2016).
- [50] J. Abraham, K. S. Vasu, C. D. Williams, K. Gopinadhan, Y. Su, C. T. Cherian, J. Dix, E. Prestat, S. J. Haigh, I. V. Grigorieva, *et al.*, *Nature nanotechnology* **12**, 546 (2017).

- [51] M. Elimelech and W. A. Phillip, *science* **333**, 712 (2011).
- [52] S. N. Shirodkar, M. Mattheakis, P. Cazeaux, P. Narang, M. Soljagic, and E. Kaxiras, Preprint at <https://arxiv.org/pdf/1703.01558v1> (2017).
- [53] X. Qian, J. Liu, L. Fu, and J. Li, *Science* **346**, 1344 (2014).
- [54] D.-Y. Wang, C.-Y. Wei, M.-C. Lin, C.-J. Pan, H.-L. Chou, H.-A. Chen, M. Gong, Y. Wu, C. Yuan, M. Angell, *et al.*, *Nature communications* **8**, 1 (2017).
- [55] A. VahidMohammadi, A. Hadjikhani, S. Shahbazmohamadi, and M. Beidaghi, *ACS nano* **11**, 11135 (2017).
- [56] Y. Li, Y. Lu, P. Adelhelm, M.-M. Titirici, and Y.-S. Hu, *Chemical Society Reviews* **48**, 4655 (2019).
- [57] F. Ambroz, T. J. Macdonald, and T. Nann, *Advanced Energy Materials* **7**, 1602093 (2017).
- [58] S. K. Das, S. Mahapatra, and H. Lahan, *Journal of Materials Chemistry A* **5**, 6347 (2017).
- [59] H. Vikström, S. Davidsson, and M. Höök, *Applied Energy* **110**, 252 (2013).
- [60] R. F. Service, Al bids to vie with li in battery wars (2012).
- [61] M.-C. Lin, M. Gong, B. Lu, Y. Wu, D.-Y. Wang, M. Guan, M. Angell, C. Chen, J. Yang, B.-J. Hwang, *et al.*, *Nature* **520**, 324 (2015).
- [62] Y. Hu, D. Ye, B. Luo, H. Hu, X. Zhu, S. Wang, L. Li, S. Peng, and L. Wang, *Advanced Materials* **30**, 1703824 (2018).
- [63] K. V. Kravchyk, S. Wang, L. Piveteau, and M. V. Kovalenko, *Chemistry of Materials* **29**, 4484 (2017).
- [64] L. Zhang, L. Chen, H. Luo, X. Zhou, and Z. Liu, *Advanced Energy Materials* **7**, 1700034 (2017).
- [65] H. Chen, H. Xu, S. Wang, T. Huang, J. Xi, S. Cai, F. Guo, Z. Xu, W. Gao, and C. Gao, *Science advances* **3**, ea07233 (2017).
- [66] C.-J. Pan, C. Yuan, G. Zhu, Q. Zhang, C.-J. Huang, M.-C. Lin, M. Angell, B.-J. Hwang, P. Kaghazchi, and H. Dai, *Proceedings of the National Academy of Sciences* **115**, 5670 (2018).
- [67] G. A. Elia, G. Greco, P. H. Kamm, F. García-Moreno, S. Raoux, and R. Hahn, *Advanced Functional Materials* **30**, 2003913 (2020).
- [68] G. Greco, D. Tatchev, A. Hoell, M. Krumrey, S. Raoux, R. Hahn, and G. A. Elia, *Journal of Materials Chemistry A* **6**, 22673 (2018).

- [69] J. P. Sethna, *Statistical mechanics: entropy, order parameters, and complexity*, Vol. 14 (Oxford University Press, USA, 2021).
- [70] W. Bao, J. Wan, X. Han, X. Cai, H. Zhu, D. Kim, D. Ma, Y. Xu, J. N. Munday, H. D. Drew, *et al.*, *Nature communications* **5**, 1 (2014).
- [71] A. M. Friedman and J. W. Kennedy, *Journal of the American Chemical Society* **77**, 4499 (1955).
- [72] D.-G. Ha, M. Rezaee, Y. Han, S. A. Siddiqui, R. W. Day, L. S. Xie, B. J. Modtland, D. A. Muller, J. Kong, P. Kim, *et al.*, *ACS central science* **7**, 104 (2020).
- [73] R. W. Day, D. K. Bediako, M. Rezaee, L. R. Parent, G. Skorupskii, M. Q. Arguilla, C. H. Hendon, I. Stassen, N. C. Gianneschi, P. Kim, *et al.*, *ACS central science* **5**, 1959 (2019).
- [74] H. Furukawa, K. E. Cordova, M. O’Keeffe, and O. M. Yaghi, *Science* **341**, 1230444 (2013).
- [75] F.-X. Coudert, *Chemistry of Materials* **27**, 1905 (2015).
- [76] X. Huang, S. Zhang, L. Liu, L. Yu, G. Chen, W. Xu, and D. Zhu, *Angewandte Chemie International Edition* **57**, 146 (2018).
- [77] W. Li, Z. Wang, F. Deschler, S. Gao, R. H. Friend, and A. K. Cheetham, *Nature Reviews Materials* **2**, 1 (2017).
- [78] L. Dong, Y. Kim, D. Er, A. M. Rappe, and V. B. Shenoy, *Physical review letters* **116**, 096601 (2016).
- [79] M. Hmadeh, Z. Lu, Z. Liu, F. Gándara, H. Furukawa, S. Wan, V. Augustyn, R. Chang, L. Liao, F. Zhou, *et al.*, *Chemistry of Materials* **24**, 3511 (2012).
- [80] T. Kambe, R. Sakamoto, T. Kusamoto, T. Pal, N. Fukui, K. Hoshiko, T. Shimojima, Z. Wang, T. Hirahara, K. Ishizaka, *et al.*, *Journal of the American Chemical Society* **136**, 14357 (2014).
- [81] M. L. Aubrey, B. M. Wiers, S. C. Andrews, T. Sakurai, S. E. Reyes-Lillo, S. M. Hamed, C.-J. Yu, L. E. Darago, J. A. Mason, J.-O. Baeg, *et al.*, *Nature materials* **17**, 625 (2018).
- [82] L. S. Xie, L. Sun, R. Wan, S. S. Park, J. A. DeGayner, C. H. Hendon, and M. Dincă, *Journal of the American Chemical Society* **140**, 7411 (2018).
- [83] M. E. Foster, K. Sohlberg, M. D. Allendorf, and A. A. Talin, *The journal of physical chemistry letters* **9**, 481 (2018).
- [84] T.-H. Le, Y. Kim, and H. Yoon, *Polymers* **9**, 150 (2017).
- [85] H. Liu, A. Pourret, and P. Guyot-Sionnest, *Acs Nano* **4**, 5211 (2010).

- [86] M. Ahlskog, M. Reghu, and A. Heeger, *Journal of Physics: Condensed Matter* **9**, 4145 (1997).
- [87] A. B. Kaiser, *Reports on Progress in Physics* **64**, 1 (2001).
- [88] D. Feng, T. Lei, M. R. Lukatskaya, J. Park, Z. Huang, M. Lee, L. Shaw, S. Chen, A. A. Yakovenko, A. Kulkarni, *et al.*, *Nature Energy* **3**, 30 (2018).
- [89] M. K. Smith, K. E. Jensen, P. A. Pivak, and K. A. Mirica, *Chemistry of Materials* **28**, 5264 (2016).
- [90] H. W. Kroto, J. R. Heath, S. C. O'Brien, R. F. Curl, and R. E. Smalley, *nature* **318**, 162 (1985).
- [91] W. I. David, R. M. Ibberson, J. C. Matthewman, K. Prassides, T. J. S. Dennis, J. P. Hare, H. W. Kroto, R. Taylor, and D. R. Walton, *Nature* **353**, 147 (1991).
- [92] M. Tanaka and S. Yamanaka, *Crystal Growth & Design* **18**, 3877 (2018).
- [93] L. Hou, X. Cui, B. Guan, S. Wang, R. Li, Y. Liu, D. Zhu, and J. Zheng, *Nature* **606**, 507 (2022).
- [94] H. Shishido, T. Shibauchi, K. Yasu, T. Kato, H. Kontani, T. Terashima, and Y. Matsuda, *Science* **327**, 980 (2010).
- [95] M. Neumann, J. Nyéki, B. Cowan, and J. Saunders, *Science* **317**, 1356 (2007).
- [96] V. Vaňo, M. Amini, S. C. Ganguli, G. Chen, J. L. Lado, S. Kezilebieke, and P. Liljeroth, *Nature* **599**, 582 (2021).
- [97] R. Okuma, C. Ritter, G. J. Nilsen, and Y. Okada, *Physical Review Materials* **5**, L121401 (2021).
- [98] M. R. Victoria A. Posey, *arxiv* (2023)



THIS THESIS WAS TYPESET using \LaTeX , originally developed by Leslie Lamport and based on Donald Knuth's \TeX . The body text is set in 11 point Egenolff-Berner Garamond, a revival of Claude Garamont's humanist typeface. The above illustration, "Science Experiment 02", was created by Ben Schlitter and released under [CC BY-NC-ND 3.0](#). A template that can be used to format a PhD thesis with this look and feel has been released under the permissive MIT (X11) license, and can be found online at github.com/suchow/Dissertate or from its author, Jordan Suchow, at suchow@post.harvard.edu.